Propeller Analysis with Adjoint Method using SU2

Daamanjyot Barara

Delft University of Technology

TU Delft

Cover Photo Credits -
https://pixabay.com/nl/photos/vlak-a400m-airbus-leger-air-force-5020700/

Propeller Analysis with Adjoint Method using SU2

by

Daamanjyot Barara

in partial fulfillment of the requirements for the degree of

Master of Science
in Aerospace Engineering

at the Delft University of Technology,
to be defended publicly on Friday January 28, 2022 at 09:30 AM.

Student number:	4902114	
Supervisor:	Dr. ir. T. Sinnige,	TU Delft, Supervisor
	Dr. ir. M. Pini,	TU Delft, Supervisor
Thesis committee:	Dr. ir. T. Sinnige,	TU Delft, Supervisor
	Dr. ir. M. Pini,	TU Delft, Supervisor
	Prof. dr. ing. G. Eitelberg,	TU Delft, Chairman
	Dr. ir. A. H. van Zuijlen,	TU Delft

An electronic version of this thesis is available at `http://repository.tudelft.nl/`.

TU Delft

Preface

Working on this thesis has been a fruitful experience for me as I started the work with limited experience with the computational tools implemented during the research. This would not have been possible without the constant support of my supervisors, Tomas Sinnige and Matteo Pini. Their immense knowledge and enthusiasm about the field motivated me to dig deeper while assessing the results. I am grateful to both my supervisors for being responsive and easily reachable to clear my doubts or whenever I felt uncertain about my results. Insightful discussions during the routine progress meeting and over the mail helped me steer my work in the right direction. I extend sincere gratitude to Tomas and Matteo for their excellent support and guidance throughout this thesis.

I would like to thank all my friends, who made my time and experience in Delft so much better. I am very grateful to my parents for their love and relentless support. My sister, Saihej, for her continuous encouragement throughout this whole time.

Daamanjyot Barara
Delft, January 2022

Abstract

To cater to the increasing demand in short-range passenger air transport and the research in electric and hybrid aircraft, there is a renewed interest in the research of propellers. Propellers are known to have high aerodynamic efficiency, which translates to lower fuel burn in comparison to other jet engines, making it an attractive option for airlines to operate it in regional transport. With such a heightened interest in the research of propellers for future applications, it is crucial to study the effect of the shape-design of the blades on its aerodynamic performance parameters. Since complex flow fields are produced by the complex geometry of modern propellers, advanced analysis tools are needed to accurately derive the propeller designs in the design process. Therefore, aerodynamic design sensitivity analysis based on the implementation of advanced Computational fluid dynamics tools can provide design insights to obtain efficient propeller designs. The goal of this dissertation is to perform the aerodynamic analysis of a propeller using multiphysics simulation software - SU2 and ANSYS Fluent and then perform a design sensitivity study using SU2's adjoint capabilities.

The verification and validation of SU2's flow solver is performed using the two propeller test cases- straight and swept blade. A RANS method with S-A turbulence model is used to perform the aerodynamic analysis of the propellers. For the same computational grid, a higher discretization error was estimated for SU2 as compared to ANSYS Fluent. SU2's flow simulation results are used to draw a comparison between the straight and swept blade based on the aerodynamic performance. The redistribution of the blade loading due to the introduction of sweep led to differences in the aerodynamic performance of the blades. It was found that for a constant freestream velocity, the swept blade operated with higher aerodynamic efficiency at high advance ratios with the largest gain of 0.47% at J=1.2. While it experiences a marginal loss in the efficiency at lower advance ratios with the largest decrement being 0.37% at J=0.6.

SU2's adjoint solver is used to perform discrete adjoint-based sensitivity analysis of the propellers at multiple design points. The Free-Form Deformation method is implemented to parameterize the propeller blades and study the sensitivity of the propeller's performance parameters to the deformation of the surface. This study has been performed for two objective functions- thrust coefficient and torque coefficient. The surface sensitivities of the thrust coefficient, obtained from the adjoint analysis indicated that the regions of high sensitivity are located at the leading-edge and outboard portion of the blade's suction side. The concentration of the regions of high sensitivity changed with the advance ratios. The surface sensitivities of the torque coefficient result in regions of high sensitivities similar to the ones seen in the case of thrust coefficient. Both blades show similar surface sensitivity contours of the two objective functions.

Based on the gradient information, the highest gradients of thrust coefficient is attained for the design variables located near the trailing edge of the straight blade, at a given radial position. Swept blade shows a trend of chordwise gradient similar to the straight blade at all radial positions, except the tip region. The introduction of a sweep at the tip results in the shift of the dominant design variable from trailing edge to mid-chord. The gradients of the torque coefficient resulted in a chordwise trend similar to that of the thrust coefficient for both blades, attributing to the dominant lift contribution to thrust and torque at the computed advance ratios.

The resulting understanding of the sensitivity of the propeller's performance parameters to the variation in blade shape design from this study can be used as an input for future design studies aimed at designing efficient propellers. Likewise, the RANS-based CFD methodology incorporating the adjoint method used in this work can be aimed at developing adjoint-based multidisciplinary design capabilities for propellers.

Contents

Nomenclature

Abbreviations

2D	=	Two-dimensional
3D	=	Three-dimensional
AD	=	Algorithmic/Automatic Differentiation
ADT	=	Actuator Disk Theory
BEMT	=	Blade Element Momentum Theory
CAD	=	Computer Aided Design
CFD	=	Computational Fluid Dynamics
DES	=	Detached Eddy Simulation
DNS	=	Direct Numerical Simulation
FD	=	Finite Differences
FFD	=	Free-Form Deformation
LES	=	Large Eddy Simulation
MCA	=	Mid-Chord Alignment
NS	=	Navier-Stokes
NURBS	=	Non-Uniform Rational B-Spline
PDE	=	Partial Differential Equations
RANS	=	Reynolds Averaged Navier-Stokes
RBF	=	Radial Basis Functions
S-A	=	Spalart Allmaras
SST	=	Shear Stress Transport

Symbols

a	=	Speed of sound, m/s
B^i	=	Bernstein polynomial of order i
b	=	Local blade chord, m
C_D	=	Drag coefficient
C_f	=	Skin-friction coefficient
C_L	=	Lift coefficient
C_P	=	$P/(\rho_\infty n^3 D^5)$, Power coefficient
C_p	=	Pressure coefficient
C_T	=	$T/(\rho_\infty n^2 D^4)$ Thrust coefficient
D	=	Diameter of the Propeller, m
e	=	Total energy
J	=	$V_\infty/(nD)$, Advance ratio of the Propeller; Objective function
k_{ij}	=	Stiffness matrix
l_{chord}	=	Chord length of blade section, m
M	=	Mach Number
M_t	=	Tip Mach number
M_w	=	Molecular weight, kg/kmol
$\hat{n}$	=	Unit normal vector
n	=	Revolutions per minute of Propeller, s^{-1}
P	=	Shaft Power, W;
Pr_d	=	Dynamic Prandtl number
Pr_t	=	Turbulent Prandtl number

p	=	Static pressure, Pa; Observed order of accuracy
p^*	=	Theoretical order of accuracy
p_t	=	Total pressure, Pa
Q	=	Torque,Nm
Q_C	=	$Q/(\rho_\infty V_\infty^2 D^3)$, Torque coefficient based on q_∞
q_∞	=	$\rho V^2/2$, Freestream dynamic pressure, Pa
R	=	Residual Vector; Universal gas constant, J/kg s
Re	=	Reynolds number
r	=	Radial position on the blade, m
S	=	Sutherland's temperature, K
T	=	Thrust, N; Static temperature, K
T_C	=	$T/(q_\infty D^2)$, Thrust coefficient based on q_∞
T_t	=	Total temperature, K
t	=	Time, s
U	=	State Variables Vector / Flow Variables Vector
$\bar{U}$	=	Adjoint State Variables Vector
$U_s(\%)$	=	Standard deviation of fit
U_ϕ	=	Estimated discretization error
u	=	Velocity, m/s
u_*	=	Friction velocity, m/s
$\overrightarrow{u}$	=	Surface displacement
V_∞	=	Freestream velocity, m/s
V_{rel}	=	$\sqrt{(V_\infty)^2 + (\omega r)^2}$, Relative velocity at blade section, m/s
X	=	Volumetric grid
X_{surf}	=	Surface grid coordinates
y^+	=	Dimensionless wall distance
$y_{firstlayer}$	=	First layer thickness, m
α	=	Design Variable, deg; Angle of attack, deg
β	=	Blade pitch angle, deg
δ_{ij}	=	Kronecker delta function
δ_{RE}	=	Error estimator
ϵ	=	Energy transfer rate
η_K	=	Kolmogorov length scale
η_P	=	Efficiency of Propeller
λ	=	Adjoint variable vector
μ	=	Dynamic viscosity of the fluid, kg/m.s
ν	=	Kinematic viscosity of the fluid
ρ	=	Density, kg/m^3
ρ_0	=	Freestream density, kg/m^3
τ_w	=	Wall shear stress, Pa
τ_{ij}	=	Deviatoric stress tensor
ϕ	=	Flow quantity
ω	=	Rotational velocity, rad/s

List of Figures

List of Tables

1

Introduction

This chapter provides a brief introduction to the propeller research to highlight the motivation behind this study. Based on the motivation, the research objective and research questions are presented. Section 1.1 presents a brief discussion on the advancements in the field of propeller research in the past and renewed motivation. Section 1.2 discusses the numerical techniques used in the design studies of aerodynamic applications. Section 1.3 presents the propeller performance methodologies that are used in the propeller's design and performance analysis. The research objective and sub-objectives to meet them are presented in Section 1.4. Section 1.5 concludes the chapter by presenting the outline of this report.

1.1. Propeller Research: Past, Present and Future

1.1.1. The Past

Propellers have been instrumental in vaulting humans into a new era of transportation by launching the aviation era, since the day first mechanically controlled, sustained, and powered heavier-than-air flight of Wright Flyer took place on 17th Dec 1903. Propellers used in the Wright Flyer's propulsion system was deemed as one of the most innovative ideas conceived by the Wright brothers. They treated the propellers as a rotating wing that moved in a spiral course as it spun through the air. The idea was based on the same reasoning responsible for the generation of upward force (lift) on a curved surface placed in a stream of air and concluded that a horizontal force (thrust) would be generated when such a surface is placed vertically and rotated through the airflow. This theory of propeller led to extensive research during the pioneer era of aviation in order to explore the high-efficiency capabilities of the propellers. Since then propellers have come of age, as these have often been sought as a solution to overcome the challenges faced by the aviation industry in the past as well as in present.

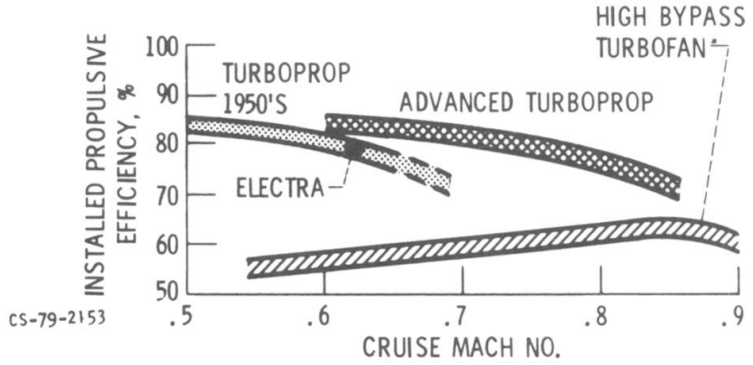

Figure 1.1: Comparison of installed propulsive efficiency of turboprops and turbofans at cruise Mach no.[10]

The propeller research experienced a lull period from the mid-1950s to the mid-1970s, due to the success of modern jet engines, i.e., turbojet and turbofan, which provided high-speed capabilities allowing cruise flights up to Mach 0.8. But, a dramatic rise in fuel prices in the 1970s prompted NASA and

several industry partners to research the propeller technology, to obtain a fuel-efficient alternative to the jet engines. The result of this research was the development of fuel-efficient, quieter propeller with lower internal and external noise environment that could be operated at high cruise Mach speeds and were called prop-fans. Prop-fans are advanced propeller designs with highly swept thin blades to reduce the noise radiation as well as losses due to compressibility effects experienced at high cruise speeds. Prop-fans achieved higher propulsive efficiency than turbojets and turbofans for the given range of high-speed during cruise flight, i.e., M=0.7 to M=0.8, as shown in Fig.1.1 [10, 35]. The high-propulsive efficiency capabilities of the propellers can be attributed to its ability to induce smaller velocity increments to a large mass of airflow and thus providing large savings in fuel consumption. Although, extensive research was done on single- and counter-rotating prop-fans from aerodynamics, aeroacoustics, and structural point of view but low and stable fuel prices at end of the 1980s halted various propeller research programs.

1.1.2. The Present and Future

Turboprop engines allow up to 10-30% of fuel savings as compared to a turbofan engine operating at a similar speed [57]. Moreover, due to its ability to generate a large amount of thrust at low speeds, the propeller-driven aircrafts require shorter take-off/ landing lengths and climb time, making it attractive for airports with shorter runways. This has been advantageous for the airline operators to open new routes to the smaller destinations, thus, enhancing the regional connectivity. The aforementioned advantages of propellers have led to the wide use of turboprop aircraft for regional transport over short distances in civil aviation.

(a) Bombardier Q400

(b) Artistic impression of NASA X-57 Maxwell Electric Airplane

Figure 1.2: Propeller-driven aircraft.

In the present day scenario, aviation industry faces a new challenge to meet the rapid growth in the number of passengers while meeting the environmental regulations set by regulating authorities. To cater to the strong growth in the number of passengers in the future, the consequent increase in the number of flights is obvious, leading to an inherent rise in the emissions. According to ACARE's [1] forecast, the air traffic will grow by a rate of 4-5% annually and 16 billion passengers will be plying annually via air transport by 2050. To keep the effect of aviation on the environment in check, ACARE aims to introduce new technologies as well as enhance the current ones, to cut down the CO_2 and NO_x emissions per passenger kilometer by 75% and 90% respectively by 2050. It aims to achieve a reduction in noise emissions from aircraft by 65%. The growth in air traffic is driven by the creation of new routes in the coming years, especially the regional routes. As per the market forecast, there is a continued demand for the turboprop aircraft as the regional traffic is expected to grow by 4.5% annually up to 2037 [44]. This has led to a renewed interest in propeller research to meet the emission goals. Given the efficient operation of the propeller system, the novel propulsion technologies are being integrated with the propeller to derive different electric-, hybrid-, and hydrogen-powered aircraft. With the substantial increase in propeller-driven aircraft, the inherent rise in emissions is apparent. Therefore, to adhere to the emission standards set by the regulatory authorities, it is of great importance to study the design of the propeller blades to develop optimal propeller designs for aerodynamically efficient operations of turboprop aircraft.

1.2. Sensitivity Analysis using Adjoint Methods

The capability of the computational simulations to predict the fluid flow over a surface has been widely used in the design process of aerodynamic configurations. The Computational Fluid Dynamics (CFD) aids the designer by bridging the pure theory with the wind tunnel experiments, by solving the Navier-Stokes equations to obtain approximate results for a real-world phenomenon. As the field of CFD has matured over the years, accurate aerodynamic prediction methods are being used predominantly in the design process as compared to the wind tunnel tests, which is a comparatively expensive process. Computational simulations are extensively used in evaluating several alternative designs during the design phase, but it is also difficult to perform such an exhaustive evaluation of the possible design variations without incorporating automated numerical design methods with it.

As stated by Jameson et al. [45], the true potential of CFD is realized by combining its capabilities with the numerical design methods to produce optimum and efficient configuration based on the design of interest. Such a coupling between the CFD analysis tools and the numerical methods can be implemented in performing optimization and sensitivity studies of the aerodynamic designs. Such an approach was emphasized by Sobieski [50], to extend the capabilities of CFD for performing sensitivity analysis. Sensitivity analysis can lay the design guidelines and aid the design team, by determining the influence of each of the design variables over the key aspects of the design. The gradient information derived from such sensitivity studies can be useful while working on aircraft design, where the inputs from multiple disciplines have to be integrated.

The sensitivity analysis plays a fundamental role in the gradient-based optimization algorithms which are commonly employed to solve the aerodynamic optimization problem. The efficient and accurate computation of the sensitivity gradients of the objective function with respect to design variables is central to the success of the gradient-based optimization studies. It dictates the direction in which the design variable must be changed to achieve the convergence of the objective function. There are several approaches to evaluate the sensitivities, some of the commonly used are- Finite Differences, Complex Variable Approach, Direct Methods, and Adjoint Methods.

The Finite Differences can be used to compute the gradient vector, but this approach comes at the cost of computing one flow solution for each design variable, thus, leading to prohibitively expensive computational cost for the aerodynamic designs involving a large number of design variables. Such a computationally expensive process can be circumvented by implementing the adjoint method. The gradient vector through adjoint method implementation is computed by solving an adjoint equation that has the coefficients defined by the solution of the flow equation, where the computational cost of solving the adjoint equation is comparable to that of solving the flow equations [26]. Thus, the complete gradient vector is computed at a computational cost of two flow solutions while being independent of the number of design variables. Pironneau [42] was first to implement adjoint method in the field of fluid mechanics to derive adjoints of the Euler equations. Jameson's work [24] further extended this method to compressible inviscid flow. Finally, Nielsen and Anderson [36] and Jameson et al. [25] applied the adjoint method to Navier-Stokes equations. Since then, the advantage of the adjoint method has led to its wide use in the gradient-based optimization of aerodynamic designs.

1.3. Propeller Performance Methodologies in Design Studies

As aforementioned in the Section 1.1.1, the spur of development of the propeller due to increased emphasis on the fuel efficiency of the aircraft, different numerical methodologies were adopted to design a an optimal propeller. A brief review of the some of the methodologies used for predicting the propeller's aerodynamic performance coupled with optimization methods have been presented here. Most of the classical propeller performance theories have proceeded from Rankine-Froude's simple momentum theory, according to which the propeller is assumed as a disc with an infinite number of blades and produces a uniform change in the velocity and pressure of the streamwise flow passing through the disc. This simple theory doesn't account for the blade geometric properties and is useful for determining the theoretical efficiency of the propeller. The details of the propeller are considered in the blade element analysis as it computes the resultant velocity at each local airfoil section of the propeller blade using the inflow velocity and rotational velocity component. It is further used to determine the local angles of attack at different sections along the radial span of the blade. The theoretical prediction of thrust and torque values are within 10% of the measured thrust and torque values [28]. Several extensions to the basic theory have been formulated by including the hub/tip losses, swirl corrections, rotational corrections, etc.

The blade element theory is one of the most commonly used low-fidelity methods incorporated in the propeller design studies. Several numerical optimizations applied to propeller blade design couple the blade element theory with an optimization routine to design optimal blades. Bernstein's [4] feasibility study and Mendoza's [33] work were one of the first works to incorporate the blade element theory with a gradient based numerical optimization method to obtain optimal propeller design.

Further, vortex theory was developed based on the simple blade element theory and the momentum theory analysis that accounts for the influence of the vorticity in the slipstream. This method yields propeller's performance parameters more precisely as the thrust and torque values are computed based on the induced velocities. While Goldstein's lifting line model is based on modelling the propeller blade as a series of horseshoe vortices. An exhaustive comparison between the forgoing classical propeller modelling methodologies is presented by Zondervan [60]. Similar to blade element theory, the vortex theory and lifting line theory have been implemented to perform propeller shape optimizations such as work by Zhen et al.[59] used to estimate the optimal efficiency of the blade based on variation of number of blades, operating speed and blade radius. Cho and Lee [8] implemented vortex lattice method along with lifting surface theory to determine the propeller blade design to achieve improvement in efficiency.

The applicability of the above-mentioned theoretical methods came with certain limitations as outlined by Korkan et al.[28]. For example, for accurate performance prediction of the high-speed propellers, importance must be given to the wake modelling and propeller-nacelle interaction while using the lifting line model. Additionally, the centrifugal viscous effects on the lift coefficient are not accounted for, while using the 2D section data in blade element theory. This leads to differences in the prediction of the propeller's performance as first observed by Himmelskamp [23]. To compensate for the differences in the results and account for the 3D effects, different correction factors are used in the low-fidelity methods.

With the invent of the Computational Fluid Dynamics (CFD), a high-fidelity method allows to perform the aerodynamic analysis of the propeller by discretizing and solving the governing equations i.e., Navier-Stokes equations. By solving the mass and momentum equations, an accurate representation of the propeller flowfield and its resulting slipstream can be simulated. In comparison to the low-fidelity method, this is computationally expensive as the governing equations are solved on the computational mesh of the domain which is dependent on the mesh density. Based on the type of simulation, the time accurate and time-averaged simulations are performed. Amongst many propeller optimizations works, Marinus [30] incorporated steady RANS-based CFD model along with Evolutionary Algorithms to perform a multidisciplinary optimization of the propeller blades. Similarly, Yu et al. [40] used high fidelity CFD method to perform an aerodynamic and aeroacoustic optimization of the propeller blade with an implementation of a surrogate model.

Based on the works cited above, most of the design studies are aimed at optimizing the blade for a single design operating condition, except Marinus's work [30] where the blade is optimized for aerodynamic and aeroacoustic performance at take-off and cruise conditions. However, few design studies present a dedicated sensitivity analysis of the propeller's performance to the variation in shape design of the blade. In the past, works of Biermann and Hartman [5] and Platt[43] presented sensitivity of the propeller's performance with respect to change in airfoil blade sections and blade parameters by performing wind tunnel testing. With the advent of advance numerical methods and CFD similar study can be performed in a cost effective and less time consuming method. By coupling the high fidelity CFD tools with the gradient-based adjoint method, a multi-point sensitivity analysis can be useful to provide physical insights into the effect on the propeller's performance due to variation in the blade shape design.

1.4. Research Objective

Based on the foregoing sections, it can be inferred that there is a rise in the demand for the propeller driven aircraft whether hybrid, electric or turboprop. In the case of electric aircraft, the energy density of the battery remains limited, it is beneficial to study the propeller blade design to develop an aircraft with high efficiency. Likewise, an efficient design of propeller blade for a turboprop-driven aircraft is relevant to improve fuel savings and reduce emissions to adhere to the environmental regulations, as the passenger volume in air transport increases.

The project aims to develop a RANS-based CFD methodology incorporating adjoint method to perform the sensitivity analysis of the propeller's performance parameters with respect to the deformation of the blade shape, at different operating conditions. To meet the objective of the current research,

open-source multiphysics simulation and design software SU2, has been chosen based on its adjoint capabilities [14]. The research objective of the current study is-

"To perform aerodynamic and sensitivity assessment of isolated propeller blades using SU2's flow and adjoint capabilities, to gain an improved understanding of the effect of blade shape design on its aerodynamic performance."

To meet the above stated research objective, following goals have been outlined-

- Perform isolated propeller simulations to verify results of SU2's RANS-based CFD solver against that of commercial software, ANSYS Fluent.
- Perform isolated propeller simulations for the straight and swept blades to investigate the difference in the aerodynamic performance of the two blades.
- Perform adjoint-based sensitivity analysis of the isolated propeller configuration of the straight and swept blades with - a) thrust and b) torque as the objective functions and assess the effect on the shape deformation on the objective functions.

The outcomes of this work will be a preliminary step of the research field aimed at developing adjoint-based multidisciplinary design capabilities for propellers.

1.5. Report Outline

The current report has been summarized into several chapters as explained here. Chapter 2 summarizes the theory related to the basic principles of aerodynamics of an isolated propeller. It also presents the review of available aerodynamic analysis models for modeling the propeller flow and estimating the propeller's aerodynamic performance. Chapter 3 presents a discussion on sensitivity analysis, with an emphasis on the adjoint-method. The geometry of the propeller test cases and setup of the RANS based CFD solver is presneted in 4. Chapter 5 presents a verification and validation of SU2's flow solver. It also presents the comparison and discussion on the aerodynamic performance of the swept and unswept propellers. Chapter 6 presents the presents the results obtained from adjoint-based sensitivity analysis of the propeller test cases. Chapter 7 concludes the report by presenting conclusions and recommendations based on this research.

2

Basic Propeller Theory and Aerodynamics Analysis Methods

The current chapter presents an overview of the working principles of an isolated propeller along with the methods used to perform the aerodynamic and performance analysis of the propeller. The fundamental working of the propellers and the parameters used to adjudge its performance are discussed in Section 2.1. Section 2.2 presents a discussion on the RANS CFD solver used for aerodynamic and performance analysis in this research, with relevant governing equations and closure models.

2.1. Basic Propeller Theory

To analyze the performance characteristics of an isolated propeller, the aerodynamics of the propeller and key non-dimensional parameters are discussed in the current section.

2.1.1. Isolated Propeller Aerodynamics

A propeller-driven aircraft is propelled by converting shaft power to propulsive power. The propeller can be defined as a set of rotating lifting surfaces, radially arranged at the hub of the shaft. A propeller blade is essentially an assembly of airfoil sections with variation in twist, chord, and thickness from hub to tip as shown in Figure 2.1.

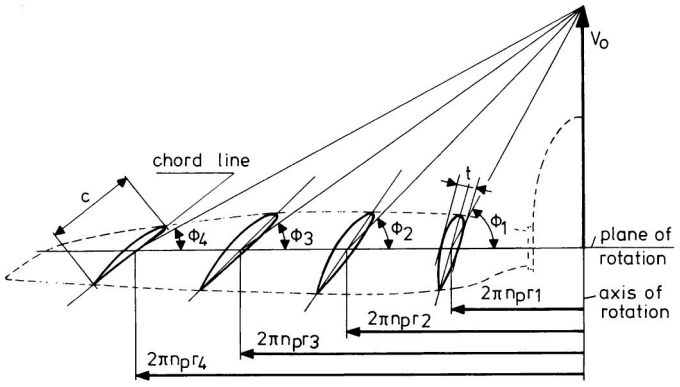

Figure 2.1: Variation of the blade geometry parameters along propeller blade [46].

As a blade can be discretized into a set of airfoils stacked from hub to tip, the aerodynamics of the blade can be studied by decomposing the forces acting on each of the blade section. On rotation of the propeller, each independent section of airfoil along the length of the blade produces lift and drag. The thrust and torque are a consequence of the these forces, since these forces experience an angle of attack

due to the translation and rotation of the blade. The velocity and resulting forces at a propeller blade section are illustrated in Figure 2.2.

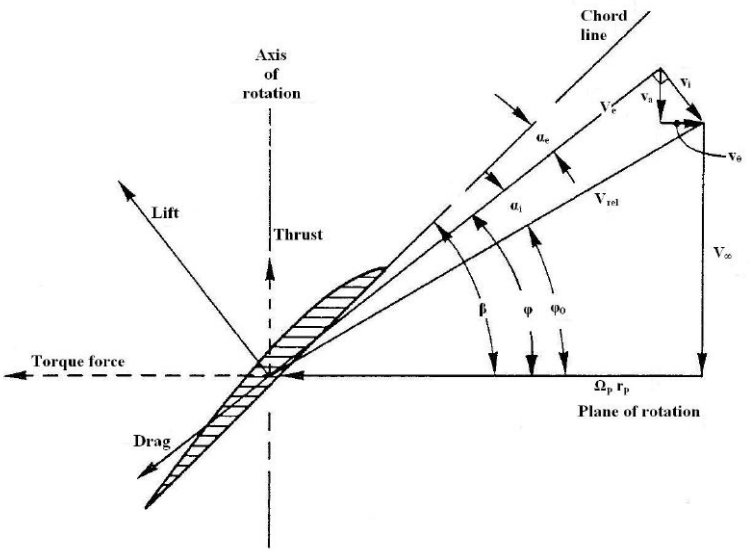

Figure 2.2: Velocity and force diagram acting on a blade element of a propeller [32].

The propeller generates thrust by inducing small velocity increments to a large amount of flow passing through the propeller, resulting in high efficiency. In accordance with the momentum theory, as the airflow passes across the propeller, the slipstream contracts downstream as shown in Fig.2.3(a). It can be inferred from Fig. 2.3(b) and 2.3(d) the propeller accelerates the flow leading to a drop in the static pressure. This causes a discontinuous rise in total pressure across the propeller disk as seen in Fig. 2.3(c).

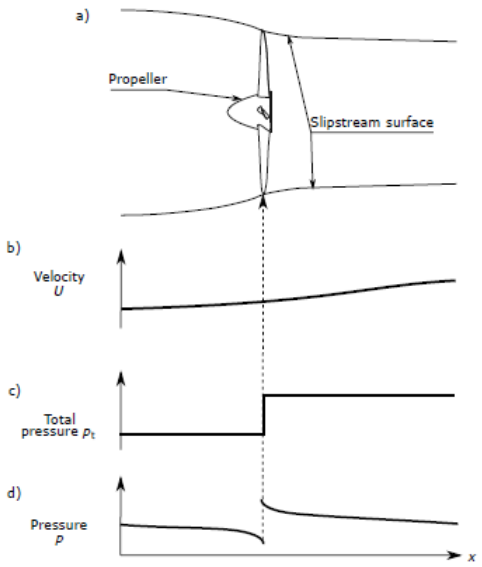

Figure 2.3: Illustration of actuator disk theory based on momentum theory: a) Slipstream contraction, b) Velocity variation, c) Total pressure variation, d) Static pressure variation across the propeller [32].

2.1.2. Propeller Performance Parameters

The propeller performance is adjudged by using non-dimensional parameters as mentioned below-

- Advance Ratio - It is a ratio of the freestream velocity of the fluid and tip speed of the propeller. Advance ratio of a propeller captures the forward motion traversed per unit rotational speed of the propeller and is given by:

$$J = \frac{V_\infty}{n.D} \tag{2.1}$$

  where v_∞ is the freestream velocity, n represents spinning rate and D is the diameter of the propeller.
- Thrust Coefficient- The thrust coefficient is given by:

$$C_T = \frac{T}{\rho.n^2.D^4} \tag{2.2}$$

  where T represents propeller thrust and ρ is the density of flow.
- Power Coefficient- The power coefficient is given by:

$$C_P = \frac{P}{\rho.n^3.D^5} \tag{2.3}$$

  where P is the shaft power of the propeller.
- Efficiency- Efficiency of a propeller is defined as a ratio of the effective power and shaft power. The efficiency of a propeller is given by:

$$\eta = \frac{T.V_\infty}{P} = \frac{T.V_\infty}{2\pi Q} \tag{2.4}$$

  where Q is the torque delivered.

2.2. RANS-based Aerodynamics Analysis Solver

An aerodynamic solver is used to model the propeller flow and estimate propeller performance along with various flow details. Based on the theoretical ability to model the physical effects of the propeller aerodynamics and the level of sophistication, several aerodynamic prediction methods are available. The 2D-based propeller prediction methods such as Blade element momentum theory (BEMT) or Vortex Lattice Method (VLM) give relatively cheaper in terms of the computational time as compared to 3D-CFD methods. But, they can't capture the flow physics around the propeller as accurately as CFD methods. CFD analysis methods are based on the equations governing the motion of fluid flow which are derived from the conservation laws. The techniques used for modelling the flow by resolving these governing equations, that is, RANS, DES, and LES.

In the current section, governing equations and turbulence modelling has been reviewed. Since the current study pertains to the use of RANS-based solver for aerodynamic analysis, an elaborated description of the governing equations and closure models is presented. Arguments concerning the choice to implement RANS-based solver for the computation of the flow field around the propeller is described in the following section.

2.2.1. Governing Equations

The governing equations for compressible viscous fluid are derived from the laws of conservation of mass, momentum and energy expressed within the confines of the continuum hypothesis. A finite control volume is considered in the space, through which fluid flows. The finite control volume can be considered to be stationary or moving. The equations are presented in the form of differential equations.

Conservation of mass

The law of conservation of mass states that total quantity of mass entering the control volume per unit time is equal to the total quantity of mass leaving the control volume per unit time. The conservation of mass is described using continuity equation and is given by,

$$\frac{\partial \rho}{\partial t} + \frac{\partial(\rho u_i)}{\partial x_i} = 0 \tag{2.5}$$

where t denotes time, u_i and x_i are velocity and i^{th} direction in the Cartesian coordinate respectively.

Conservation of momentum
Law of conservation of momentum is described using Newton's second law of motion which states that the rate of change of momentum of the fluid in a control volume is due to the total flow of the momentum into the domain and external forces acting on the fluid within the control volume. The external forces can be further divided into the body and surfaces forces. The equation for the conservation of momentum for a compressible viscous flow is given by,

$$\frac{\partial(\rho u_i)}{\partial t} + \frac{\partial(\rho u_j u_i)}{\partial x_j} = -\frac{\partial p \delta_{ij}}{\partial x_i} + \frac{\partial \tau_{ij}}{\partial x_j} + f_i \tag{2.6}$$

where δ_{ij} is the Kronecker delta function, τ_{ij} denotes deviatoric stress tensor and f_i is the body force. In propeller applications, body forces are often not considered in absolute frame of reference.

Conservation of energy
Conservation of energy is described using first law of thermodynamics, which states that the energy can neither be created nor be destroyed and can only be transformed from one form to another. The energy conservation equation is given by,

$$\frac{\partial(\rho e_o)}{\partial t} + \frac{\partial(\rho u_j e_o)}{\partial x_j} = -\frac{\partial u_j p}{\partial x_j} + \frac{\partial u_i \tau_{ij}}{\partial x_j} - f_i u_i + \dot{q} \tag{2.7}$$

where e_o denotes total energy which is expressed as, $e_o = e + \frac{1}{2}\rho u^2$. $\dot{q}$ represents the heat flux, which is neglected in the current research.

2.2.2. Turbulence Modeling & Simulation

Turbulence Scales
Turbulent flows with sufficiently high Reynolds number are characterized by a spectrum of eddies or vortices with varying dimensions in space and time. The dimensions of the eddies have an upper bound dictated by the dimension of the device or confinement of the flow field and the lower bound is dictated by the dimension of the scale at which the diffusive action of molecular viscosity dominates. Integral scale eddies are related to the large scale instabilities in the turbulent flow and are created by extracting energy from the mean flow motion [29]. The integral scale eddies are unstable and break up into smaller eddies until a certain scale is reached where viscous dissipation becomes effective.

As the concentration of the turbulent kinetic energy is largest in the neighborhood of integral scales, these eddies are also called energy-containing eddies. Eddies at different scales contain different amounts of turbulent kinetic energy which is determined by the intensity of the velocity fluctuation at a given scale. The kinetic energy is transferred from the eddies at one scale to another through the concept of energy cascading. According to the energy cascade concept, for the turbulent flows with high Reynolds number, there exists a range of scales for which the rate of energy transfer is independent of the viscous dissipation. This range of scale through which the turbulent kinetic energy is transferred from integral scales to smaller ones is called inertial sub range. The rate of energy transfer from the integral scale to the dissipative scales is given by,

$$\epsilon = \frac{u'^3}{l_0} \tag{2.8}$$

where, ϵ is the energy transfer rate, u' is the characteristic velocity fluctuation, and l_0 is the integral length scale. The kinetic energy from the integral scale eddies is supplied to smaller scales at a rate ofϵ until eddies at dissipative length scale are reached where viscous dissipation dominates. This dissipative length scale is called the Kolmogorov scale, η_k. Following energy conservation, the rate of energy dissipation from the Kolmogorov eddies must be equal to the rate of energy supplied from the integral scales. The Kolmogorov length scale is determined through dimensional analysis using energy transfer rate, ϵ and characteristic kinematic viscosity of the fluid ν,

$$\eta_k = \left(\frac{\nu^3}{\epsilon}\right)^{1/4} \tag{2.9}$$

By using the above relations, the relation between integral scale and Kolmogorov scale is determined and is given by,

$$\frac{l_0}{\eta_k} = Re^{3/4} \tag{2.10}$$

where Re is the Reynolds number. The equation implies that disparity between the integral scale and Kolmogorov scale increases with the turbulent Reynolds number. Thus, the turbulent flows with high Reynolds number consist of eddies with a wide range of length scales. Therefore, making it computationally expensive to directly solve the Navier-Stokes equations for flows with high Reynolds number.

Turbulence Modeling
The governing equations of the turbulent flows can be solved using different computational simulation and modeling approaches, namely- Direct Numerical Simulation (DNS), Large Eddy Simulation (LES), and Reynolds-averaged Navier-Stokes (RANS). These approaches differ from each other based on how one resolves the turbulent structures in the flow.

Out of the aforementioned computational approaches, DNS involves the most rigorous treatment of the turbulent flow as it provides a direct solution to the Navier-Stokes equations. It yields solutions to the governing equation free from the errors that occur due to turbulence modelling. It accurately resolves all the scales present in the turbulent flow, but at the expense of enormous computational demand. For homogenous isotropic turbulence, the computational cost of DNS scales with Re^3, making it infeasible to computationally resolve a three-dimensional turbulent flow with high Reynolds number [16].

LES is an alternative approach used for simulating the turbulent flows, which is computationally less expensive than DNS. LES accurately resolves the integral scales, which contains more energy than smaller scales, and invokes turbulence models to model the effects of smaller scales. It is based on the assumption that as one proceeds from largest to smallest scales, the smaller scales become increasingly geometry-independent. At a certain small scale, flow is isotropic and the turbulence is modelled using an isotropic model. Although LES is computationally less expensive than DNS, implementing it for the sensitivity analysis of an objective function remains computationally intensive.

RANS technique is based on the statistical approach where a flow quantity is decomposed into two parts- a mean and a fluctuating part. This approach is based on solving the mean part of all the flow quantities in the turbulent flow. In this implementation, the averaged quantities are obtained by averaging the non-linear Navier-Stokes equations, which must be modeled. The resulting averaged equations require additional turbulence models to accurately represent the flow dynamics of a turbulent flow.

Even though one has an access to the DNS solution of a turbulent flow, the amount of information obtained, in space and time, is overwhelming and practically of little use. From the engineering point of view, most engineers are interested in knowing a few properties of a turbulent flow. Therefore, using the LES and DNS approach to compute these quantities is infeasible and RANS results as a reasonable compromise between the computational load and accuracy. In the proceeding section, the RANS approach with relevant closure models will be presented in detail.

2.2.3. Reynolds Averaged Navier-Stokes based Solver

The inherent randomness of turbulent flows can be analyzed and modeled using statistical approach by averaging the non-linear Navier-Stokes equations. The RANS-based approach is based on decomposition of the flow quantity of the governing equations into its mean component and time-dependent fluctuating component. The RANS equations are derived with a combination of two types of averages- Reynolds average and Favre average (density-weighted average), where the latter is used for compressible flows. Equation 2.11 depicts the decomposition of the flow quantity ϕ into its mean part $\overline{\phi}(x,t)$ and fluctuating part $\phi'(x,t)$ using Reynolds averaging,

$$\phi(x,t) = \overline{\phi}(x,t) + \phi'(x,t) \tag{2.11}$$

Whereas, Favre averaging is used to split the flow quantity ϕ into its Favre mean $\tilde{\phi}(x,t)$ and Favre fluctuation $\phi''(x,t)$ as shown in Equation 2.12.

$$\phi(x,t) = \tilde{\phi}(x,t) + \phi''(x,t) \tag{2.12}$$

The Favre mean is given by equation 2.13,

$$\tilde{\phi}(x) = \frac{\overline{\rho\phi}}{\overline{\rho}} \tag{2.13}$$

where, ρ is the density, thus, representing a density weighted average. In the above decompositions of the flow variable in equations 2.11 and 2.12, the mean part of the flow quantity can be derived using different forms of Reynolds averaging, namely- time averaging, spatial averaging and ensemble averaging. In the current study, time averaging is used for the computation of the mean part of the flow quantity.

The averaged form of the Navier-Stokes equation is obtained by applying Reynolds averaging to p and ρ, and Favre averaging to the velocity and remaining flow quantities in the equation. The resultant averaged equations are presented in the Einstein notation using Cartesian coordinates,

$$\frac{\partial\overline{\rho}}{\partial t} + \frac{\partial(\overline{\rho}\tilde{u}_i)}{\partial x_i} = 0 \tag{2.14}$$

$$\frac{\partial(\overline{\rho}\tilde{u}_i)}{\partial t} + \frac{\partial(\overline{\rho}\tilde{u}_j\tilde{u}_i)}{\partial x_j} = -\frac{\partial(\overline{\rho u_j'' u_i''})}{\partial x_j} - \frac{\partial\overline{p}}{\partial x_i} + \frac{\partial\overline{\tau_{ij}}}{\partial x_j} + f_i \tag{2.15}$$

$$\frac{\partial(\rho e_o)}{\partial t} + \frac{\partial(\rho u_j e_o)}{\partial x_j} = -\frac{\partial u_j p}{\partial x_j} + \frac{\partial u_i \tau_{ij}}{\partial x_j} - f_i u_i \tag{2.16}$$

In addition to the averaged flow quantities, the averaged equations also include the additional terms representing the exchanges between the fluctuating quantities. These additional terms are Reynolds stress and turbulent scalar flux. The occurrence of these additional terms leads to a closure problem, where the number of unknowns are more than equations and the system of equations remains unclosed. Consequently, additional relations are needed to model these terms and close the system of equations.

Bosinuessq eddy viscosity assumption is a viable approach to take the aforementioned closure problem. This hypothesis for the turbulent transport of flow quantities is based along the lines of molecular diffusive transport. This approach is based on the assumption that the shear stress is linearly proportional to the mean rate of the strain. The Reynolds stress can be written as,

$$-\overline{\rho}\widetilde{u_i'' u_j''} = 2\mu_T\tilde{S}_{ij} - \frac{2}{3}\mu_T\tilde{S}_{kk}\delta_{ij} - \frac{2}{3}\overline{\rho}\tilde{k}\delta_{ij} \tag{2.17}$$

$$\tilde{S}_{ij} = \frac{1}{2}\left(\frac{\partial\tilde{u}_i}{\partial x_j} + \frac{\partial\tilde{u}_j}{\partial x_i}\right) \tag{2.18}$$

where μ_T is the turbulent viscosity coefficient, δ_{ij} is the Kronecker delta, and S_{ij} is the strain rate tensor. The turbulent heat transport term is defined as;

$$\overline{\rho}\widetilde{u_j'' h''} = -\kappa_T\frac{\partial\tilde{T}}{\partial x_j} \tag{2.19}$$

where κ_T is the turbulent thermal heat conductivity. To model the turbulence using the Boussinesq hypothesis, the total viscosity, μ, is written as a sum of the laminar component, μ_{dyn}, and a turbulent component, μ_{tur}.

$$\mu = \mu_{dyn} + \mu_{tur}, \quad \mu^* = \frac{\mu_{dyn}}{Pr_d} + \frac{\mu_{tur}}{Pr_t} \tag{2.20}$$

where Pr_d and Pr_t are the dynamic and turbulent Prandtl numbers, respectively. To close system of equations, the dynamic viscosity is determined using Sutherland's law, whereas, the turbulent viscosity is estimated through a turbulence model.

There are multiple turbulence models available to close the system of equations. SU2 suite presents two turbulence models for the analysis and modeling of turbulent flow applications- one-equation Spalart Allmaras (S-A) and other being the two-equation Shear Stress Transport (SST) model of Menter.

Closure Model: Spalart Allmaras (S-A) model
The Spalart-Allmaras model is a one-equation model used to compute the turbulent viscosity [51]. It is formulated to accurately model the applications involving wall-bounded flows. The turbulent viscosity is computed using the following set of equations,

$$\mu_{tur} = \rho\tilde{\nu} f_{v1}, \quad f_{v1} = \frac{\chi^3}{\chi^3 + c_{v1}^3}, \quad \chi = \frac{\hat{\nu}}{\nu}, \quad \nu = \frac{\mu_{dyn}}{\rho}. \tag{2.21}$$

where the $\tilde{\nu}$ is the transport variable and obtained by solving the transport equation. The S-A model effectively is a low Reynolds number model, requiring the near-wall y^+ resolution to be properly resolved to $y^+ \sim 1$. Even though the S-A model is computationally cheaper, but it faces issues in dealing with recirculation and flow separation.

Closure Model: Shear Stress Transport (SST) model
The Shear Stress Transport (SST) model by Menter [34] is a two-equation model for the turbulent kinetic energy, k, and the specific dissipation, ω. This model combines the superior features of two traditional models, i.e., accurate modeling of the near-field in $k-\omega$ model and freestream independence of the$k-\epsilon$ model in the far-field region. The turbulent viscosity is computed using,

$$\mu_{tur} = \frac{\rho a_1 k}{max(a_1\omega, SF_2)} \tag{2.22}$$

where a_1 is the model constant, $S = \sqrt{2S_iS_j}$, and F_2 is the second blending function. This model is suitable for the wide range of flow applications involving the presence of adverse pressure gradients and shocks. SST model has been widely used in the modeling of the propeller flow field.

3

Adjoint-based Sensitivity Analysis Methodology

The current chapter presents the design chain, governing equations and the processes involved in the discrete adjoint-based sensitivity analysis. Section 3.1 present a brief methodology of the computation of the sensitivities in aerodynamic design process. A discussion on the surface parameterization and mesh deformation techniques, which are of fundamental importance to the sensitivity analysis is presented in Section 3.2 and 3.3 respectively. Section 3.4 presents the discrete adjoint sensitivity equations. Finally, a discussion on the interpretation of the adjoint sensitivities is presented in Section 3.5.

3.1. Sensitivity Analysis Methodology

Sensitivity analysis is the process of computing the derivatives of one or more output quantities with respect to several independent input variables. In a design-based study of aerodynamic applications, the output quantities refer to objective and constraint functions of interest, while design variables defining the geometry are used as the input. Such a capability to determine the sensitivity information is highly desirable for performing-design optimization, error estimation, and parameter sensitivity.

In an aerodynamic design-based application, the objective function, J, can be defined as,

$$\begin{aligned} J &= J(X, \alpha) \\ where \quad X &= X(X_{surf}, \alpha) \end{aligned} \tag{3.1}$$

where, α represents the vector of the design variables, X_{surf} represents the surface grid coordinates,and X represents the volumetric grid. Eq.3.1 shows the dependence of the objective function of the interest on the the design variables α. Similar dependence can be depicted through the schematic of the fluid dynamic design chain as shown in Figure 3.1.

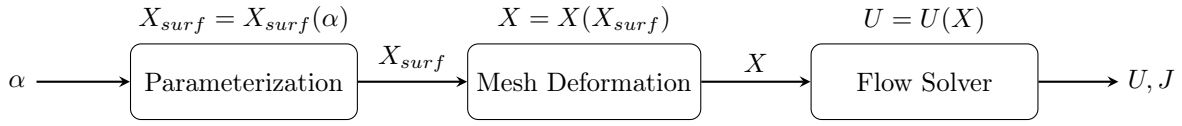

Figure 3.1: Schematic of fluid dynamic design chain for objective function computation.

The parameters in the design vector, α, depend on the parameterization method that is used to define the geometry. A variation in the design vector leads to a change in the surface coordinates, X_{surf}, which is translated into the movement of the volume mesh, X. The deformed mesh is given as an input to the flow solver to compute the flow variables, U, and objective function of interest, J.

The schematic representation of the gradient computation of the total gradient is shown in Figure 3.2. As can be inferred from Figure 3.2, the gradients from different modules of the design chain are used as an input to compute the total gradient, $\frac{dJ}{d\alpha}$. The parameterization tool uses the vector of the design variables as input and computes the sensitivity of the surface coordinates with respect to the

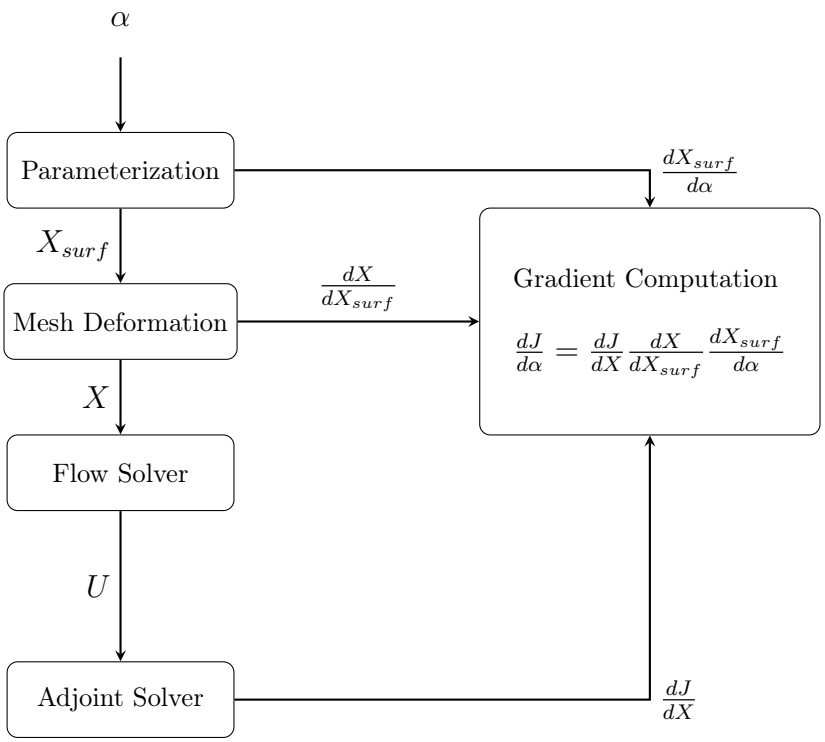

Figure 3.2: Schematic of gradient computation of the total gradient.

design variables, $\frac{dX_{surf}}{d\alpha}$. The mesh deformation algorithm computes the mesh sensitivities, $\frac{dX}{dX_{surf}}$. Using the flow solution U as an input from the flow solver, the adjoint solver computes the adjoint variables. Based on the adjoint values, the sensitivity of the objective function with respect to the volumetric grid coordinates, $\frac{dJ}{dX_{surf}}$, is further computed. The total gradient is computed by using the inputs from different modules and given by,

$$\frac{dJ}{d\alpha} = \frac{dJ}{dX}\frac{dX}{dX_{surf}}\frac{dX_{surf}}{d\alpha} \tag{3.2}$$

3.2. Surface Parameterization

Parameterization is the process of mathematically modeling the geometry under study. It is a crucial step in the shape optimization process of the design phase, as it impacts the formulation and the implementation of the optimization problem [47]. The parametrization must account that the design space is large enough to include the optimal designs while keeping geometric limitations in place. As the complexity of the geometry increases, it becomes necessary to model the problem with an accurate and consistent shape parameterization technique, yielding compact and effective sets of design variables. The selection of a suitable parameterization method is a highly problem-dependent process. Various shape parameterization techniques have been proposed and implemented in the design studies of aerodynamic applications, which have been surveyed and reviewed by Samareh [47]. Some of the shape parameterization techniques have been discussed below-

- Discrete Method- The discrete method parameterizes the shape of the blade by using the coordinates on the surface grid as the design variables. It is the simplest way to parameterize the geometry and leads to rich design space, thus, theoretically making it possible to represent any shape. Jameson [24] and Campbell [7] had implemented this approach to parameterize the airfoils. This method leads to a large number of design variables and it is difficult to maintain a smooth geometry. Additionally, the requirement for multipoint constraints and dynamically adjusting the bounds to ensure the smoothness of the airfoil, makes this complex and infeasible to apply.
- Analytical Approach- Analytical approach is based on a linear combination of basis functions and

a set of perturbation functions added linearly to the geometry surface, either defined analytically or numerically. Hicks-Henne's [22] shape function method is one of the most common analytical methods used. Hicks-Henne shape function consists of 'bumps' defined by equation 3.3.

$$Y = sin^3(X^\beta) \tag{3.3}$$

where, β is used to control the position of the bump in the chord-wise direction of an airfoil. The drawback of this method is that it lacks robustness as the change in shape due to the change in the perturbation function is non-intuitive [55]. An extra set of perturbation function is required to make the approach efficient.

- CAD-based Methods- CAD-based methods employ B-spline and/or NURBS to generate the curve and surfaces of a blade geometry, whose control points are directly derived from defining the characteristics and design parameters of the blade (such as thickness distribution, blade chord, etc.) [3]. This approach allows defining the geometry intuitively which are related to the aerodynamic design variables (camber, twist, thickness, etc.) and therefore making this approach ideal for parametric changes in the geometry.

  The main advantage of this method is its easy implementation of the geometrical constraints. However, this comes at the cost of narrowing down the design space. Additionally, the computation of the sensitivities is a challenge [56].
- Free-Form Deformation Methods- This method is based on the surface morphing technique which is used to deform the solid models. In FFD method, the geometry of interest is encapsulated within a lattice box and the box is parameterized as a Bezier box [12]. The surface of this box is divided into a set of control points, the number of which depends on the order of the chosen Bernstein polynomials. The expression in equation 3.4 is used to parameterize the Bezier box.

$$X(u,v,w) = \sum_{i,j,k=0}^{l,m,n} P_{i,j,k} B_j^l(u) B_j^m(v) B_j^n(w) \tag{3.4}$$

where $u, v, w \in$ [0,1] and B^i represents the Bernstein polynomial of order i. The Cartesian coordinates of the points on the surface of the geometry in the physical space are transformed into the parametric space of the FFD box (Bezier box). The control points of the box are used as the design variables, which on perturbation deform the box, and thus deforming the enclosed geometry. On deformation, the new Cartesian coordinates of the enclosed geometry can be calculated using the equation 3.4.

Yu et al.[40] and Pagano et al. [37] implemented this method of parameterization in the optimization of a propeller blade. As stated by Samareh [47], although FFD methods are suitable for parameterizing complex geometries, it is hard to specify the optimization bounds and constraints as the designers have less intuitive control over the surface of the geometry.

Amongst the above stated parameterizations methods, SU2 offers two parameterization techniques for the definition of the design variables- Hicks-Henne's bump functions and Free-Form Deformation [12]. For two dimensional problems, Hicks-Henne bump functions are used for the modification of the shape. Whereas, FFD method is employed for the shape modification of the three-dimensional calculations. Additionally, there are works where the authors have integrated the different parameterization techniques such as CAD-based parameterization [2] and CST techniques [21] into SU2-based design cycle to perform optimization studies. Based on the literature cited above and the reduced complexity, FFD method has been adopted in the current research.

3.3. Mesh Deformation

In the sensitivity analysis and design optimisation studies, the design variables control the shape of geometry, and for every perturbation in the design variables, there is a corresponding change in the shape of the geometry. When the geometry undergoes a change, the volumetric mesh has to be deformed to confine the changing fluid domain. At each iteration, the change in the surface mesh is governed by

the parameterisation tool whereas the change in the volumetric mesh is implemented by either of the approaches: mesh regeneration and mesh deformation.

Mesh regeneration involves the deletion of the old mesh and regenerating a new mesh for every corresponding change in the shape of geometry, leading to higher computational requirements. Regenerating a new mesh at every time step requires special mesh quality controls and consumes high CPU cost making it an impractical approach. Moreover, mapping the solution from old mesh to new mesh consumes extra computational cost.

In comparison to the mesh regeneration, mesh deformation approach is computationally cheaper, more practical, and flexible. Spring analogy, linear elasticity, and radial basis functions are some of the commonly used mesh deformation approaches. SU2 employs spring method to perform mesh deformation. Once the perturbation is performed using the FFD method, the vertices of the unstructured mesh are deformed using the spring method. This method is essentially based on the definition of the stiffness matrix connecting two ends of the spring, mesh edge in this case. Each mesh node is subjected to equilibrium forces suing the following equation 3.5,

$$\left(\sum_{j\in N_i} k_{ij}\,\overrightarrow{e}_{ij}\,\overrightarrow{e}_{ij}^{T}\right)\overrightarrow{u_i} = \sum_{j\in N_i} k_{ij}\,\overrightarrow{e}_{ij}\,\overrightarrow{e}_{ij}^{T}\overrightarrow{u_j} \tag{3.5}$$

where, k_{ij} is the stiffness matrix, $\overrightarrow{u_i}$ is the unknown displacement, $\overrightarrow{u_j}$ known surface displacement, N_i represents the set of neighboring points to node i, and $\overrightarrow{e}_{ij}$ represents the unit vector in the direction connecting two points. The known surface displacements $\overrightarrow{u_j}$ are used to compute the unknown displacements $\overrightarrow{u_i}$. Conjugate gradient algorithm with Jacobi preconditioning is used to solve the system of equations iteratively.

3.4. Adjoint-based Sensitivity Analysis

Sensitivity analysis is a computationally intensive operation and dictates the efficiency of an optimization process. Based on the problem definition of shape optimization, an appropriate analysis approach is chosen for the calculation of the sensitivities. The adjoint method is a highly efficient and effective approach to computing sensitivity derivatives of the function of interest with respect to a large number of design variables. As will be explained through the mathematical formulation in the current section, the implementation of the adjoint method leads to the computation of accurate derivatives at a cost independent of the number of design variables.

The adjoint equation for a set of PDEs can be formulated using two approaches- continuous and discrete. In the continuous approach, adjoint equations are obtained by differentiating the PDEs followed by discretizing them to solve them numerically. Whereas, in the discrete approach, the PDEs are discretized followed by linearizing them to obtain adjoint equations.

3.4.1. Continuous vs. Discrete Adjoint Approach

The wealth of early works on adjoint implementations used the continuous approach which includes the initial implementations of the adjoint methods in SU2 [14] and OpenFOAM [20] and works of Jameson et. al.[25]. The continuous approach generates the linearized PDEs which can be solved using the same numerical iteration techniques as the primal flow solution, thus, eliminating the need to form the Jacobian leading to faster and low-memory adjoint implementations[27]. Whereas, the resulting low accuracy for coarser meshes and the challenging implementation are some of the disadvantages of this approach. Also, the PDEs of the continuous adjoint systems need to be differentiated by hand, which can be challenging for some terms. Moreover, the boundary conditions of the linearized PDEs are not always obvious and require careful consideration.

Lately, much of the adjoint work has made use of the discrete adjoint approach. The main advantage of this approach is that it generates derivatives that are numerically consistent, irrespective of the coarseness of the mesh as it is formulated from the discretized flow equations. Additionally, the partial derivatives appearing in the discretized adjoint equations can be computed using several numerical methods such as- Algorithmic Differentiation (AD), Complex step, and Finite differences; and do not necessarily need to be hand differentiated [27]. While the disadvantage of the discrete adjoint approach is the high computational cost and memory allocation, due to the need to compute and store the exact

Jacobian. Therefore, to yield good adjoint performance, it is necessary to implement such computations efficiently.

3.4.2. Adjoint method

The current subsection briefly presents a mathematical formulation of the adjoint method. As aforementioned, in the adjoint-based sensitivity analysis of a fluid-dynamic design problem, the objective function to be analyzed has a non-linear dependence on the discrete variables. The objective function depends on the physical and geometric design variables α, state variables U, and grid points X. State variables U comprises of conserved flow variables attained from the solution of the flow governing equations computed at grid points of an unstructured mesh. The state variables depend on the physical and geometrical design variables, whereas, the grid points only depend on the geometrical design variables. In practice, the physical design variables are neglected in a design process and hence neglected. The objective function can be stated as,

$$J = J[U(\alpha), X(\alpha)] \tag{3.6}$$

where U vector consists of the state variables that satisfy flow governing equations for the given vector of design variables α. The residuals of the discretized flow governing equations is expressed as,

$$R[U(\alpha), X(\alpha)] = 0 \tag{3.7}$$

where Equation 3.7 is equivalent to zero and it is an equality constraint.

Using the chain rule, the total gradient of the objective function with respect to the geometric design variables can be expressed as,

$$\frac{dJ}{d\alpha} = \frac{\partial J}{\partial U}\frac{\partial U}{\partial \alpha} + \frac{\partial J}{\partial X}\frac{\partial X}{\partial \alpha} \tag{3.8}$$

where it is relatively cheaper to compute the term $\partial J/\partial U$ as compared to the term $\partial U/\partial \alpha$. The computation of the sensitivity of the state variable to the variation in the geometric variable, $\partial U/\partial \alpha$, is a computationally intensive operation. Implementation of finite difference method to compute $\partial U/\partial \alpha$, is straightforward but not advisable as it is a computationally expensive method. Alternatively, to solve for $\partial U/\partial \alpha$, the total derivative of the residual of the discretized flow governing equations with respect to the geometric design variables is written as,

$$\frac{dR}{d\alpha} = \frac{\partial R}{\partial U}\frac{\partial U}{\partial \alpha} + \frac{\partial R}{\partial X}\frac{\partial X}{\partial \alpha} = 0 \tag{3.9}$$

To maintain the equality constraint for the flow governing equations to be feasible, the total derivative $dR/d\alpha$ must be equivalent to zero. Equation 3.9 can be rearranged to obtain a linear system,

$$\left(\frac{\partial R}{\partial U}\right)\left(\frac{\partial U}{\partial \alpha}\right) = -\left[\frac{\partial R}{\partial X}\frac{\partial X}{\partial \alpha}\right] \tag{3.10}$$

The above equation can be used to compute the sensitivity $\partial U/\partial \alpha$, but it utilizes considerable amount of computational memory as we need to solve the linear equations N times, where N represents the number of columns in term $[\partial R/\partial X][\partial X/\partial \alpha]$ on right-hand side, which is equivalent to the number of geometrical design variables. Instead of solving the Equation 3.10, it can be rewritten as,

$$\frac{\partial U}{\partial \alpha} = -\left(\frac{\partial R}{\partial U}\right)^{-1}\left[\frac{\partial R}{\partial X}\frac{\partial X}{\partial \alpha}\right] \tag{3.11}$$

and by substituting the flow variable sensitivity $\partial U/\partial \alpha$ into equation 3.8,

$$\frac{dJ}{d\alpha} = -\frac{\partial J}{\partial U}\left(\frac{\partial R}{\partial U}\right)^{-1}\left[\frac{\partial R}{\partial X}\frac{\partial X}{\partial \alpha}\right] + \left[\frac{\partial J}{\partial X}\frac{\partial X}{\partial \alpha}\right] \tag{3.12}$$

In the above equation 3.12, term $-\frac{\partial J}{\partial U}\left(\frac{\partial R}{\partial U}\right)^{-1}$ represents the adjoint variable vector. Subsequently, the adjoint variable can be computed by resolving the adjoint system given by:

$$\left(\frac{\partial R}{\partial U}\right)^T \lambda = -\left(\frac{\partial J}{\partial U}\right)^T \tag{3.13}$$

which represents the discrete form of the adjoint equation. By substituting above equation 3.13 into equation 3.14 , the gradient of the objective function with respect to the design variables is given by:

$$\frac{dJ}{d\alpha} = \frac{\partial X}{\partial \alpha}\left[\frac{\partial J}{\partial X} + \lambda^T \frac{\partial R}{\partial X}\right] \tag{3.14}$$

It can be inferred from Equation 3.13 that as the geometric design variable does not explicitly appear in the equation, we only need to solve this equation for the number of objective functions of interest. Therefore, the computational cost of the adjoint method is independent of the number of design variables and proportional to the number of objective functions.

3.5. Interpretation of Adjoint Sensitivities

As this work is based on the implementation of the adjoint method to an isolated propeller configuration, it is crucial to state how the wealth of adjoint data generated from this research can be interpreted and used for the design purposes. In particular, an adjoint solution results in the following data-

- Surface Sensitivities- A surface sensitivity map indicates the regions of extreme sensitivity on the surface of the geometry in the study. The regions of high sensitivity on perturbation can have a dominant influence on the objective function of interest.
- Gradient Vector- The gradients provide a quantitative change in the objective function with respect to the perturbation of the design variables used to parameterize the geometry.

  This information provides physical insight into the design parameters that have a dominant effect on the objective function and can be used to drive the design process in order to achieve a gain in the performance of interest.
- Adjoint flowfield- Similar to the flowfield attained from a CFD solver that provides the solution of physical flow variables for a given boundary conditions, an adjoint flowfield provides adjoint counter part of those flow variables. The adjoint flow field ties the adjoint solution to the flow variables to gain a physical insight of how the variation in a physical flow variable due to design modification can lead to increment in the objective function [31].

4

Propeller Geometry and CFD Solver Setup

The current chapter presents the setup of the RANS CFD method used for the aerodynamic and performance analysis of the propellers along with a geometry of the propeller test cases. The propeller test cases used in this research are presented in Section 4.1. Two solvers have been used for the purpose of performing RANS based-CFD simulations of the propeller in isolated configuration- ANSYS Fluent and SU2. As aforemetioned, to validate SU2's Section 4.2 presents a discussion on the computational domain, setup of the two solvers as well as the mesh strategy used for the grid generation of the computational domains.

4.1. Propellers

To analyze the performance of the propeller, two propeller test cases have been analyzed in the current research namely – XPROP and Optimized XPROP.

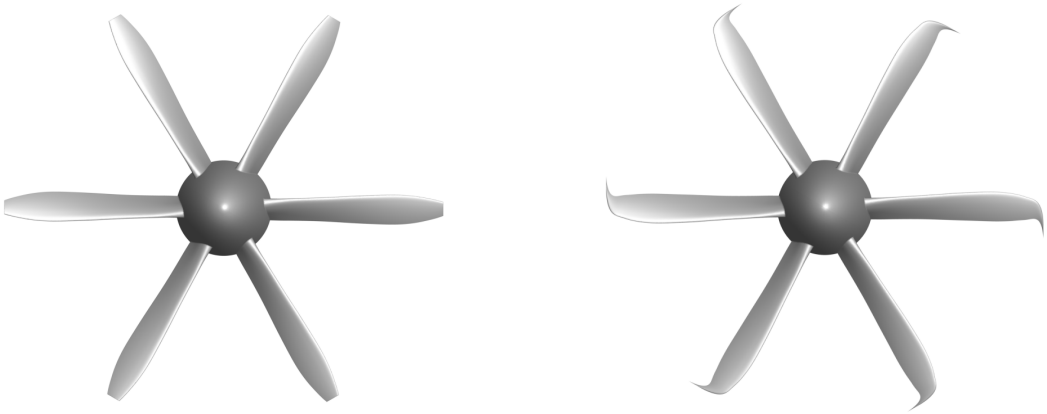

(a) XPROP **(b)** Optimized XPROP

Figure 4.1: Propeller test cases used in the research.

XPROP is a 6-bladed propeller used at Delft University of Technology. It has a blade radius of R_p=0.2032 m and lacks sweep. The computational simulations for XPROP have been performed at the blade pitch of $\beta_{0.7R_p} = 30°$.

Optimized XPROP is the second propeller test case that has been analyzed in the current research. As the name suggests, it is an optimized version of the baseline XPROP propeller blade that has been optimized for improved acoustic performance. The blade optimization was a result of the works of Wouter de Haan [18]. The optimization was performed using a low-fidelity blade element method wherein thrust-scaled acoustic pressure was the objective function to be minimized with a constraint on the propeller efficiency and thrust. The optimized XPROP differs from the Optimized XPROP sweep

distribution. Similar to the baseline XPROP blade, the computational simulations for the Optimized XPROP blade have been performed at the blade pitch of $\beta_{0.7R_p} = 30°$. It must be noted that both the propeller blades are operating at a blade pitch that is different from the design condition for cruise.

4.2. RANS-based CFD Setup

In the current research, the RANS-based CFD simulations have been performed using two solvers-

1. ANSYS Fluent 19.2, a commercial software.
2. SU2, an open-source collection of C++ based software tools used for performing PDE analysis and solving PDE-constrained optimization problems on general unstructured meshes.

The choice of the above-stated software solely depends on the availability and capabilities of the two. It is the open-source nature and the adjoint capabilities that made SU2 an attractive option to perform the computational flow and sensitivity analysis of the propeller. Although, SU2's computational analysis tools have been validated and verified comprehensively in Ref. [39], but for the sake of completeness SU2's RANS-based flow solver is verified against the available experimental data (only XPROP) and the results of similar simulations attained from ANSYS Fluent. Additionally, the reason to perform the CFD validation study of SU2 is motivated by the fact that since the primal flow solver's solution is used as an input by adjoint solver a design study, it is important to validate the flow results for the high accuracy of the gradients.

The current section presents a discussion on the generation of computational domain, setup of SU2's and ANSYS Fluent's solvers, and the grid generation of isolated propeller configurations.

4.2.1. Computational Domain

The computational domain defines the volume around the object under consideration (propeller blade, wing, etc.) where the discretized set of fluid flow equations are to be solved. The computational domain mimics the physical space around the object by defining the artificial boundaries where the physical values of the boundary conditions are specified. In the external aerodynamics such boundaries of the computational domain are namely inlet, outlet, farfield boundary, periodic boundary and symmetry. Enough care must be taken while constructing the computational domain such that the outer boundaries are sufficiently far away from the object under consideration in order to reduce the influence of the boundary conditions on the flow field near the object. Otherwise, the accuracy of the solution is impacted.

Based on the preceding best practices, the computational domain of the two propeller cases were constructed and are shown in Figure 4.2 for XPROP. Since same considerations have been used for both propellers, domain of only one propeller has been shown here for conciseness. Using the rotational periodicity boundary condition, the computational cost of the simulation was reduced by modelling a single blade in a 60° wedge domain. The rotational axis of the domain is parallel to the x-axis and the direction of the freestream flow is set to be in the positive x-direction. While, the direction of rotation is in the counter clockwise direction as shown in the Figure 4.2. The origin of the coordinate system i.e., (0,0,0) was defined at the nose of the spinner geometry. The dimensions of the outer boundaries of the domain were defined in terms of propeller radius and were chosen to be sufficiently far away from the propeller blade to minimize the effect on the flow properties near the propeller. Stokkermans [54] recommends having the farfield top boundary atleast five times the propeller radius from the propeller blade.

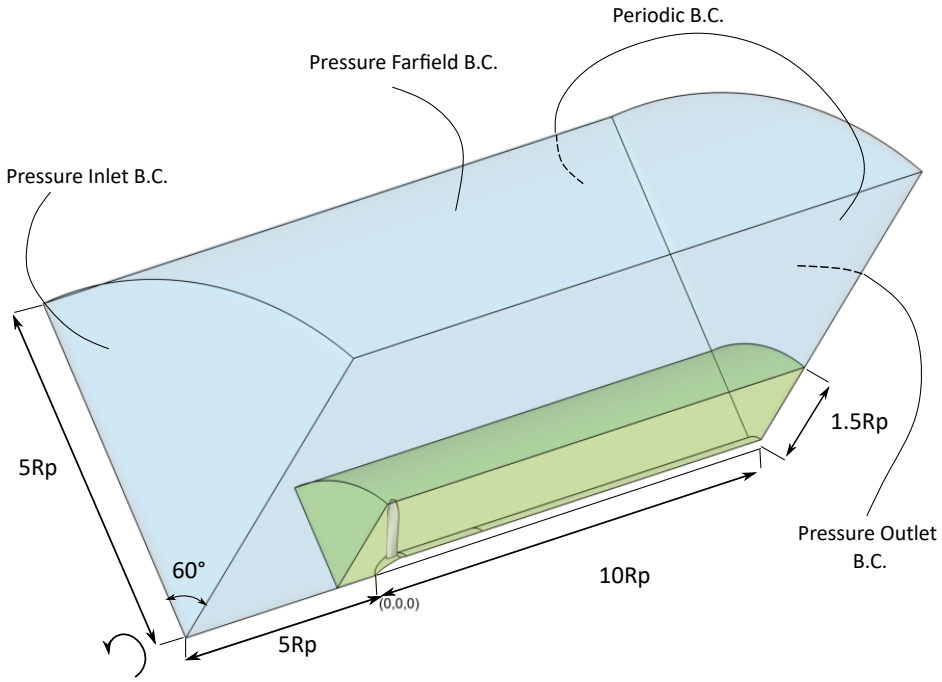

Figure 4.2: XPROP's computational domain with dimensions and boundary conditions

4.2.2. Solver Setup

The choice of the setting of the flow solver to perform the CFD simulations dictates the convergence, stability and accuracy of the simulation. This subsection presents a discussion on the setup of the flow solver of SU2 and ANSYS Fluent. First, a description physical problem of the simulation along with the turbulence model is presented. It is followed by a discussion on the definition of the freestream and boundary conditions. Finally, the numerical implementation of the solvers are presented.

Problem Description and Turbulence Modeling

In this study, the RANS equations are used to compute the flow simulation of an isolated propeller blade. The steady-state simulation is chosen to reduce the computational cost. As the unsteady or transient simulations are suitable to account for the unsteady phenomenon caused by the external influences such as non-asymmetric flow or induced effects due to the environment etc., which are negligible in the current case of isolated propeller.

A fully turbulent flow over the propeller blade is modelled using an appropriate turbulence model. Modelling a fully turbulent boundary layer reduces the computational cost in comparison to the transition model. Choice of turbulence model was based on the availability of the models, since SU2 offers two turbulence models – SA and k-ω SST. One equation S-A turbulence model has been implemented for modeling turbulence.

Free stream and Boundary Conditions

To perform the aerodynamic analysis of the isolated propeller configuration using a CFD solver accurately, it is essential to assign correct freestream values and boundary conditions to the solver. Based on the solver type, boundary conditions, and available freestream data, the user needs to compute additional required flow variables to set up the solver. Accurate inputs define the convergence and the stability of the flow simulation as they are used to initialize the solution. To perform the aerodynamic analysis of the propeller and compare the solvers, similar freestream values and boundary conditions are used that will be elaborated here along with relevant equations.

The ideal gas equation has been used as the equation of state for all the simulations performed in this research, which takes the form of –

$$T = \frac{p}{\rho \frac{R}{M_w}} \tag{4.1}$$

where T is the static temperature, p is static pressure, ρ is density, R is the universal gas constant and M_w is molecular weight. Using the above equation the static temperature is determined. The Mach number is determined using equation 4.2,

$$M_\infty = \frac{V_\infty}{a} = \frac{V_\infty}{\sqrt{\gamma RT}} \tag{4.2}$$

The dynamic viscosity is determined using Sutherland's law shown in equation 4.3,

$$\mu = \mu_{ref} \left(\frac{T}{T_{ref}} \right)^{3/2} \frac{T_{ref} + S}{T + S} \tag{4.3}$$

where μ is the dynamic viscosity, μ_{ref} is reference dynamic viscosity, T_{ref} is reference static temperature and S is Sutherland temperature. The total quantities are computed using the following equation 4.4 and 4.5.

$$p_t = p \left(1 + \frac{\gamma - 1}{2} M^2 \right)^{\frac{\gamma - 1}{\gamma}} \tag{4.4}$$

$$T_t = T \left(1 + \frac{\gamma - 1}{2} M^2 \right) \tag{4.5}$$

The inlet turbulence quantity for SA model, the eddy viscosity ratio is computed using recommndations of Spalart and Rumsey [52].

The boundary conditions used in the current research are highlighted in Figure 4.2. Similar boundary definitions have been specified for the case of Optimized XPROP. For the purpose of comparing the results of the two solvers in this research, similar boundary conditions have been used for the setup as shown in Table 4.1. The inlet of the domain has been specified as pressure inlet where total temperature and total pressure is assigned as an input. The total conditions are based on the freestream velocity V_∞=30 m/s. The total conditions are computed based on the static freestream that was used to perform XPROP's experiments. This is done to draw the comparisons of the RANS results with the experimental runs. At the domain outlet, pressure outlet condition has been specified where the static pressure and static temperature are prescribed. Riemann-invariant pressure farfield condition is specified at the top of the computational domain. For the pressure farfield condition, Mach number, static pressure, and static temperature are prescribed based on the freestream conditions. In contrary to ANSYS Fluent, no values are to be prescribed for farfield boundary condition in SU2 as the actual values are computed based on the other inputs by the user. The propeller, spinner and nacelle have been assigned as no-slip walls. It must be noted that SU2 offers, namely three options for no slip walls- constant heatlfux, convection, and isothermal. For this research, the option of constant heatflux is chosen to model the no-slip walls as they are assumed to be adiabatic walls. Finally, conformal periodic boundary condition is specified at the side walls of the domain by coupling the two side faces. For conformal periodic boundary condition, the two faces comprising of the periodic pair must have identical node distribution.

Table 4.1: Boundary Conditions for XPROP and Optimized XPROP with ANSYS Fluent and SU2.

Boundary Names	Boundary Conditions	
	ANSYS Fluent	SU2
Inlet	Pressure inlet	Pressure inlet
Outlet	Pressure outlet	Pressure outlet
Top	Pressure farfield	Pressure farfield
Propeller, Spinner, and Nacelle	No-slip walls	Constant heatflux (no-slip)
Periodic 1 & 2	Periodic	Periodic

Numerical Implementation of the Solvers

The numerical schemes used for solving the flow governing equations for ANSYS Fluent and SU2 are presented here.

ANSYS Fluent
ANSYS Fluent is a finite volume based CFD solver. ANSYS Fluent offers two types of solvers- pressure-based and density-based solvers. The two solvers differ in the method used to solve the continuity, momentum, and energy equations. In principle, pressure-based solvers have been traditionally used to solve incompressible to mildly compressible problems. While density-based solvers are suitable for high-Mach compressible flows. However, both the solvers have been reformulated to solve a broad range of flows [17]. In this research, a pressure-based solver is chosen. This decision is based on the fact that the tip Mach number for a range of advance ratios simulated in this research vary from incompressible to moderate Mach numbers. Moreover, better convergence is achieved with the pressure-based solver as compared to the density-based solver. The Coupled algorithm is used for solving pressure-based continuity equation and momentum equation. 2nd order upwind discretization scheme is chosen for solving the convection terms of the governing equations. By default, ANSYS Fluent uses 2nd order accuracy for the viscous terms. The Green-Gauss Node-based method is used for approximating the spatial gradients of the flow governing equations. The Courant number of 1 is used for all the simulations with ANSYS Fluent in this research.

SU2
Jameson-Schmidt-Turkel (JST) centered scheme is used for the discretization of the convective terms in flow governing equations. Discretization of the turbulence variable is done using 2nd order upwind scheme. The spatial gradienst of the flow variables are approximated using Green-Gauss method. CFL = 1 has been used for performing all the RANS simulations with SU2 in this research.

4.2.3. Grid Generation
In order to proceed with the CFD solution, the solver must be provided with a grid where the governing equations are to be discretized. This grid is generated by discretizing the computational domain/flowfield into discrete points and create a grid by connecting them using coordinate lines. The CFD solver further uses the generated grid to discretize the governing equations and compute the solution of the flow field. There are basically three types of grids-

1. Structured Grids – The structured grids are identified by the regular connectivity of the discrete points and each grid point is uniquely identified by the indices and Cartesian coordinates. The structured grid consists of quadrilateral in 2-D and hexahedra in 3-D.
2. Unstructured grids- The unstructured grids are identified by the irregular connectivity where the grid cells and points have no particular order. Due to the irregularity in ordering the grid points can not be identified by their indices. The unstructured grids consist of triangles in 2D and tetrahedra in 3D.
3. Hybrid Grids- The hybrid grids are a mix of structured and unstructured grids. The hybrid grid consists of hexahedra cells in the boundary layer region and tetrahedra cells in the rest of the flowfield, thus making it a hybrid or mixed grid. Due to large number of tetrahedra cells in the case of 3D mesh, it is often referred to as a type of unstructured mesh.

For selecting the type of grid generation, some of the differences between the structured and unstructured/hybrid grids can be highlighted below as mentioned by Blazek [6]-

- Unstructured grids offer higher flexibility in terms of the treatment of the complex geometries as compared to the structured grids.
- The unstructured grids have higher memory requirement to store the elements, nodes and connectivity table as compared to the structured grids.
- The solution dependent grid refinement and coarsening is easier in the case of unstructured grids as compared to the structured ones.
- Unstructured grids can handle complex flow problems in shorter turn around time with respect to the structured grids.

Based on the above differences hybrid grid, a type of unstructured grid, in the current research. The grids were generated using ANSYS Meshing software. The volume grid of the computational domain is discretized using tetrahedral elements while prism layers have been used in the region adjacent to the

walls. As mentioned in the foregoing description of the computational domain, the domain has been divided into the near field and far field domain for the purpose of meshing. Finer grid settings have been used in the near field domain with respect to the far field domain, to resolve the flow field near the propeller blade accurately. Figure 4.3a shows symmetry plane cut at z=0, depicting the volume domain around the XPROP's blade.

The surface grid of propeller blade, spinner, and nacelle have been discretized using triangular elements. For accurate resolution of the leading-edge curvature and trailing edges along the propeller blade, higher grid density is assigned around these regions as shown in Figure 4.3b. In addition to the element size of the surface grid, the growth rate as well as curvature normal angle is used to attain fine grid along the sharp edges.

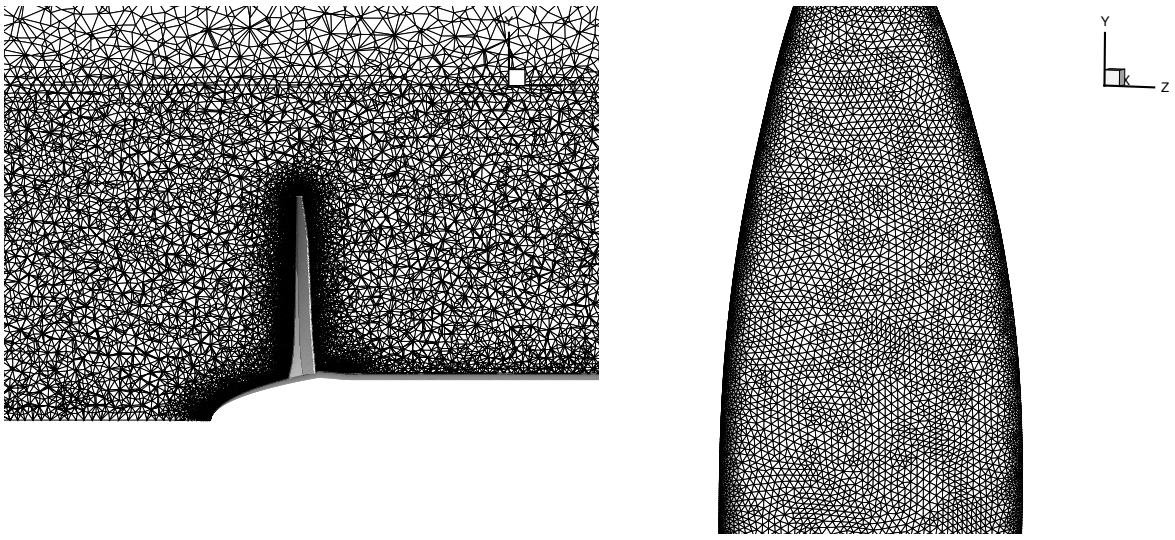

(a) XPROP's volume mesh sliced at z=0. **(b)** XPROP blade's surface mesh.

Figure 4.3: XPROP's Mesh domain.

Accurate resolution of the viscous region adjacent to the walls is essential for the computation of aerodynamic forces acting on the surfaces. The viscous region is resolved by using prismatic layers and the resolution of the prismatic layers is dictated by the thickness of the first layer and the growth rate. The thickness of the first layer is based on the non-dimensional normal distance to the wall, defined by y^+, which is defined as:

$$y^+ = \frac{\rho_\infty u_* y_{firstlayer}}{\mu} \tag{4.6}$$

where u_* is the friction velocity at the nearest wall, y is the distance of the first mesh layer to the nearest wall and μ is the dynamic viscosity of the fluid. In the current research, the first layer thickness is chosen such that, $y^+ \approx 1$ at the 70% of the propeller blade radius for the lowest advance ratio at which the simulation is performed. Since highest velocities are experienced at the low advance ratios leading to thinner boundary layer thickness, the thickness of the first layer is chosen with respect to the boundary layer thickness attained at low advance ratios. As for the requirement of the turbulence model, the viscous region must be resolved to have $y^+ \leq 1$.

The velocity at 70% propeller radius is determined using equation 4.7. This velocity computation is the resultant of the free stream velocity and the angular velocity at 70% propeller radius, while ignoring the induced velocities.

$$V_{rel} = \sqrt{(V_\infty)^2 + (\omega r)^2} \tag{4.7}$$

After determining the velocity at the 70% blade radius, the Reynolds number based on the chord of the section is estimated using 4.7

$$Re = \frac{\rho_\infty V_{rel} l_{chord}}{\mu} \tag{4.8}$$

Where, μ is computed using the Sutherland's law based on equation 4.3. The skin friction coefficient and wall shear stress can be computed using equations 4.9 and 4.10 respectively, as obtained from Schlichting [48].

$$C_f = [2log_{10}(Re) - 0.65]^{-2.3} \tag{4.9}$$

$$\tau_w = \frac{C_f}{0.5\rho V_{rel}^2} \tag{4.10}$$

Further, the friction velocity u_* is determined using equation 4.11.

$$u_* = \sqrt{\frac{\tau_w}{\rho}} \tag{4.11}$$

Finally, the thickness of first layer is determined by rearranging the equation 4.6.

$$y_{firstlayer} = \frac{y^+ \mu}{\rho u_*} \tag{4.12}$$

Figure 4.4 displays the slice at 70% radius, to show the inflation layers along the wall of the propeller blade.

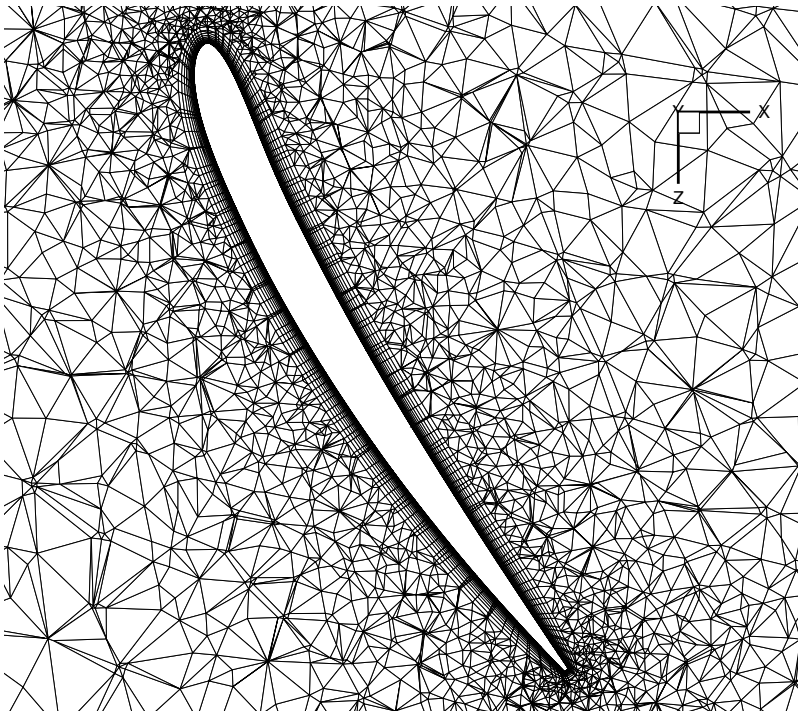

Figure 4.4: XPROP's volume mesh with slice at r/Rp=70%

In the present research, grid dependency studies have been performed for the two propeller cases. It is performed by generating a set of grids varying in fineness of the grid and performing simulations on them. Therefore, a set of grids are generated by gradually refining the grid density of the whole computational domain. Grid density is controlled by varying the volume refinement of the domain, surface refinement of the no-slip walls, the first layer thickness of the inflation layers, and growth rates of the surface grid. The number of inflation layers was kept constant while performing the grid refinement. Furthermore, these grids are used to estimate the discretization uncertainty using the least squares version of grid convergence index (GCI) as proposed by Eça and Hoekstra [11].

Estimation of Discretization Uncertainty using GCI

According to Eça and Hoekstra, three sources contribute towards the numerical error of a CFD simulation, namely- round-off error, iterative error, and discretization error [11]. Among these three errors, the contribution by spatial discretization error is dominant. Discretization error is a consequence of the transformation of governing equations meant for continuum domain into discrete algebraic equations. The Grid convergence index (GCI) proposed by Roache is one of the most used methods to estimate the resulting spatial discretization error. In this work, the least squares version of Roache's GCI method is implemented to estimate the discretization uncertainty, which is briefly presented here.

The discretization uncertainty of flow quantity or a solution U over a chosen grid is estimated using equation 4.13

$$U = F_s|\delta_{RE}| \tag{4.13}$$

where F_s is safety factor and δ_{RE} is the error estimation.

Richardson's extrapolation can be used to obtain the error estimation, as shown in Equation 4.14 [11].

$$\delta_{RE} = \phi_i - \phi_0 = \alpha h_i^p \tag{4.14}$$

Where ϕ_i is the value of the flow quantity on a given grid i, ϕ_0 is the estimated exact solution, h_i is average cell size of the grid i, and p is the order of convergence. The relative cell size of a grid is computed using the ratio of the finest grid and the grid i as shown in Equation 4.15.

$$\frac{h_i}{h_{fine}} = \frac{N_{cells_i}}{N_{cells_{fine}}}^{\frac{-1}{3}} \tag{4.15}$$

As will be discussed in the next chapter, five grids have been used for performing grid dependency study. Richardson extrapolation of the flow solutions ϕ_i on the five grids is performed using the least-squares method. Using the solutions on the five grids, least squares method is used to compute ϕ_0, h_i, and p by minimizing the function shown in Equation 4.16.

$$U_s = \sqrt{\sum_{i=1}^{n_g}(\phi_i - (\phi_0 + \alpha h_i^p))^2} \tag{4.16}$$

Where n_g is the number of grids used in the study to compute the required variables. The minimisation of the above function is performed using MATLAB's minimization function fmincon. The standard deviation of the fit is determined using Equation 4.17.

$$U_s = \sqrt{\frac{\sum_{i=1}^{n_g}(\phi_i - (\phi_0 + \alpha h_i^p))^2}{n_g - 3}} \tag{4.17}$$

Once the required parameters are determined, the resulting discretization error U_ϕ is computed using Equation 4.18 based on the value of observed order of accuracy, p. For the cases where monotonic convergence is not observed, the uncertainty estimation is based on the Δ_M. It represents the maximum difference between the computed solutions as shown in Equation 4.19.

$$U_\phi = \begin{cases} 1.25\delta_{RE} + U_s & \text{for} \quad 0.95 \leq p < 2.05 \\ \min\left(1.25\delta_{RE} + U_s, 1.25\Delta_m\right) & \text{for} \quad 0 < p < 0.95 \\ \max\left(1.25\delta^*_{RE} + U^*_s, 1.25\Delta_m\right) & \text{for} \quad 2.05 \geq p \\ 3\Delta_m \end{cases} \tag{4.18}$$

$$\Delta_m = \max(|\phi_i - \phi_j|) \quad \text{with} \quad 1 \leq i \leq n_g \wedge 1 \leq j \leq n_g \tag{4.19}$$

Where, the parameters with a superscript * represent the parameters based on a least-squares fit with theoretical order of convergence where $p = 2$.

5

Aerodynamic and Performance Analysis

This chapter presents the results obtained from RANS-based CFD simulations of the two isolated propeller configurations. These results from the aerodynamic analysis are used to draw a comparison between SU2 and ANSYS Fluent's flow solvers, as discussed in Section 5.1. While Section 5.2 presents the results and discussion comparing the aerodynamic performance of XPROP and Optimized XPROP for a range of advance ratios.

5.1. Flow Solver Comparison

This section presents a comparison between the performance of the SU2 and ANSYS Fluent's flow solvers based on the results obtained from the aerodynamic analysis of XPROP and Optimized XPROP. SU2's results have been compared against that of ANSYS Fluent's, based on the grid convergence, discretization uncertainty, performance parameters, and pressure distributions of the blade simulations. For all the simulations presented in this section, freestream values shown in Table 5.1 are used.

Table 5.1: Freestream operating conditions.

Variable	Value
V_∞	30 m/s
p	101742 Pa
ρ	1.176 kg/m^3
T	301.4 K

The aerodynamic analysis of the propeller blades has been performed for a range of advance ratios ranging from 0.6-1.2. In this study, the advance ratio is varied by changing the rotational speed of the propeller while keeping the freestream velocity constant, i.e., V_∞=30 m/s. The operating points of the propeller are shown in Table 5.2

Table 5.2: Operating points for the CFD simulations of propellers with $\beta_{0.7R} = 30°$.

J	V_∞ [m/s]	n[s^{-1}]	$Re_{0.7R_p}$	M_{tip}
0.6	30	123.03	225073.66	0.46
0.7	30	105.46	195318.68	0.40
0.8	30	92.27	173293.73	0.35
0.9	30	82.02	156411.59	0.31
1	30	73.82	143119.40	0.28
1.1	30	67.11	132428.70	0.26
1.2	30	61.52	123680.38	0.24

5.1.1. Grid Convergence and Discretization Error Estimation

When performing CFD simulations, it is essential to choose a grid that is fine enough to estimate results close to the exact solution. Even though it is known that finer mesh would generate a more accurate result but, it comes at the expense of higher computational resources and time. A grid dependency study is performed to choose a grid that would generate an accurate solution and is optimal to perform simulations. It is a method to ensure that the results are the consequence of the flow physics and boundary conditions but not affected by the spatial resolution. The grid dependency study and estimation of discretization error for XPROP and Optimized XPROP is presented here.

XPROP

As aforementioned in the preceding chapter, five grids were constructed for performing a grid dependency study and quantifying discretization error. Table 5.3 presents the grid size and refinement ratio h_i/h_5 for each of the five grids of XPROP's isolated propeller configuration, where Mesh 1 is the coarsest and Mesh 5 being finest mesh.

Table 5.3: Mesh sizes of XPROP's domain.

Mesh	Number of cells	h_i/h_5
Mesh 1	1518725	1.54
Mesh 2	2229029	1.36
Mesh 3	2832304	1.26
Mesh 4	4018643	1.12
Mesh 5	5613054	1

For grid dependency study and estimation of the discretization error, CFD simulations have been performed at an advance ratio of J=1.0. The motivation for choosing J=1.0 as the condition to perform initial calculations for grid dependency study is based on the fact that in the experimental runs of XPROP, the highest efficiency was attained for the advance ratios closer to J=1.0. This can be seen in the performance plots from XPROP's experimental run discussed in Subsection 5.1.2. The variation in the thrust coefficient C_T and power coefficient C_P obtained using SU2 and ANSYS Fluent as a function of mesh refinement of XPROP's domain are shown in Figure 5.1a and 5.1b respectively. The variation of the thrust and power coefficient is shown with respect to the value attained at the Mesh 1 i.e., coarsest mesh. The thrust and power coefficients presented in this research are the contribution from the propeller blade and spinner.

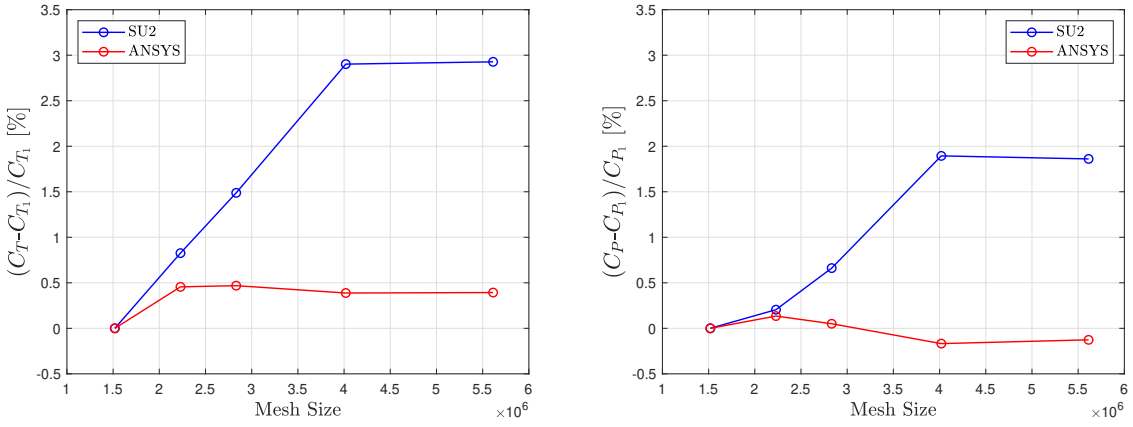

(a) Grid convergence for Thrust Coefficient (C_T). **(b)** Grid convergence for Power Coefficient (C_P).

Figure 5.1: Grid Convergence of XPROP mesh with SU2 and ANSYS Fluent.

A convergent behaviour is observed for the C_T obtained from both the solvers as seen in Figure 5.1a. The difference between the two solvers lies in the sensitivity of the C_T to the mesh refinement. For every mesh refinement beyond Mesh 2, the deviation in thrust coefficient C_T is minimal with the

ANSYS Fluent. The variation of the ANSYS Fluent's solution from Mesh 1 to 5 is 0.4%. Whereas, variation in SU2's solution from Mesh 1 to Mesh 5 is 2.93%. Thus, SU2's solutions are relatively more sensitive to the mesh refinement as a higher deviation in thrust coefficient C_T is observed on refining the same grids as compared to that with ANSYS Fluent. Beyond Mesh 4, C_T from SU2 results in a change of 0.3%. While, C_T from ANSYS Fluent results in a change of 0.1% on refining Mesh 4. This deviation on mesh refinement is within an acceptable tolerance.

The variation of power coefficient C_P with grid refinement is shown in Figure 5.1b. It can be observed that the solution from the two solvers converges. Although, the convergence behaviour of the solutions from the two solvers differs, as the difference between the solutions from ANSYS Fluent tends to change the sign on refinement. Thus, the convergence observed for ANSYS Fluent is not monotone as explained by Philips and Roy [41]. In comparison to the C_T, the solutions of C_P with SU2 are less sensitive to mesh refinement as lower differences are attained. For both the solvers, power coefficient C_P deviates negligibly on refining Mesh 4 indicating a converged solution. On refining Mesh 4, the C_P obtained at Mesh 5 results in a deviation of 0.04% and 0.03% for ANSYS Fluent and SU2, respectively.

Based on the inferences made from the grid convergence study, Mesh 4 was chosen for further computations for XPROP's isolated propeller configuration. Error analysis was performed for C_T andpower coefficient C_P of XPROP using the least-squares version of the GCI method. Table 5.4 shows the quantities computed for the estimation of discretization error with SU2 and ANSYS Fluent for both the performance parameters. It presents the observed order of accuracy, the standard deviation of fits, error estimation and the estimated discretization error for Mesh 4.

Table 5.4: Grid dependency study of XPROP.

Boundary Names	Thrust coefficient C_T		Power coefficient C_P	
	ANSYS Fluent	SU2	ANSYS Fluent	SU2
p	-	1.09	-	-
$U_s(\%)$	-	0.39	-	-
$\delta_{RE}(\%)$	-	5.23	-	-
p^*	2	2	2	2
$\lvert U_\phi \rvert(\%)$	0.31	6.85	0.38	5.58

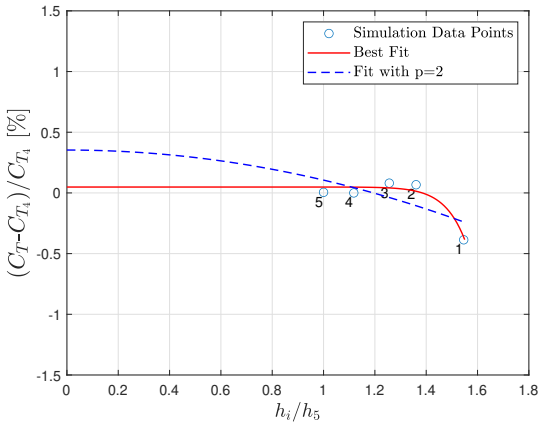

(a) Grid convergence of XPROP with ANSYS Fluent for Thrust Coefficient (C_T).

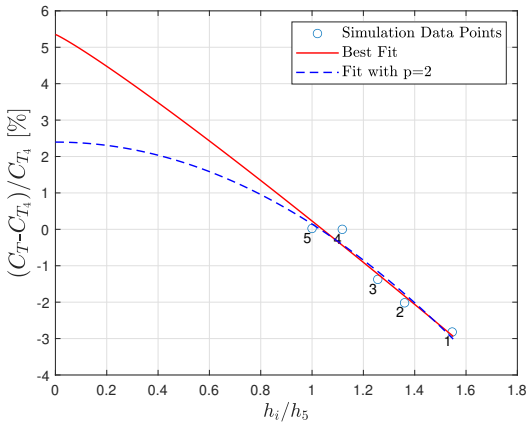

(b) Grid convergence of XPROP with SU2 Thrust Coefficient (C_T).

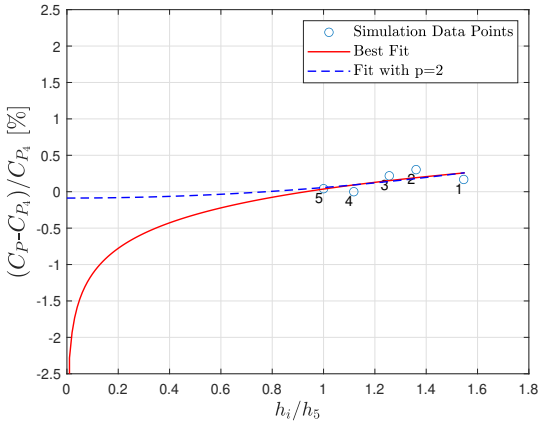

(c) Grid convergence of XPROP with ANSYS Fluent for Power Coefficient (C_P).

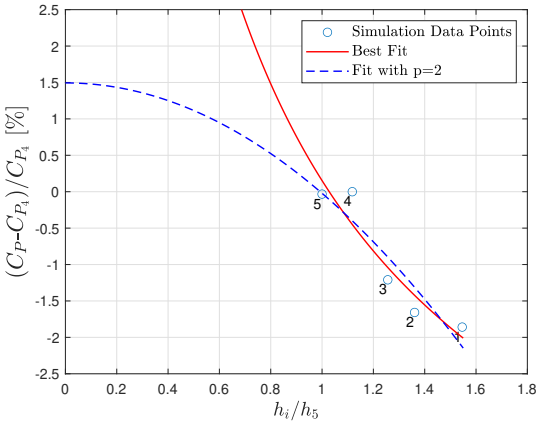

(d) Grid convergence of XPROP with SU2 for Power Coefficient (C_P).

Figure 5.2: Grid convergence plots of XPROP using least squares method of GCI.

For C_T calculations with ANSYS Fluent, a converging behaviour is observed with the observed order of accuracy of 17.96. Such high order of observed accuracy could be a consequence of the scatter in the data, potentially due to Mesh 1 as seen in Figure 5.2a. This results in the use of theoretical order of accuracy for estimating the discretization error. As inferred from from the table, the discretization error is estimated to be 0.31% for C_T computed with the ANSYS Fluent. Whereas, a monotonic converging is observed for the thrust coefficient C_T with SU2 as seen in Figure 5.2b. On using the observed order of accuracy of p =1.09 to compute the discretization error, a high numerical uncertainty of 6.85% is achieved. It is interesting to see that even though the convergence behaviour of C_T with SU2 in Figure 5.1 depicts Mesh 4 to be converged with respect to Mesh 5, but based on the GCI results high discretization error is observed with the best fit curve.

Solutions of C_P with ANSYS Fluent results in a best fit curve to be diverging. This could be attributed to the differences between the solutions being small and, therefore adding scatter to the data as shown in Figure 5.2c. The theoretical order of accuracy is used for estimating the discretization error which is estimated to be 0.38%. Similar to the ANSYS Fluent, SU2's best fit for solution of C_P is observed to be diverging. Moreover, oscillatory convergence is observed for SU2's data. For C_P, convergence was found to have a discretization error of 5.58%.

Optimized XPROP

Similar to the case of XPROP, five grids were constructed for Optimized XPROP case to perform a grid dependency study and estimation of discretization error. Table 5.5 presents the grid size and refinement ratio h_i/h_5 for each of the five grids of Optimized XPROP's isolated propeller configuration.

Table 5.5: Mesh sizes of Optimized XPROP's domain.

Mesh	Number of cells	h_i/h_5
Mesh 1	1646243	1.54
Mesh 2	2391334	1.36
Mesh 3	3056077	1.26
Mesh 4	4259850	1.12
Mesh 5	6056295	1

The variation in thrust coefficient C_T and power coefficient C_P obtained using SU2 and ANSYS Fluent as a function of grid refinement of Optimized XPROP's domain are shown in Figure 5.3a and 5.3b, respectively. Similar to XPROP, case the variation of the performance is shown with respect to the value attained at the Mesh 1 i.e., coarsest mesh.

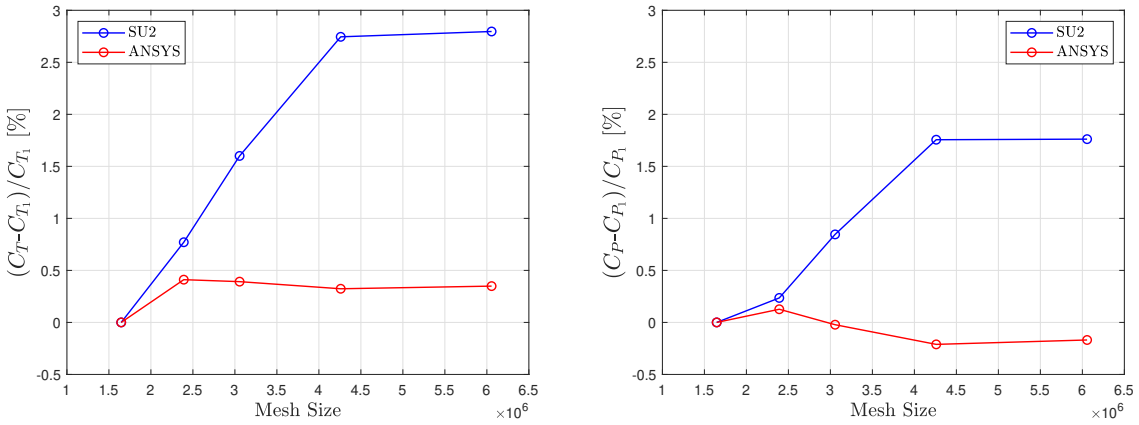

(a) Grid convergence of Optimized XPROP with SU2 and ANSYS Fluent for Thrust Coefficient (C_T).

(b) Grid convergence of Optimized XPROP with SU2 and ANSYS Fluent for Power Coefficient (C_P).

Figure 5.3: Grid Convergence of Optimized XPROP mesh with SU2 and ANSYS Fluent.

From Figure 5.3a, converging behaviour of thrust coefficient is observed for both the solvers. A larger relative difference in the thrust coefficient C_T is attained for the SU2's solutions as compared to that of the ANSYS Fluent on grid refinement. The variation of the ANSYS Fluent's solution from Mesh 1 to Mesh 5 is 0.35%. Whereas, variation in SU2's solution from Mesh 1 to Mesh 5 is 2.79%. For the case of ANSYS Fluent, there is negligible change in the C_T on refining the mesh beyond Mesh 2 and therefore the mesh seems to be converged quickly at Mesh 2 itself. While a significant difference in the value of thrust coefficient is seen on refining up to Mesh 4 for SU2. On refining Mesh 4, the C_T obtained at Mesh 5 results in a deviation of 0.02% and 0.05% for ANSYS Fluent and SU2, respectively.

From Figure5.3b, it can be inferred that the difference in the solutions of power coefficient C_P on successive refinements is lower for ANSYS Fluent as compared to SU2. As seen for XPROP's case, ANSYS Fluent's convergence behaviour is less uniform as compared to SU2's solutions and is termed as non-monotone. In comparison to the C_T, the solutions of C_P with SU2 are less sensitive to mesh refinement as lower differences are attained. For both solvers, negligible differences are attained on refining Mesh 4, indicating a converged solution. On refining Mesh 4, the C_P obtained at Mesh 5 results in a deviation of 0.04% and 0.005% for ANSYS Fluent and SU2, respectively.

Mesh 4 was chosen for performing further computations for Optimized XPROP's isolated propeller configuration. The error analysis was performed for C_T and C_P for Optimized XPROP using the least-squares version of the GCI method. Table 5.6 shows the quantities computed for the estimation of discretization error with SU2 and ANSYS Fluent for both the performance parameters. It presents the observed order of accuracy, the standard deviation of fits, error estimation and the estimated discretization error for Mesh 4.

High order of observed accuracy was attained for the grid convergence of Optimized XPROP's thrust coefficient C_T using ANSYS Fluent. This can be attributed to the solutions from different grid being

Table 5.6: Grid dependency study of Optimized XPROP.

Boundary Names	Thrust coefficient C_T		Power coefficient C_P	
	ANSYS Fluent	SU2	ANSYS Fluent	SU2
p	-	1.67	-	-
$U_s(\%)$	-	0.72	-	-
$\delta_{RE}(\%)$	-	3.0	-	-
p^*	2	2	2	2
$\lvert U_\phi \rvert(\%)$	0.40	3.9	0.42	11.78

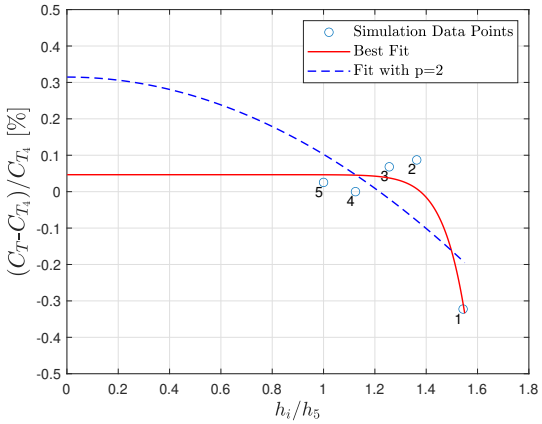

(a) Grid convergence of Optimized XPROP with SU2 and ANSYS Fluent for Thrust Coefficient (C_T).

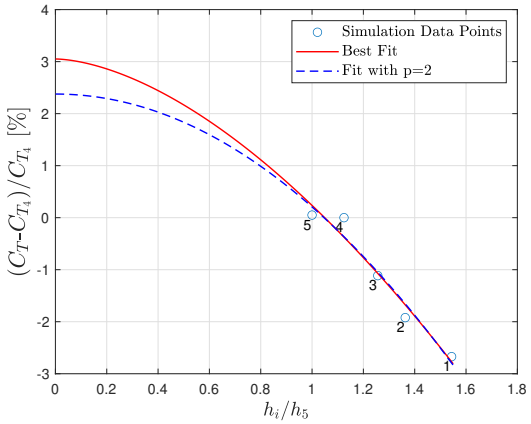

(b) Grid convergence of Optimized XPROP with SU2 and ANSYS Fluent for Power Coefficient (C_P).

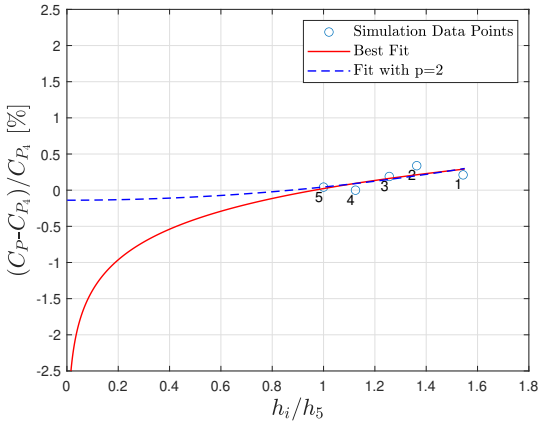

(c) Grid convergence of Optimized XPROP with SU2 and ANSYS Fluent for Thrust Coefficient (C_T).

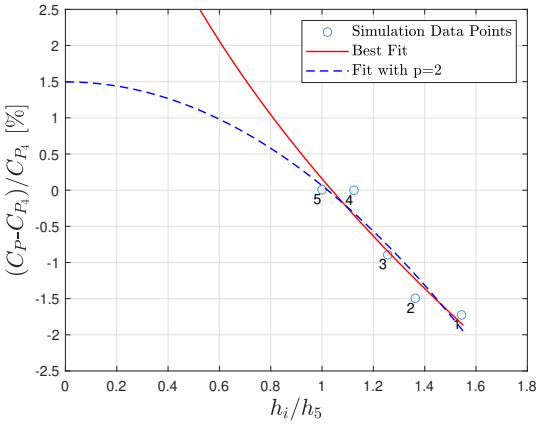

(d) Grid convergence of Optimized XPROP with SU2 and ANSYS Fluent for Power Coefficient (C_P).

Figure 5.4: Grid convergence plots of Optimized XPROP using least squares method of GCI.

very close to each other, thus introducing scatter in the data [53]. The theoretical order of accuracy is used to estimate the discretization error for C_T which is 0.4%. Whereas, monotonic convergence is observed for the thrust coefficient with SU2. This results in a best fit with a observed order of accuracy 3.9%. Therefore, a good fit is achieved as shown in Figure 5.4b. However, in comparison to ANSYS Fluent, a higher discretization error is estimated.

From Figure 5.4c, a diverging behaviour is observed for the best fit of solutions of power coefficient C_P with ANSYS Fluent. Similar to C_T, the solutions for C_P are very close to each other for a large variation in the grid sizes, thus introducing scatter in the data. A discretization error of 0.42% is estimated with the theoretical order of accuracy. Similar to the ANSYS Fluent, SU2's solution of power

coefficient C_P results in a diverging fit. A large discretization error of 11.78% is achieved for SU2.

5.1.2. Performance Parameters

The curves of performance parameters of the two propeller test cases are compared and discussed in the following paragraphs. The aerodynamic analysis of the propeller blades has been performed for a range of advance ratios ranging from 0.6-1.2. In this study, the advance ratio is varied by changing the rotational speed of the propeller while keeping the freestream velocity constant, i.e., V_∞=30.

XPROP

Figure 5.5 and 5.6 depicts the trends of thrust coefficient and power coefficient over a range of advance ratios. The C_T and C_P curves obtained from the RANS simulations using SU2 and ANSYS Fluent have been compared against the experimental data. The curves for the experimental data have been plotted by fitting the available data points using 2nd order polynomial fitting.

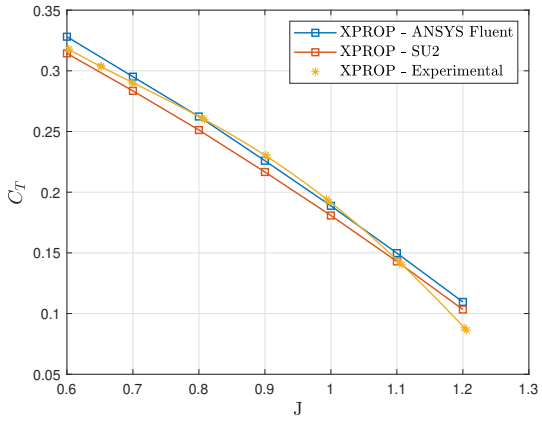

Figure 5.5: Comparison of XPROP's Thrust Coefficient (C_T) trends obtained using flow solvers with experimental data.

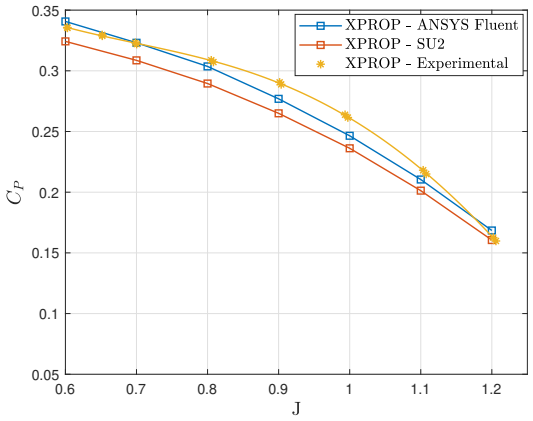

Figure 5.6: Comparison of XPROP's Power coefficient (C_P) trends obtained using flow solvers with experimental data.

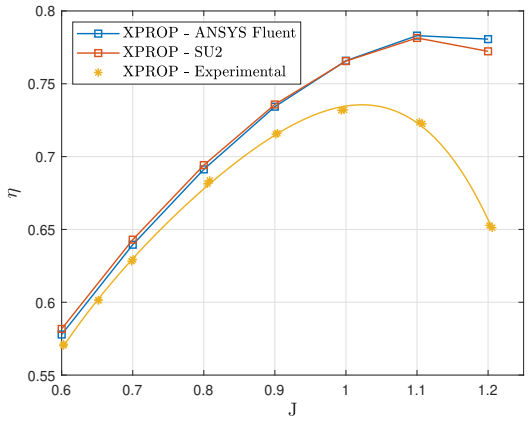

Figure 5.7: Comparison of XPROP's Efficiency (η) trends obtained using flow solvers with experimental data.

The thrust coefficient C_T curve predicted by ANSYS Fluent has a linear variation with respect to the advance ratio. Whereas, the experimental curve tends to be less linear. ANSYS Fluent overpredicts the thrust coefficient at low and high advance ratios with respect to the experimental curve. Relatively, lower differences between the experimental and ANSYS Fluent's computed values at moderate advance ratios. Whereas in the case of power coefficient C_P curves, ANSYS Fluent tends to underpredict C_P

values for a large range of advance ratios with respect to experimental data. It overpredicts the C_P values at low advance ratios and high advance ratios. Based on the difference between the computed and experimental values, ANSYS Fluent's thrust curves exhibit better agreement with the experimental data for a large part of the operating range in comparison with the power curves.

On comparing values from SU2 with experimental data, it can be inferred that SU2 underpredicts the thrust coefficient C_T values for the whole range of the advance ratios except for advance ratios beyond J=1.1. At J=1.1, the experimental thrust curve crosses that of SU2's, beyond which SU2's computations result in a higher thrust coefficient C_T. A similar trend is seen for the power coefficient C_P curves, as SU2 underpredicts the C_P values for the almost whole range of computed advance ratios except at the advance ratio close to J=1.2 where it meets experimental the C_P curve. In comparison to the C_T curve, it can be seen that larger differences are obtained between SU2's computed and experimental values for the C_P curve.

On comparing the thrust and power curves of SU2 and ANSYS Fluent, results from both solvers exhibit similar curves with increasing advance ratios. However, SU2 predicts lower C_T and the C_P values than ANSYS Fluent for the whole range of advance ratios. Additionally, a trend of decreasing differences between the computed values of SU2 and ANSYS Fluent with increasing advance ratio is seen for both C_T and the C_P curves.

On observing the trends, the discrepancies between the numerical calculations and the experimental results can be the result of the differences in the blade pitch angle of the simulated blades and experimental blade. This difference in the blade pitch angle arises due to the change zero-lift angle of attack at high advance ratios, where the Reynolds number is low. As can be seen from Table 5.2, the Reynolds number with respect to 70% radius is lower than $1.5*10^5$ for J >0.9. At such high advance ratios (on varying the RPM), the viscous effects become important and the performance of the propeller is sensitive to the Reynolds number for $Re < 1.5*10^5$ [49]. Additionally, the CFD simulations have been performed with fully turbulent flow over the blade section, while this might not be the case for the experimental runs.

Whereas, the results from ANSYS Fluent and SU2 display a similar trend but the offset in the values could be the result of the difference in the numerical schemes used by the two solvers. Further investigation is performed in Subsection 5.1.3, drawing the comparisons between the pressure distributions from the two solvers to gain an insight into the reason behind such discrepancies at a given condition. Although the differences exist, the results from SU2 are deemed to be satisfactory for further computations.

Optimized XPROP

Figure 5.8 and 5.9 depicts the trends of thrust coefficient C_T and power coefficient C_P over a range of advance ratios for Optimized XPROP. Much similar to the case of XPROP, the ANSYS Fluent predicts higher value of C_T as compared to SU2 throughout the range of computed advance ratios. Similar inference can be made from the C_P curves, where ANSYS Fluent predicts higher values for simulation for any given advance ratios. The trend of the curves from both the solvers are same for the thrust and power. However, C_T curve exhibits a linear relation to advance ratio, while C_P displays a more curvy relation. Similar to the XPROP's trends, a decrease in offset is seen for the C_T and C_P curves with increasing advance ratios.

Based on the inferences from thrust and power curves, the effect tends to cancel out and there is a marginal difference in the efficiency curve for the two solvers upto J=1.0, as displayed in Figure 5.10. Although, SU2 tends to predict higher efficiency upto J=0.9. Beyond this point, the ANSYS Fluent tends to predict higher efficiencies at higher advance ratios. Highest efficiency for both the solvers is attained at the advance ratio of J=1.1, before peaking down at J=1.2.

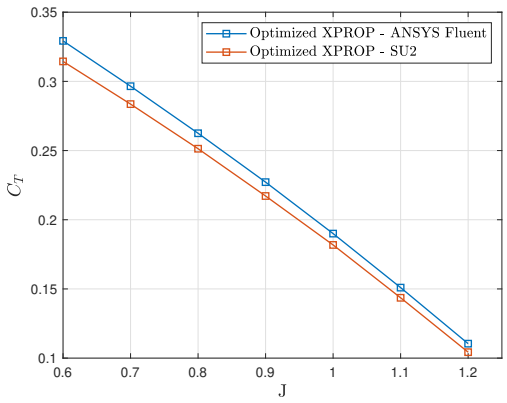

Figure 5.8: Comparison of Optimized XPROP's Thrust Coefficient (C_T) trends obtained with SU2 and ANSYS Fluent.

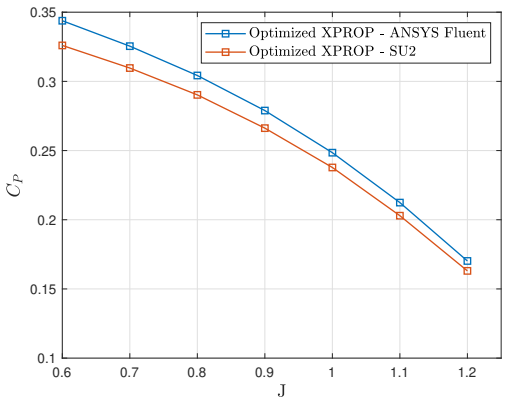

Figure 5.9: Comparison of Optimized XPROP's Power coefficient (C_P) trends obtained with SU2 and ANSYS Fluent.

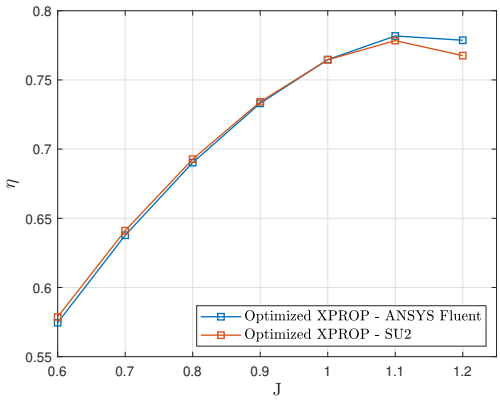

Figure 5.10: Comparison of Optimized XPROP's Efficiency (η) trends obtained with SU2 and ANSYS Fluent.

A comparison of aerodynamic performance of XPROP and Optimized XPROP propellers will be presented later in Section 5.2.

5.1.3. Pressure Distribution

This subsection presents a comparison between the pressure distributions obtained with ANSYS Fluent and SU2 at various radial positions along the XPROP and Optimized XPROP propeller at J=1.0. In this reaerch, pressure coefficient C_p is defined based on the freestream velocity and rotational velocity at a considered radial section, as show in equation 5.1

$$C_p = \frac{P - P_\infty}{\frac{1}{2}\rho_\infty[V_\infty^2 + (\omega.r)^2]} \tag{5.1}$$

XPROP

Figure 5.11 shows the pressure distributions from ANSYS Fluent and SU2 at radial locations- 25%, 40%, 60%, 80% and 95%.

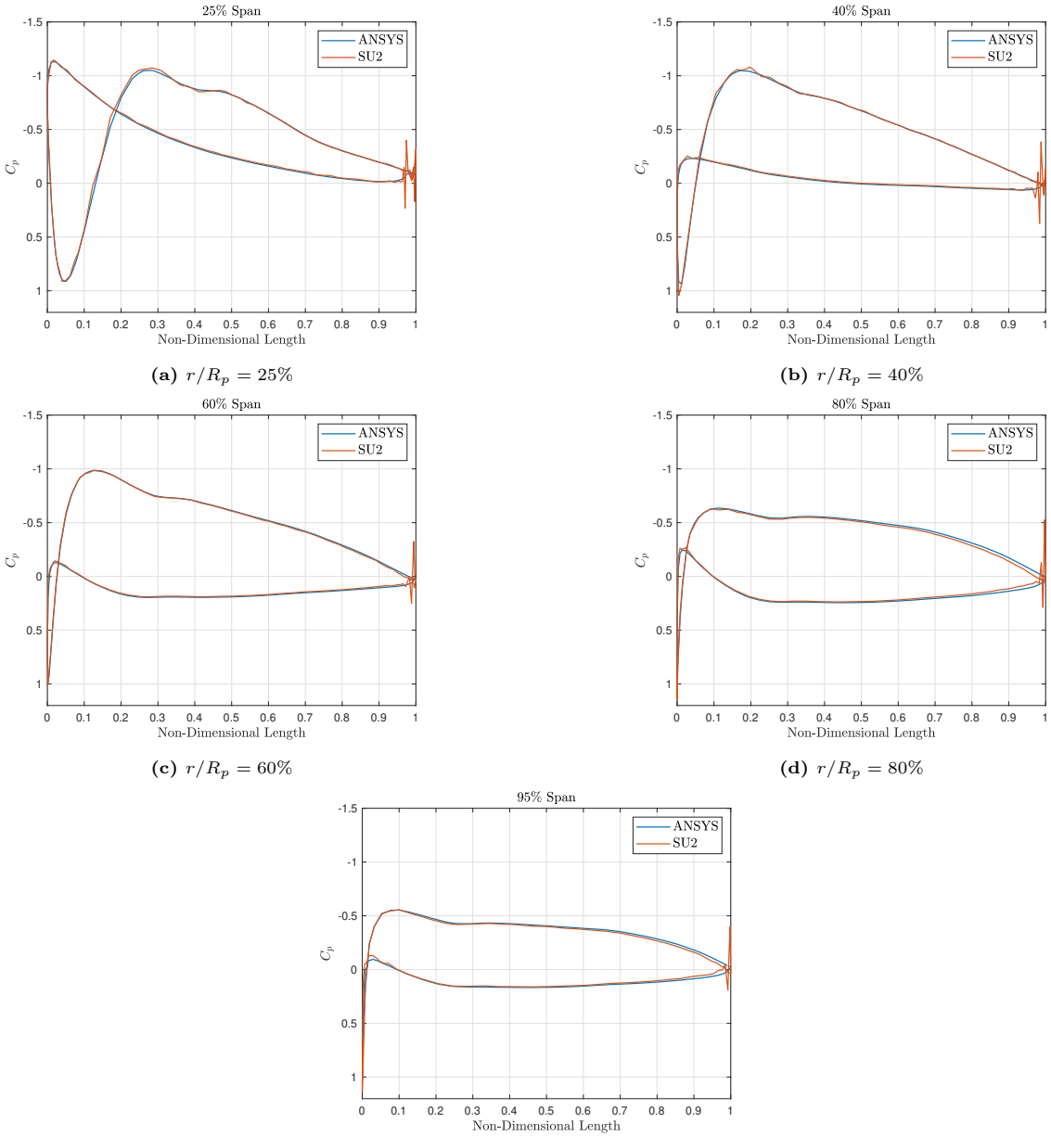

(a) $r/R_p = 25\%$

(b) $r/R_p = 40\%$

(c) $r/R_p = 60\%$

(d) $r/R_p = 80\%$

(e) $r/R_p = 95\%$

Figure 5.11: Pressure distribution at different radial spans of XPROP at J=1.0 from ANSYS Fluent and SU2.

On comparing the surface pressure distributions from the two solvers, a reasonable agreement is seen

for the pressure distributions at 25%, 40%, and 60% radius for most of the surface, except the trailing edge. In contrast to ANSYS Fluent, SU2 predicts spikes along the trailing edge of the blade section.

At 80% radius, a difference in the pressure distribution near the trailing edge can be noticed as SU2 predicts lower C_p values on the suction side as well as the pressure side as compared to ANSYS Fluent. A similar trend is seen for the pressure distribution along the trailing edge of the blade section at the 95% radius. As seen in the inboard sections, SU2's predicts the spikes at the trailing edge of the blade sections at outboard radial positions as well. Similar discrepancies along the trailing edge were observed in the works of Dhert [9] and Economon et al. [13]. Economon et al. related such spikes to be the result of the presence of a sharp trailing edge. Moreover, SU2 predicts C_p greater than 1 at the stagnation point at 80% and 95% span, for a tip Mach number of 0.28, i.e., incompressible flow.

Based on the above observations, it can be inferred that SU2 and ANSYS Fluent predict similar pressure distribution for large part of the blade sections, except the discrepancies at the trailing edges of all the blade sections with SU2. Additionally, the SU2 predicts higher value of C_p at the stagnation point. Such differences in the pressure distributions could lead to integrated loads and flowfield, different from that obtained with ANSYS Fluent. This can also explain the offset in the performance parameter curves of the two solvers, as discussed in the preceding Subsection 5.1.2.

Optimized XPROP

Figure 5.12 shows the pressure distributions from ANSYS Fluent and SU2 at radial locations- 25%, 40%, 60%, 80% and 95%, of Optimized XPROP's blade.

On observing the pressure distributions from two solvers, similar inferences are made as were highlighted in the case of XPROP's blade. Except the trailing edge, identical pressure distributions are seen on large part of pressure and suction side at 25%, 40%, and 60% radius for the two solvers. Similar to XPROP, SU2 predicts spikes at the trailing edges of the blade sections at all the radial positions along Optimized XPROP's blade. SU2 predicts value of C_p greater than 1 at the stagnation point of the Optimized XPROP's blade at 80% and 95% span.

Based on the pressure distributions of Optimized XPROP, similar differences are seen in the trends as were pointed out in the case of XPROP. Therefore, the trailing edge C_p spikes and higher value of C_p at the stagnation point seen in SU2's prediction, could potentially explain the differences between the performance curves of the two solvers.

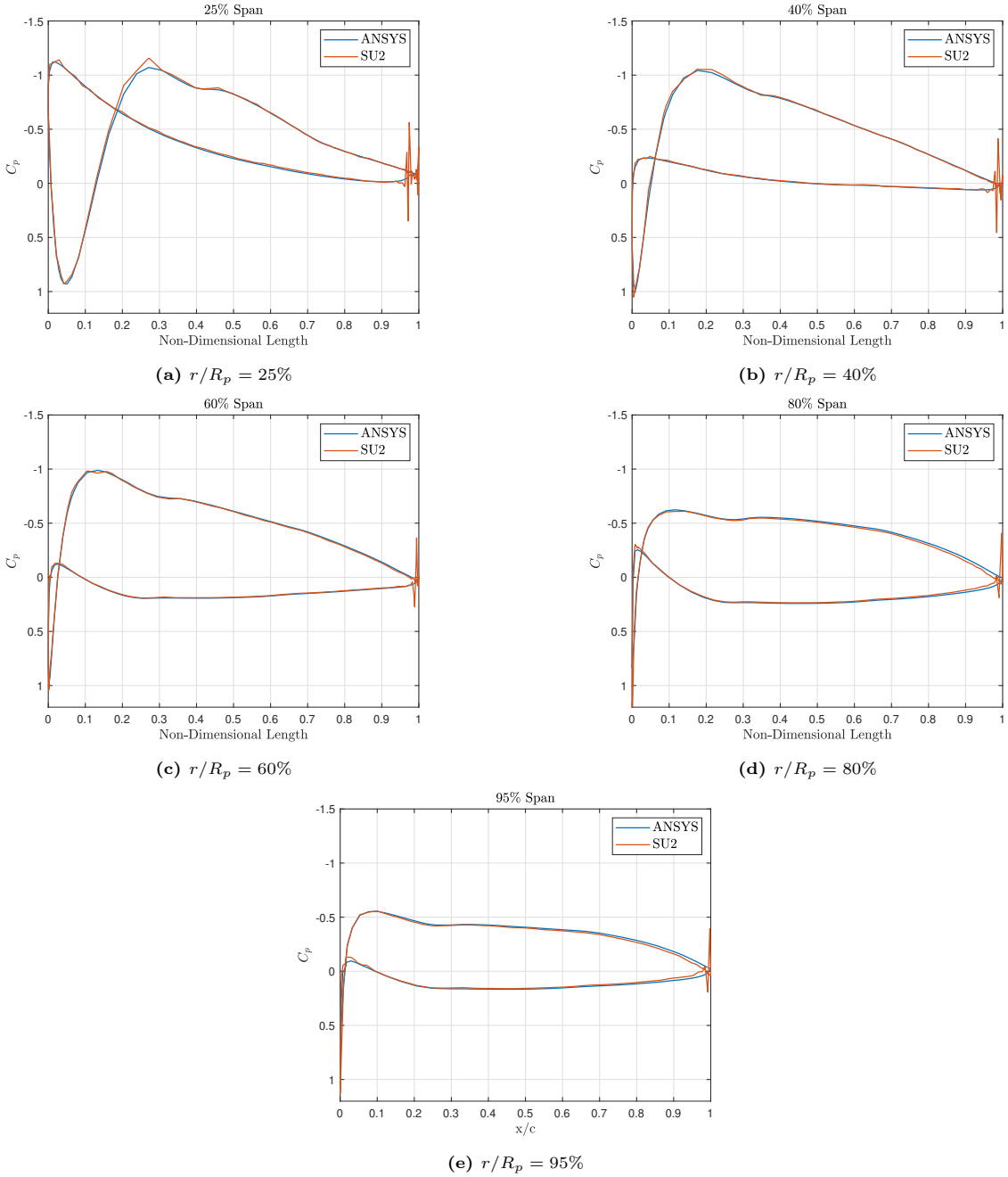

(a) $r/R_p = 25\%$

(b) $r/R_p = 40\%$

(c) $r/R_p = 60\%$

(d) $r/R_p = 80\%$

(e) $r/R_p = 95\%$

Figure 5.12: Pressure distribution at different radial spans of Optimized XPROP at J=1.0 from ANSYS Fluent and SU2.

5.1.4. Convergence Analysis

The convergence history of the residuals of flow equations on same computational mesh, from ANSYS Fluent and SU2 have been presented and compared here. The discussion is presented for XPROP and Optimized XPROP blade.

XPROP

The steady state calculations were performed using single rotating reference frame and conformal periodic boundary conditions with ANSYS Fluent and SU2. As discussed in Section 4.2.2, the CFL number of 1.0 was used for both the calculations. The criteria used to monitor and determine the convergence of the solution was a drop of at least 4 orders of magnitude for the continuity residual. Figure 5.13 displays the plots of convergence history from the two solvers.

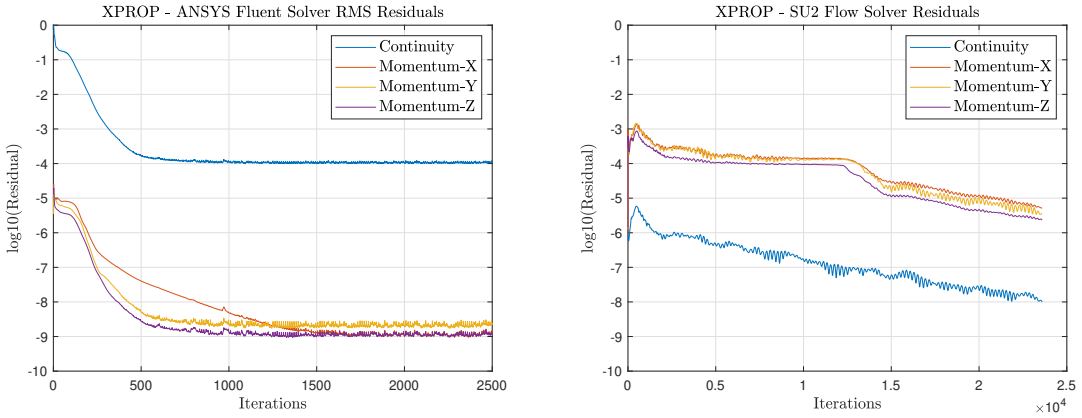

(a) ANSYS Fluent. **(b)** SU2's CFD Solver.

Figure 5.13: Convergence history for XPROP at J=1.0 with ANSYS Fluent and SU2

On observing the residuals, it can be inferred that ANSYS Fluent attains a drop of 4 orders of magnitude within 1500 iterations. Whereas, it takes 23,000 iterations for the SU2's solver to drop by 4 orders of magnitude.

Optimized XPROP

Similar to the setup of XPROP, CFL number of 1.0 was used for the simulations and convergence criteria was set at 4 orders of drop in residuals of the continuity equations. Figure 5.14 displays the plots of convergence history from the two solvers.

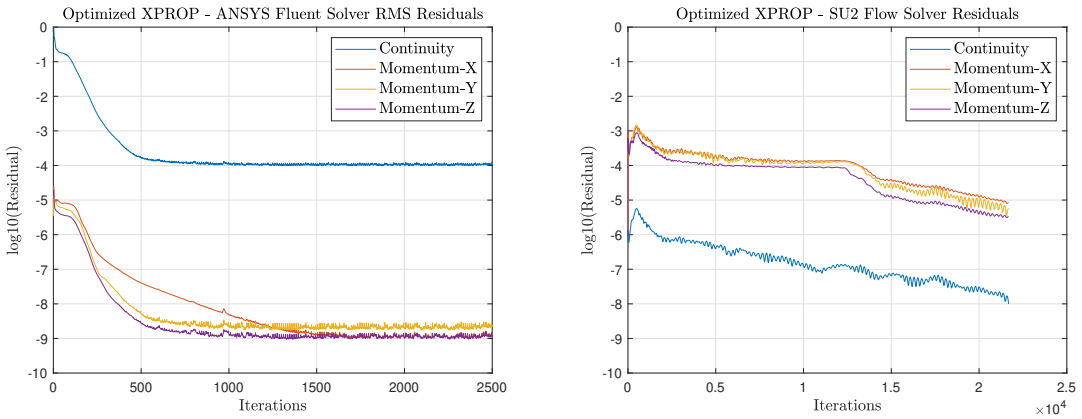

(a) ANSYS Fluent. **(b)** SU2's CFD Solver.

Figure 5.14: Convergence history for Optimized XPROP at J=1.0 with ANSYS Fluent and SU2.

For the Optimized XPROP's case, residuals of continuity equation with ANSYS Fluent attains a drop of 4 orders of magnitude within 1500 iterations. Whereas, it takes 22,000 iterations for the residual of continuity equation with the SU2's flow solver to meet the convergence criteria.

5.1.5. Discussion of Results

The SU2's results were compared and validated against the results obtained from commercial CFD solver ANSYS Fluent and experimental data (for the case of XPROP). Based on the grid convergence study, SU2's solutions were relatively more sensitive to the grid refinement for both the propeller cases as a larger deviation between the solution is observed as compared to the ANSYS Fluent's solution on the same grids. For all the cases of GCI, higher discretization error was attained with SU2.

Based on the observation of the performance curves, even though the two solvers show similar trends for the variation of C_T and C_P with advance ratios, SU2 underpredicted the values for both the propeller test cases at any given advance ratio. Such difference in the magnitude of the values can be partly

attributed to the difference in the type of solvers and numerical schemes the two CFD solvers use. The pressure distribution curves with the two solvers were compared to get an insight into the reason that could potentially explain such a difference in the performance curves.

Overall, a satisfactory agreement is seen between the ANSYS Fluent's and SU2's results based on the pressure distributions. However, discrepancies are seen in the pressure distribution with SU2 at the trailing edge of the blade sections in terms of large spikes in C_p. Additionally, SU2 tends to predict C_p greater than 1 at the stagnation points of the outboard blade sections for a flow with helical tip Mach number of 0.28. As such discrepancies in the pressure distribution could lead to different values of integrated loads and flowfield, it can be used to explain the offset seen in the performance parameter curves with the two solvers.

5.2. Aerodynamic Comparison of Isolated Propeller Configurations

The aerodynamic performance of XPROP and Optimized XPROP have been compared in this section for a range of advance ratio 0.6-1.2. As aforementioned, the simulations have been performed at fixed operating conditions as shown in Table 5.1. The results presented here are based on the flow simulations performed with SU2's CFD solver.

5.2.1. Performance Parameters

Figure 5.15, 5.16, and 5.17 depict the performance of both isolated propellers in terms of thrust coefficient, power coefficient, and efficiency versus advance ratio, respectively. Table 5.7 presents the quantitative values of the performance parameters for two propellers.

Table 5.7: Performance parameters of XPROP and Optimized XPROP

J	Thrust Coefficient (C_T)		Power Coefficient (C_P)		Efficiency (η)	
	XPROP	Optimized XPROP	XPROP	Optimized XPROP	XPROP	Optimized XPROP
0.6	0.314	0.318	0.324	0.329	0.582	0.579 (-0.374%)
0.7	0.284	0.286	0.309	0.313	0.643	0.642 (-0.196%)
0.8	0.251	0.254	0.289	0.293	0.694	0.693 (-0.105%)
0.9	0.21	0.219	0.265	0.269	0.736	0.735 (-0.058%)
1.0	0.181	0.184	0.236	0.239	0.766	0.766 (+0.087%)
1.1	0.143	0.146	0.201	0.205	0.782	0.783 (+0.190%)
1.2	0.103	0.106	0.161	0.164	0.72	0.776 (+0.469%)

From Figure 5.15, it can be inferred that the optimized XPROP yields higher thrust than the baseline XPROP propeller throughout the range of computed advance ratios. Qualitatively, a linear C_T is observed for both propellers.

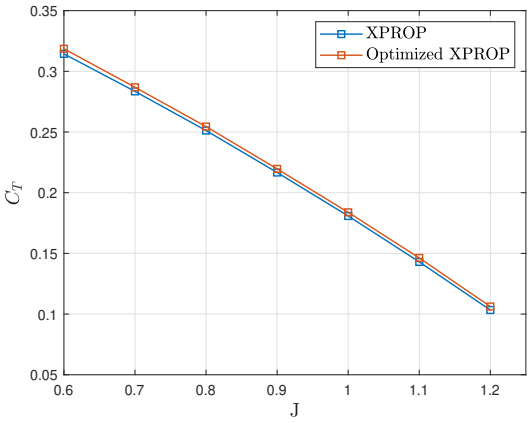

Figure 5.15: Comparison of Thrust Coefficient (C_T) of XPROP and Optimized XPROP.

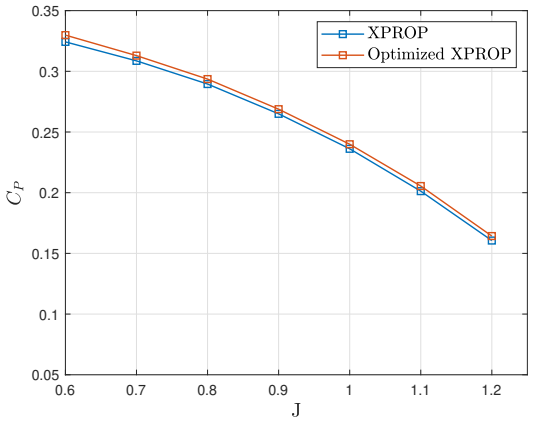

Figure 5.16: Comparison of Power coefficient (C_P) of XPROP and Optimized XPROP.

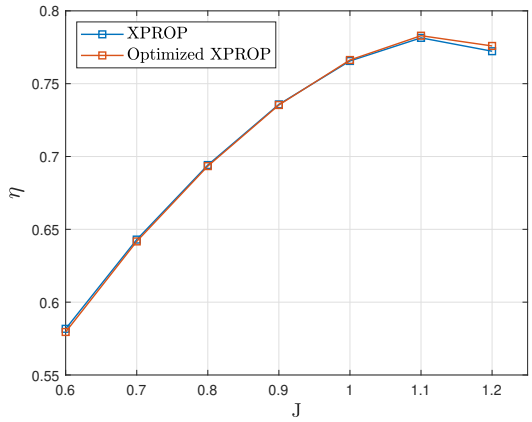

Figure 5.17: Comparison of Efficiency (η) of XPROP and Optimized XPROP.

Similar to the observations of the thrust curve, the Optimized XPROP attains higher power at any given advance ratio in comparison to XPROP as shown in Figure 5.16. Nonlinear identical curves are attained for both propellers throughout the operating range.

The above observations translate to the efficiency curves of both propellers shown in Figure 5.17. It can be seen that the Optimized XPROP experiences marginal loss in aerodynamic efficiency at low advance ratios from J=0.6 to J=0.9. While the benefit in terms of aerodynamic efficiency is attained at moderate and high advance ratios, with the largest gain of +0.469% at an advance ratio of J=1.2. For both propellers, the peak efficiency is achieved at J=1.1, beyond which the curve starts to drop off.

5.2.2. Blade Loading

Figure 5.18a and 5.18b displays radial thrust and torque distribution of XPROP and Optimized XPROP for various advance ratios, respectively. These distribution plots provide an insight into the reason for difference in the performance of the two blades. The radial thrust and torque distribution are plotted using the components of pressure and viscous forces acting on a spanwise element along the axis of rotation.

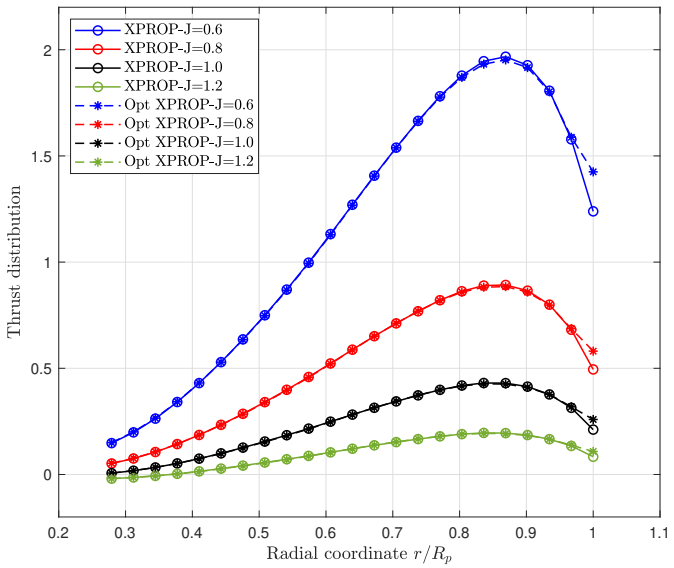

(a) Thrust Distribution

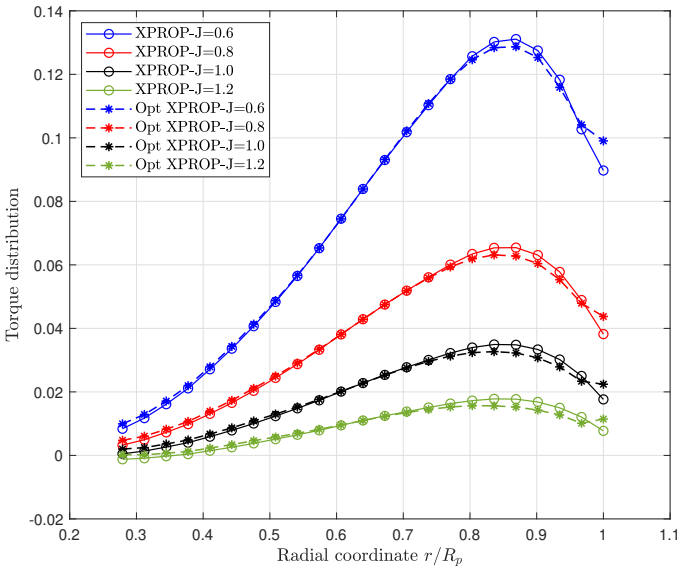

(b) Torque Distribution

Figure 5.18: Comparison of radial blade loadings of XPROP and Optimized XPROP.

On observing the radial thrust distribution of both the propeller blades at different advance ratios shown in Figure 5.18a, as the radial thrust loading flattens out as the advance ratio increases. It can be inferred that both blades obtain an identical load distribution for most part of the blade except outboard portion of the blade. Optimized XPROP attains a higher tip loading than the XPROP's blade. While, a redistribution of load is visible in 80%-90% span, as lower values of thrust are attained for the

Optimized XPROP's blade.

On observing the radial torque (power) distribution in Figure 5.18b, the torque loading of the two blades slightly differs along the span at any given advance ratio, contrary to the observations made for the thrust distribution. It can be seen that the elements within 70%-90% span along Optimized XPROP's blade generate lower torque as compared to XPROP. While the significant difference in comparison to XPROP's loading is seen at the tip, as Optimized XPROP's tip results in higher torque. In comparison with the thrust distribution, the deficit between the power distributions of the two blades especially at 80%-95% radius is larger at any given advance ratio.

From the foregoing observations, it can be inferred that for identical flow conditions, the sweep along Optimized XPROP's blade results in higher tip loading in comparison to the baseline XPROP blade. Moreover, a larger deficit exists in power distribution as compared to the thrust distribution of the two blades at any given advance ratio. This contributes to higher thrust and torque (power) values attained for the whole range of advance ratios as seen in the performance charts in Section 5.2.1.

5.2.3. Pressure Distribution

Figure 5.19 displays the pressure distribution curves of XPROP and Optimized XPROP blades at J=1.0 at different radial positions.

At 25% radius, two suction peaks represented by a negative value of C_p, are observed as a consequence of the incidence angle at the blade section being negative. As seen in Figure 5.19a, the first suction peak is attained at the pressure side followed by a second suction peak on the suction side. On moving outboard from the root section, the local incidence angle increases and the suction peak on the pressure side tends to reduce as the stagnation point moves towards the lower surface of the blade section. At 40% and 60% radius, similar pressure distributions are attained by the two propellers.

A similar shape of pressure distribution is observed at 80% radius, but the Optimized XPROP's blade has a marginally lower suction peak. This can be attributed to the increase in Mid chord alignment (MCA) i.e., sweep, on moving outboard. As aforementioned in Subsection 5.1.3, SU2 predicts a value of C_p greater than 1 at the stagnation point for both blades even though the flow is incompressible for this condition as tip helical Mach number is 0.28. A similar peak can be noticed in the incompressible simulations performed using SU2 [9]. At 95%, the Optimized XPROP attains a lower suction peak. Moreover, the Optimized XPROP attains slightly lower C_p values on the suction side's aft portion of the blade in comparison with XPROP.

On moving further outboard, it can be inferred that the pressure distributions at the 98% radius show the largest difference between the two blades. It must be mentioned that this radial position has the largest sweep (high MCA), in comparison to other radial positions shown in Figure 5.19. A redistribution of chordwise loading is apparent, as Optimized XPROP attains a lower suction peak at the leading edge and higher aft loading in comparison with the XPROP's section. The C_p value at Optimized XPROP's stagnation point is lower than that of XPROP. Such a difference in the C_p values at the stagnation point of the two blades could be potentially attributed to the different local induction factors as a result of different blade tip geometry [15]. Moreover, on observing XPROP's C_p curve, a small suction peak is visible on the pressure side of the leading edge. Whereas, Optimized XPROP's C_p seems to operate at an inflow incidence angle higher than that of the XPROP at the considered section. Thus, it would result in higher lift contributing towards high tip loading of Optimized XPROP.

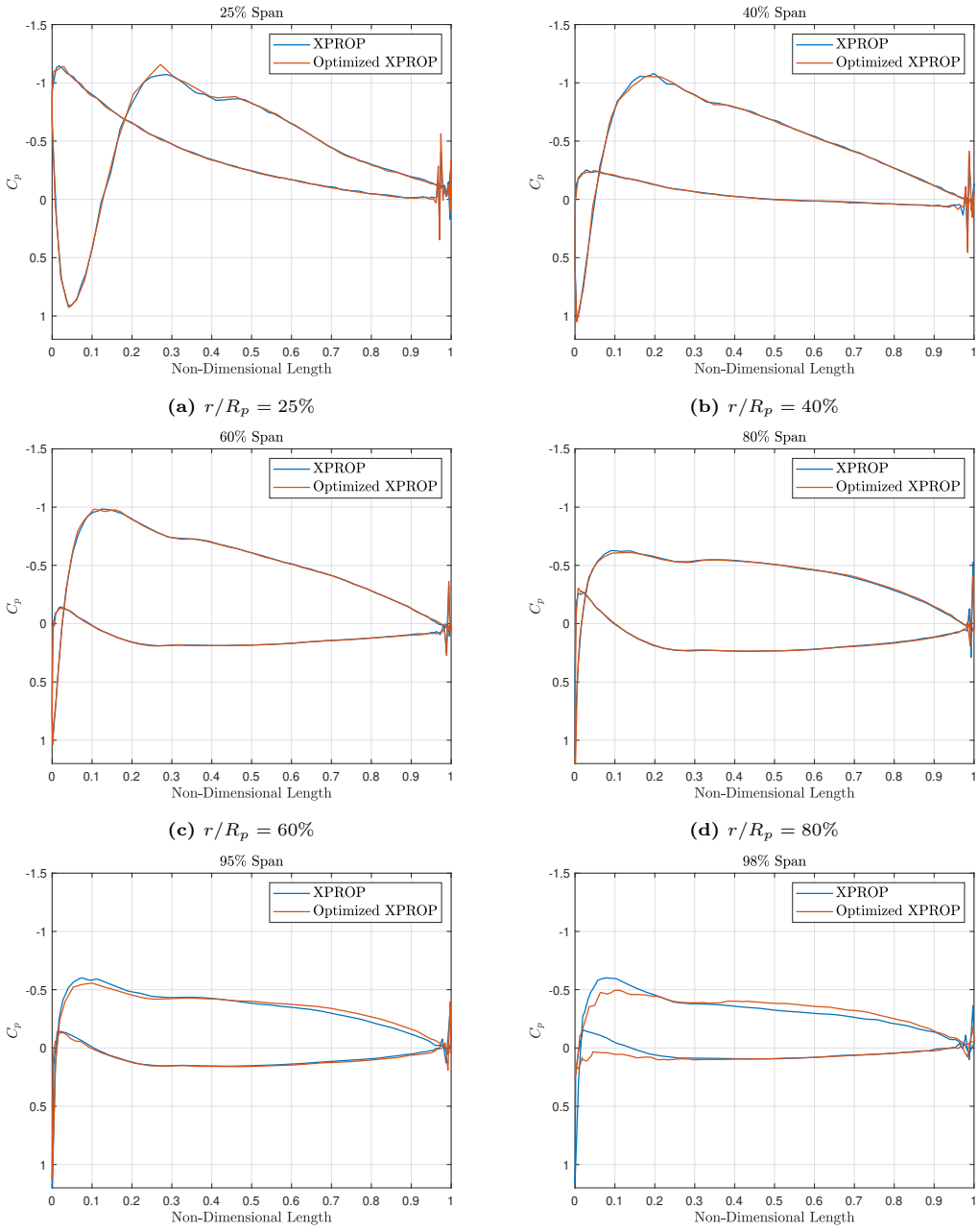

(a) $r/R_p = 25\%$ **(b)** $r/R_p = 40\%$

(c) $r/R_p = 60\%$ **(d)** $r/R_p = 80\%$

(e) $r/R_p = 95\%$ **(f)** $r/R_p = 98\%$

Figure 5.19: Pressure distribution at different radial spans of XPROP and Optimized XPROP at J=1.0.

5.2.4. Vorticity

In order to analyze the effect of the geometrical differences between the two propellers on the flow field, the vorticity distribution was analyzed at a station located 10%Rp downstream of the propeller blade for a steady-state computation at J=1.0. The vorticity distributions for XPROP and Optimized XPROP are shown in Figure 5.20a and 5.20b, respectively.

According to Figures 5.20a and 5.20b, two major regions of high vorticity are located at the blade tip and along the inboard portion of the blade near the root. The edge of the blade tips shed vortices downstream. Similarly, vortices from the inboard portion of the blade are shed downstream from the trailing edges. This acts as a source of the blade turbulence noise. Although, this turbulence noise will be negligible as compared to the tonal noise which comprises of loading and thickness noise.

On comparing the vorticity distribution between the two propellers, it can be seen that the vorticity magnitude near the tip of the Optimized XPROP's blade is higher as compared to the XPROP. Whereas, a smaller magnitude of vorticity can be seen along the inboard section of Optimized XPROP. The higher magnitude at the tip could be attributed to the higher tip loading of Optimized XPROP. From the preliminary judgement, it can be inferred that the high tip loading could result in increased sound radiation from the tip. With that being said, more insights into sound radiation from two blades can be provided by implementing an aeroacoustic model.

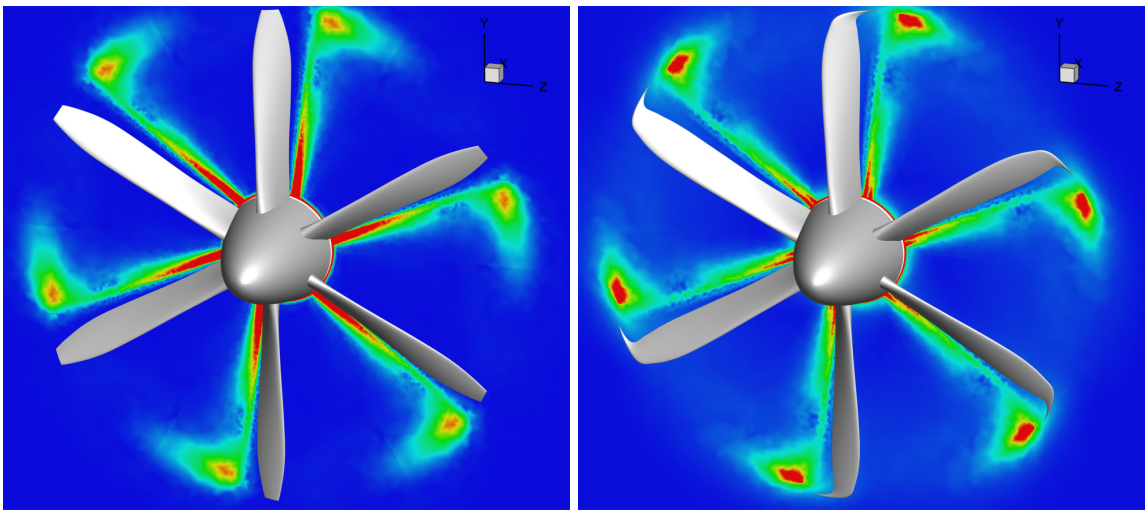

(a) XPROP. **(b)** Optimized XPROP.

Figure 5.20: Vorticity Distribution of XPROP and Optimized XPROP at J =1.0, at a downstream location $10\%R_p from the blade$.

5.2.5. Discussion of Results

On comparing the performance of the propellers based on the aerodynamic analysis done using SU2's CFD solver, it can be concluded that Optimized XPROP tends to achieve a higher thrust coefficient and power coefficient for the whole range of the computed advance ratios. For the identical flow conditions, the optimized blade operates with different loading distributions as a result of the swept tip. The blade thrust and power distributions showed higher load at the tip of the blade for Optimized XPROP at any given advance ratios. Although the thrust distribution is largely identical for a large part of the blade for the two propellers, the power distribution varies. A larger deficit in power distribution can be seen between the two blades as compared to the thrust distribution at any given advance ratio. Such differences have an effect on the aerodynamic efficiencies of the two propellers. As the advance ratio increased (lower helical tip Mach number), the Optimized XPROP gains a marginal increase in aerodynamic efficiency. The highest gain in efficiency of +0.47% is achieved at J=1.2. Whereas, the introduction of sweep results in a marginal loss in efficiency at lower advance ratios, the largest being at J=0.6 i.e., -0.37%.

The study of pressure distributions of the two blades didn't depict large differences for inboard blade sections, except redistribution of surface pressure for Optimized XPROP at 98% which was different from that of the XPROP. The redistribution of load at the tip results in higher lift and could be used to

explain the Optimized XPROP's higher tip loading. While studying the results it must be stated that there could be discrepancies in results due to the overprediction of pressure coefficient C_p values at the stagnation point by SU2's CFD solver. Additionally, the pressure spikes at the trailing edge of the blade where the pressure is interpolated smoothly can make results inconsistent.

The comparison of vorticity distribution showed variation in the magnitude of the vorticity shed by the two blades as a result of differences in the loading distribution. An increase in vorticity magnitude was observed near the tip of the Optimized XPROP blade due to higher tip loading. While there was a reduction in the vorticity magnitude near the inboard portion of the blade. Based on the observation of the spanwise blade loadings and vorticity distribution, a preliminary judgement can be made about the acoustic radiation of the blades, wherein higher tip loading could result in high sound radiation. Even though the introduction of sweep contributes to the reduction in sound but one must bear in mind that the operating conditions play a significant role. As concluded by Hanson, the shape variations have less influence at low Mach numbers [19]. That being said, the implementation of an aeroacoustic model would allow an exhaustive comparison between the acoustic performance of the two blades.

6

Sensitivity Analysis

This chapter presents setup and results of adjoint-based sensitivity analysis. The setup of the adjoint solver and parameterization of the blade is presented in Section 6.1. The results from adjoint-based sensitivity analysis of the XPROP and Optimized XPROP are discussed in Section 6.2 and Section 6.3 respectively. Finally, Section 6.4 presents a comparison between the two propeller blades cases based on the results of sensitivity analysis.

6.1. Parameterization and Adjoint Solver Setup

This section presents a discussion on parameterization of the test cases and setup of SU2's adjoint solver. The setup of adjoint solver comprises of - numerical implementation of the solver, choice of objective functions, and the effect of sharp edges on the sensitivity.

6.1.1. Parameterization

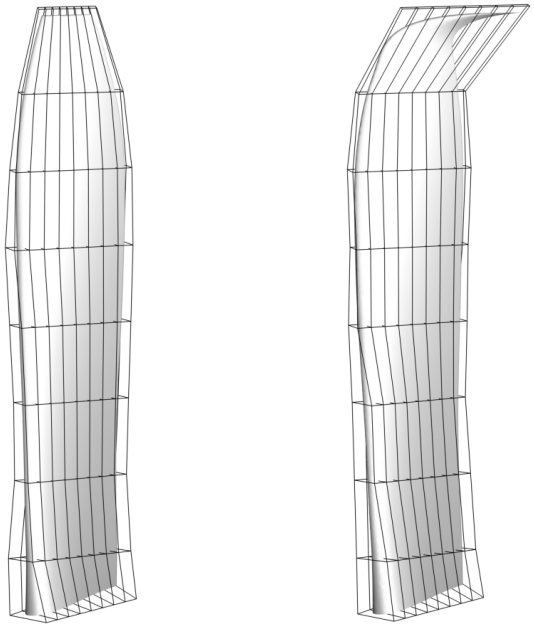

(a) XPROP **(b)** Optimized XPROP

Figure 6.1: Parameterization of XPROP and Optimized XPROP blades using FFD method.

In this research, the design variables have been chosen by using Free-Form Deformation (FFD) method. The number of FFD boxes and the control points have been chosen such that effect of surface deformation

on the objective function can be computed at large number of points on the blade. This provides crucial insights into the design of the aerodynamic surfaces and identify the most sensitive regions of surface for each objective function. In this study, the geometry of the blade is encapsulated by assigning 8 FFD boxes for parameterization as shown in Figure 6.1. The decision to use multiple FFD boxes for parameterization was to encapsulate the blade from root to tip while conforming to its varying shape due to twist and sweep distribution along the blade. The FFD control points of the defined FFD boxes are the three dimensional design variables used for surface deformation. Movement of the control points in the surface normal direction i.e., Z-direction was defined for all the 288 control points in the upper and lower surface of the FFD boxes. Even though dimensionality study has not been performed in this research, the number of FFD control points along the chord of the blade have been chosen based on the parameterization used in the different blade design studies [12]. Since, the FFD boxes for two blades have an orientation to conform to the twist and sweep distribution of the respective blades, the displacement of a particular FFD control point would result in different geometrical deformations in the two blades.

6.1.2. Adjoint Solver Setup

Numerical Implementation

After solving the RANS equations, the solution from the SU2's CFD solver and the computational mesh are used as an input to SU2's adjoint solver. Wherein, the adjoint solver uses the input to solve the adjoint counterpart of the RANS equations. SU2's discrete adjoint solver is implemented to perform the sensitivity analysis of the isolated propeller blades in this study. Similar to the flow solver, Jameson-Schmidt-Turkel (JST) centred scheme is used for the discretization of the convective fluxes. The convection of adjoint turbulence quantity is discretized using a scalar upwind scheme.

Objective functions

While setting up SU2's adjoint solver, the user needs to define the objective function and constraints for performing design studies. Since the current research deals with the sensitivity analysis itself, only objective functions were defined. This study deals with the sensitivity analysis of the propeller's performance parameters - thrust coefficient and torque coefficient, with respect to the geometric deformation of the propeller blade. Since thrust and torque have a combined affect on the aerodynamic efficiency of the propeller in the form of thrust to torque ratio, it was decided to perform the sensitivity analysis of the two parameters to study their individual response to the geometric deformation.

In contrast to the foregoing definition of thrust coefficient and torque coefficient in Chapter 5, alternative definitions are used- T_C and Q_C. Equation 6.1 and 6.2 present the alternative definitions of thrust coefficient, T_C, and torque coefficient, Q_C, respectively.

$$T_C = T/(q_\infty D^2) \tag{6.1}$$

$$Q_C = Q/(\rho_\infty V_\infty^2 D^3) \tag{6.2}$$

It can be inferred from the above equations that T_C and Q_C are defined based on the freestream conditions. These definitions provide clear insights into the average disk loading and the torque generated at the actuator disk.

Sharp Edge Sensitivity

The evaluation of the effect of the sharp edges in the geometry is important for the design studies as they impact the overall performance characteristics of the blade. The sharp edges can induce surface sensitivities that are an order of magnitude higher than the rest of the geometry and are, therefore, considered as an important design setting [38]. While it is a crucial setting from the design point, the evaluation of the sensitivities is difficult in these non-smooth regions.

The sharp edges are typically located at the trailing edge of the propeller blade. SU2 provides a sharp edge filter, that detects the sharp edges in the geometry and assigns sensitivity to 0 at that region. The effect of SU2's sharp edge filter on the surface sensitivities of the XPROP blade with T_C as the objective function is shown in Figure 6.2.

Due to the difference in the orders of magnitude in the surface sensitivities of the two cases, two contour bands with different ranges are shown. From the contours of T_C surface sensitivity, stark

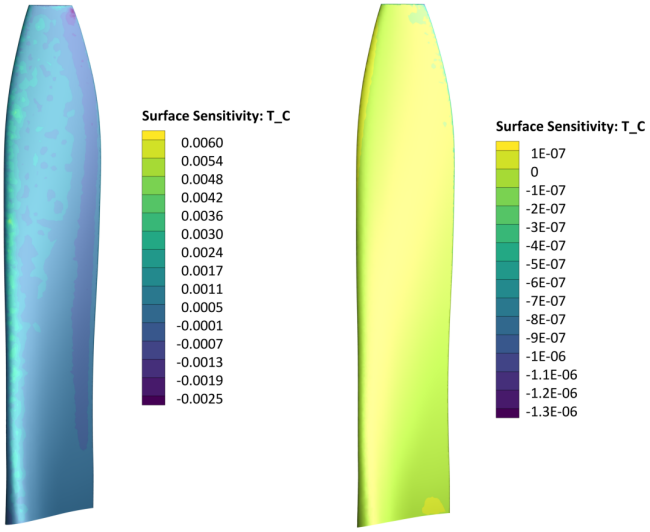

(a) Without sharp edge filter. **(b)** With sharp edge filter

Figure 6.2: Effect of SU2's sharp edge filter on the surface sensitivity of XPROP, with T_C as the objective function at J =0.8.

differences are seen in terms of the magnitude of surface sensitivities as the sharp edge filter tends to produce a contour where it is difficult to visualize the sensitive regions in Figure 6.2b. Whereas, the sensitive regions are clearly visible for the case without sharp edge filter as seen in Figure 6.2a. Based on the results, it can be concluded that the contribution from sharp edges is important for the sensitivity analysis of the propeller blade. Therefore, it was decided not to use SU2's sharp edge filter for further computations.

6.2. Sensitivity Analysis of XPROP

This section presents the results and discussion from the sensitivity analysis of the XPROP's aerodynamic performance parameters using the discrete adjoint method.

6.2.1. Convergence Analysis

The convergence history of SU2's flow solver and adjoint solvers for thrust coefficient and torque coefficient are shown in Figure 6.3, 6.4 and 6.5, respectively. For the convergence of the SU2's CFD solver, the residual of continuity equation is used as a monitor to meet the required threshold for the flow to be converged. From the flow solver's convergence history it can be inferred that the residual of continuity equation drops by 3 orders of magnitude within 23000 iterations. Similar observation is made for the component of momentum equations along the three spatial coordinates of the domain.

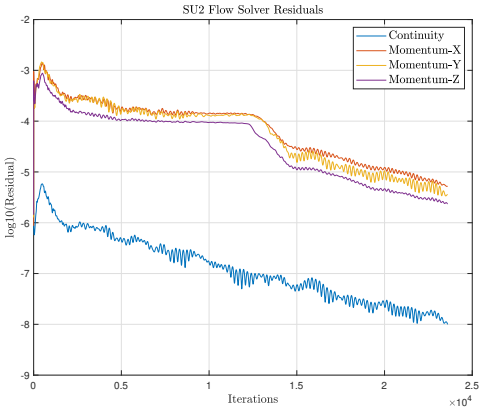

Figure 6.3: Flow Solver's convergence history for XPROP at J=.0.

According to the residuals from SU2's adjoint solver shown in Figure 6.4 and 6.5, the residual of the adjoint continuity equation ends up stagnating after 1.5 orders of drop in the magnitude. Similar convergence behaviour is observed for the residual of X-component of momentum equation for the two objective functions. In comparison to the flow solver, it can be noticed that it was more difficult to converge the adjoint solver. One of the potential reason for stall of the adjoint solver could be due to (relative) poor convergence of flow solver for the set criterion. Based on the validation of the adjoint gradients and deformation studies, a discussion on the convergence of adjoint solver is presented in Section 6.6.

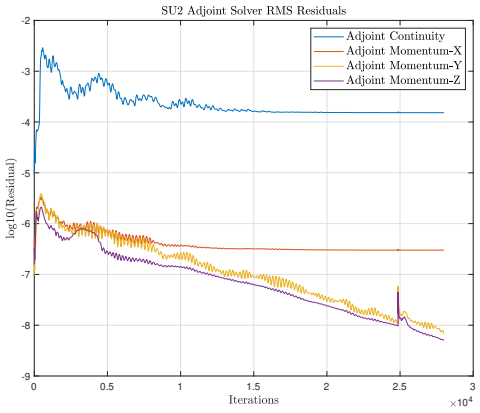

Figure 6.4: Adjoint Solver's convergence history for XPROP at J=1.0, with thrust coefficient as objective function.

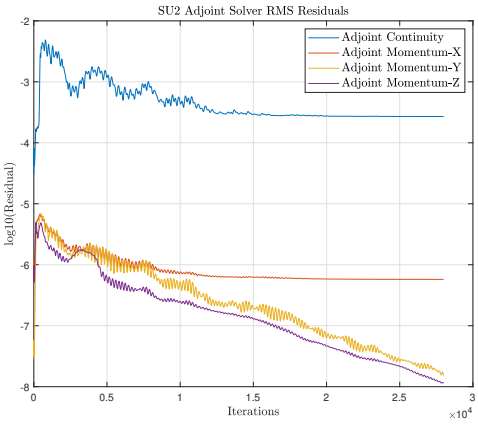

Figure 6.5: Adjoint Solver's convergence history for XPROP at J=1.0, with torque coefficient as objective function.

6.2.2. Objective function: Thrust Coefficient

Surface Sensitivities

The discrete adjoint method has been applied to analyze the sensitivity of the propeller's thrust coefficient T_C, to the deformation of blade shape controlled by the design variables, i.e., FFD control points. As mentioned before, the FFD control points are displaced in the surface normal direction (+Z-direction).

Figure 6.6 displays the surface sensitivity contours of XPROP's suction and pressure side for objective function T_C at different advance ratios. The surface sensitivity maps display the gradient of the objective function with respect to the normal displacement of the surface. It provides an insight to the designer by highlighting the regions of high sensitivity that on perturbation have a dominant effect on the objective function, as compared to regions of low sensitivity.

In Figure 6.6, the regions of high sensitivity are highlighted as yellow and dark blue regions. For yellow region, normal displacement of the surface outwards (i.e. in +Z direction) will result in an

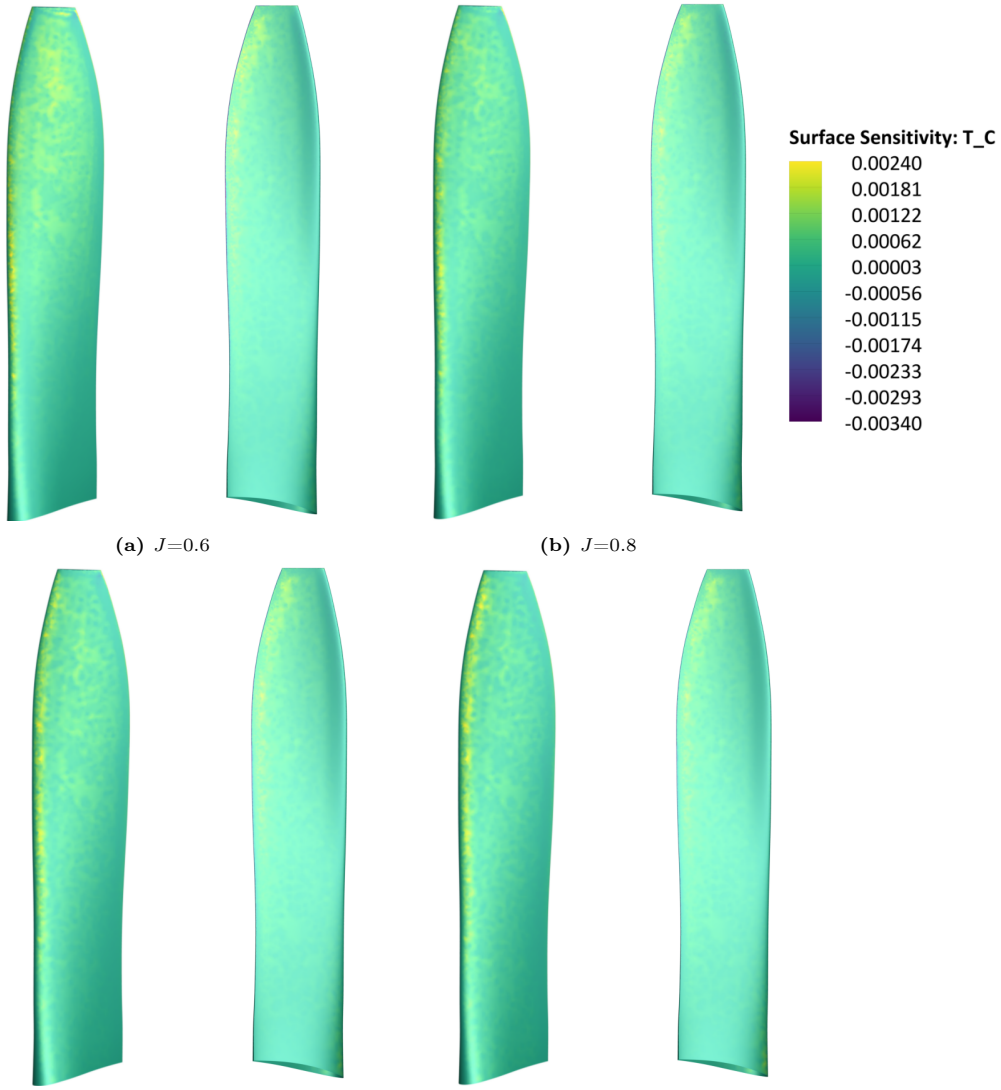

(a) J=0.6 **(b)** J=0.8

(c) J=1.0 **(d)** J=1.2

Figure 6.6: Surface sensitivity contours of XPROP's suction and pressure sides with Thrust (T_C) as objective function at various advance ratios.

improvement of the objective function i.e., T_C in this case. Whereas, moving the dark blue region inwards would improve T_C of the blade. The displacement of the light green region would relatively have a little effect on the objective function.

On observing the suction side of XPROP's blade at any given advance ratio, it can be inferred that region of high sensitivity (yellow spots) increases from root to tip, with highest being at 80%-90% radius. This region of high sensitivity along 80%-90% span, could due to the fact that region of highest radial blade loading is located here. The magnitude of this high sensitivity region tends to reduce on increasing the advance ratio from J=0.6 to J=1.2.

Additionally, regions of high sensitivity (yellow region) can be noticed along the leading edge of the blade's suction side. As the advance ratio increases, the extent of this high sensitivity region along the blade's leading edge tends to increase, extending from mid-span up to the blade's tip. Here, the regions of high sensitivity indicated in yellow suggest that on displacing the surface outwards in the normal direction, will increase the thrust as a result of increased camber near the leading edge.

Another region of high sensitivity (yellow region) lies at the tip of the blade's suction side. This high sensitivity region is apparent at a low advance ratio of J=0.6 and tends to reduce/disappear with increasing advance ratio. This could be explained by the presence of tip vortex at the blade's tip, and its intensity tends to reduce with increasing advance ratio (thus, low tip Mach number).

On the blade's pressure side, a region of high sensitivity (yellow region) is located along the trailing edge of the blade. This could potentially be a sensitive region, but one must bear in mind that sharp edges along the trailing edges can introduce gradients that are an order of magnitude higher than the rest of the geometry [38]. The effect of this was investigated in Section 6.5.

Gradients

Chordwise gradients of T_C at different radial positions along XPROP's blade are shown in Figure 6.7. The plots depict the variation of the chordwise gradients at different FFD control points along the chord, where design variable number DV = 1 to 9 represents the FFD control points starting from leading edge to trailing edge at all the radial positions. These gradients are with respect to the deformation of the FFD control points on the upper side of the FFD boxes.

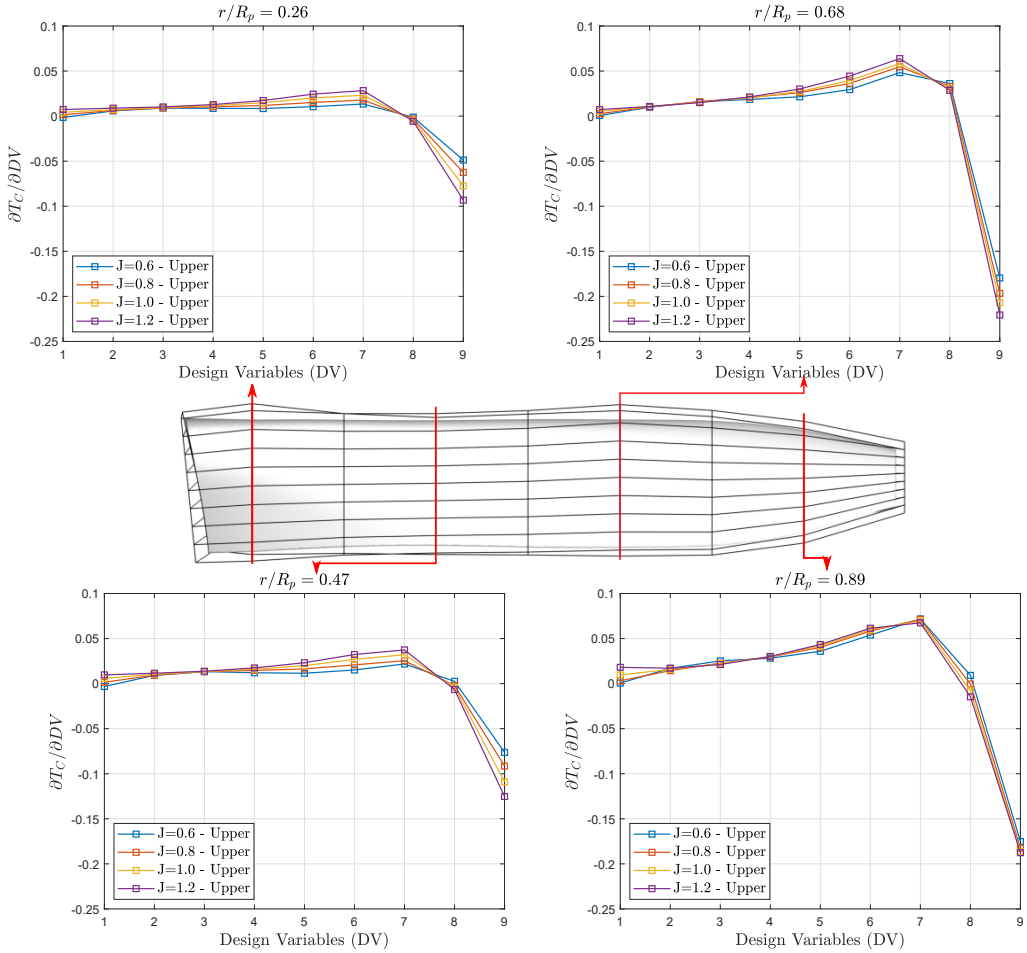

Figure 6.7: Adjoint gradient for thrust coefficient (T_C) as objective function along the chord at different span positions of XPROP blade. Here, DV=1 is located near leading edge and DV=9 is located aft of trailing edge.

On observing the chordwise gradient plots of T_C at different radial locations in Figure 6.7, it can be inferred that the magnitude of increment in the thrust gradient at a given chord position increases from root to tip. This is similar to the inference made from the surface sensitivity contours, indicating that any modification in the inboard section of the blade's suction side would have a little effect on T_C. Whereas, T_C will be relatively more sensitive to the deformation of outboard sections due to the increased loading.

From the chordwise gradient plots at all the radial positions, a variation in the magnitude of the thrust gradient with the chordwise position from leading edge to trailing edge is visible. It can be inferred that at a given radial position, the magnitude of thrust gradient increases upto design variable number DV=7, and beyond this point the direction of thrust gradient changes. The negative value of the thrust gradient on displacement of design variable DV=9, the displacement of this FFD control point in

+Z-direction would have a diminishing effect on the cost function. In other words, the cost function can be improved by moving the FFD control point in the opposite direction normal to the surface.

Based on the modulus of the thrust gradient, highest sensitivities are attained at the trailing edge of the blade for all the radial locations shown here. Although, part of the reason for high magnitude along the trailing edge could have been due to the presence of sharp edges at the trailing edge, however based on the investigation in Section 6.5, manual deformation of trailing edge had a dominant effect on the blade's performance.

At any given radial position on the outboard part of the blade, a trend of higher thrust gradient with increasing advance ratio is seen. This trend is clearly visible at the control points located on the aft part of the blade section. It can be explained by the variation in local flow characteristics at a given blade section due to varying advance ratio thus, affecting the local surface pressure distribution. For a constant freestream velocity, increasing the advance ratio by reducing the rotational speed, decreases the Reynolds number as well as local angle of attack. Such conditions alter the boundary layer characteristics of the flow and therefore it is important to inspect the boundary layer characteristic at a given section to explain the trend. A low-fidelity calculation using XFOIL was performed for this purpose.

Since it is essential to know the local angle of attack at the blade section to inspect the boundary layer characteristics, the following procedure is used. Local pressure distribution at 70% radius is extracted from the computed RANS solution at different advance ratios. Based on the area under the C_p curve (curve integral), the sectional normal force coefficient is calculated. XFOIL is used to perform the calculations on the extracted airfoil blade section at 70% propeller radius, for a range of operating conditions similar to the ones used for RANS calculations. For XFOIL computations, calculations are performed at Mach number and Reynolds number based on the local relative velocity at the 70% radius for each operating condition as shown in Table 6.1. Since the data RANS calculations were fully turbulent, the transition location was placed at 2% chord to simulate a fully turbulent flow over the airfoil in XFOIL. XFOIL calculations were performed for a range of angles of attack computed the pressure distributions along with other boundary layer parameters. The data obtained from XFOIL calculations are used to compare and find the normal force coefficient value which is same as that obtained from SU2's pressure distribution curves. The pressure distribution curves from two solvers are shown in Figure 6.8a. Even though this procedure does not lead to an exact equivalent pressure distribution between XFOIL's 2D and SU2's 3D C_p curves, it does estimate the magnitude of the local angle of attack at each advance ratio. Table 6.1 shows the estimated local angle of attack at 70% propeller radius for a range of advance ratio.

Table 6.1: Calculated conditions from CFD simulations.

J	$Re_{0.7R_p}$	M_{rel}	$\alpha_{0.7R_p}$
0.6	7.091e6	0.321	3.87°
0.8	5.465e6	0.247	2.09°
1.0	4.519e6	0.205	0.04°
1.2	3.910e6	0.177	-2.05°

On studying the boundary layer parameters obtained from the XFOIL calculations, the shape factor on the suction side of the airfoil is plotted. Figure 6.8 depicts the variation of shape factor on the suction side of the airfoil. High values of shape factor are attained at the leading-edge depicting transition from laminar flow, followed by a reduction in its value after transition. A shape factor of H=1.3-1.4 on the large part of the airfoil indicates turbulent flow. The shape factor towards trailing edge increases, indicative of increasing adverse pressure gradient and leading towards separation. It can be inferred that higher shape factor is attained at lower advance ratios. As the shape factor increases, the flow experiences higher adverse pressure gradient and increases as the flow approaches separation point. Thus, at low advance ratios the blade section experiences stronger adverse pressure gradient as compared to higher advance ratios. A deformation of geometry at low advance ratio could increase adverse pressure gradient and lead to an early onset of separation. Therefore, effect of geometry deformation on thrust would have higher benefit at higher advance ratios as compared to low. Moreover, the thicker boundary layer results in the reduced lift for the cases with strong adverse pressure gradient.

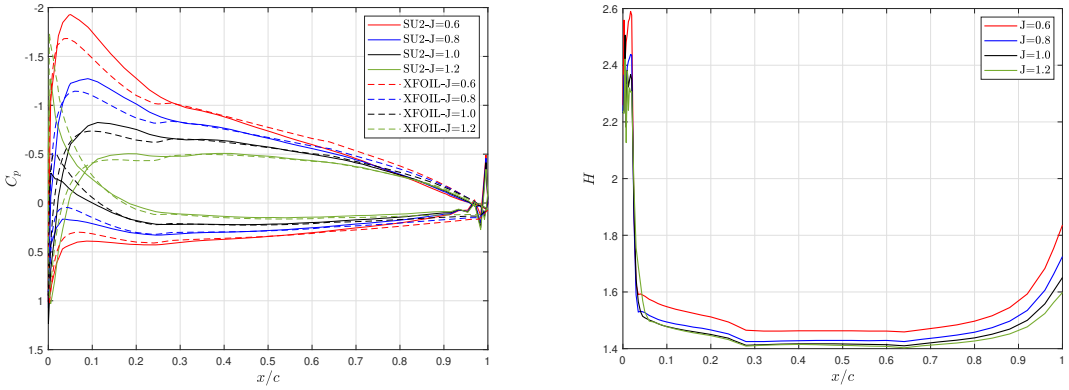

(a) Comparison of pressure distributions from SU2 and XFOIL calculations at various advance ratios.

(b) Chordwise variation of shape factor (H) on suction side for various advance ratios.

Figure 6.8: XFOIL Calculations for boundary layer properties at $r/R_p = 0.7$ of XPROP blade.

The adjoint gradients obtained using SU2's discrete adjoint solver are validated by performing the gradient calculation using Finite Differences (FD) method. A suitable step size of 0.001 was chosen for the gradient computation using FD method. Figure 6.9 shows the comparison between T_C gradients of XPROP's blade for J=1.0 at 57% and 89% radial positions. The comparison is drawn between the design variables located on the upper surface of the FFD box.

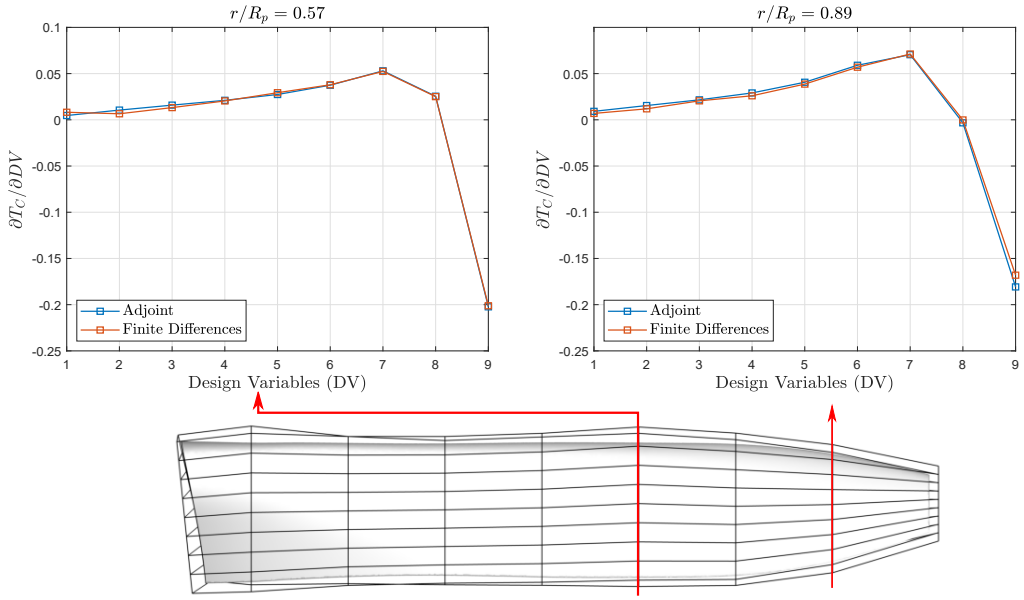

Figure 6.9: Gradient comparison of XPROP's thrust coefficient T_C at J=1.0.

On comparing the FD gradients with that of adjoint in Figure 6.13, chordwise trends of the two gradients are in good agreement in terms of the direction of the gradients at both the radial positions. On inspecting closely, differences are seen for the FFD points close to the leading edge at both the radial positions. While at the 57% radius, the gradients are well matched in terms of magnitude for the design variables located aft of design variable DV=6. In comparison to 57% radius, higher differences are noticed at 89% radius with largest for the design variable aft of the blade's trailing edge. Overall, a good agreement is seen between the gradients from the two methods.

Adjoint Flowfield

As pointed out by Marta et al. [31], an adjoint flowfield represents the adjoint solution at each grid point and is an adjoint counterpart of the physical flow variables. For example, an adjoint density is

interpreted as the amount by which the mass flux must be changed to increase/decrease the objective function of interest. This change can be induced by either changing the design of the blade or by changing the boundary conditions. Figure 6.10 shows the contours for adjoint momentum (X-direction) at 70% propeller radius of XPROP for different advance ratios.

The plots indicate that the region where momentum must be increased is largely present along the suction side of the blade section in the vicinity of the boundary layer. Especially, increasing the momentum in the region along the suction side's trailing edge would have a dominant effect on the thrust coefficient T_C. This is in line with the chordwise gradients, as the largest gradient was attained at the trailing edge for the radial position close to 70% propeller radius.

With increasing advance ratio, this region along the boundary layer spreads out further upstream with respect to the point close to the trailing edge, suggesting an increased portion of flow where higher momentum would reap benefits in T_C. Based on the adjoint flowfield, a designer can make geometrical changes to induce changes in the flow variables and attain the desired flowfield.

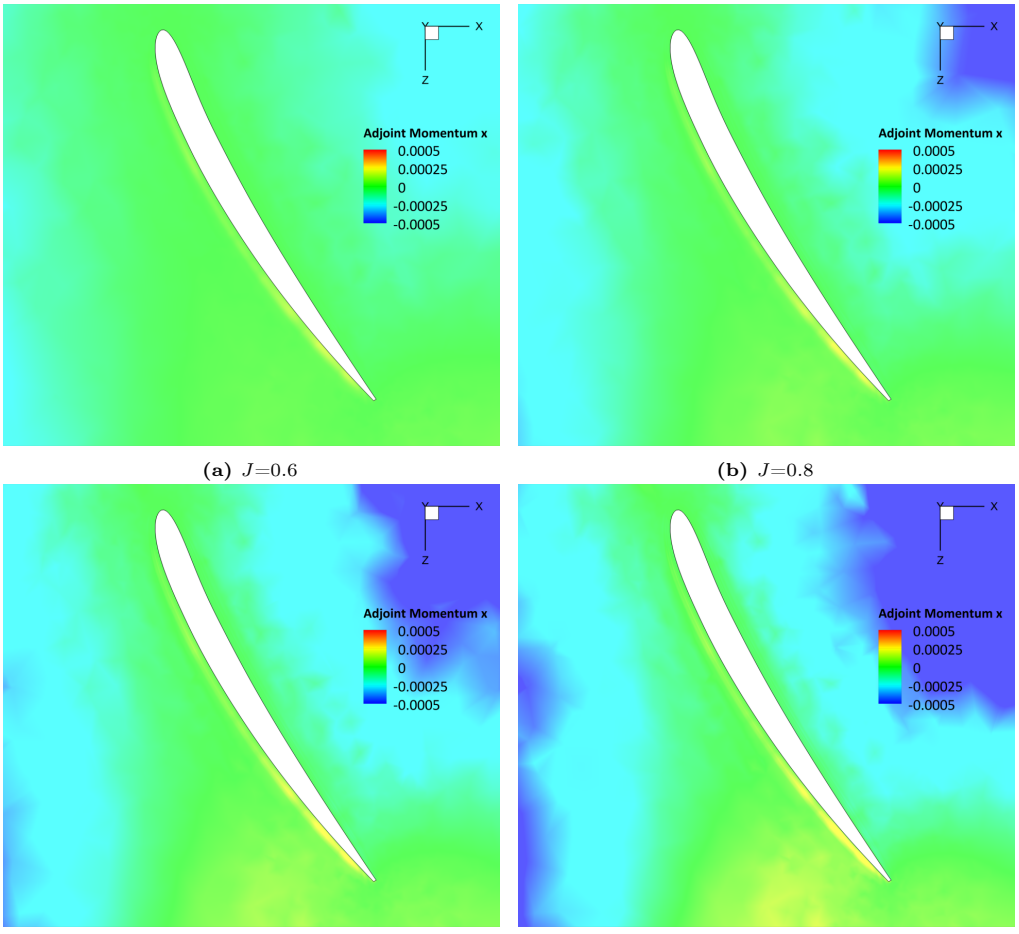

(a) J=0.6 **(b)** J=0.8

(c) J=1.0 **(d)** J=1.2

Figure 6.10: Adjoint solution for Momentum (X-direction) at 70% R_p of XPROP with Thrust coefficient (T_C) as objective function at various advance ratios.

6.2.3. Objective function: Torque Coefficient

Surface Sensitivities

Figure 6.28 displays the surface sensitivities of the XPROP's blade with torque coefficient Q_C as the objective function.

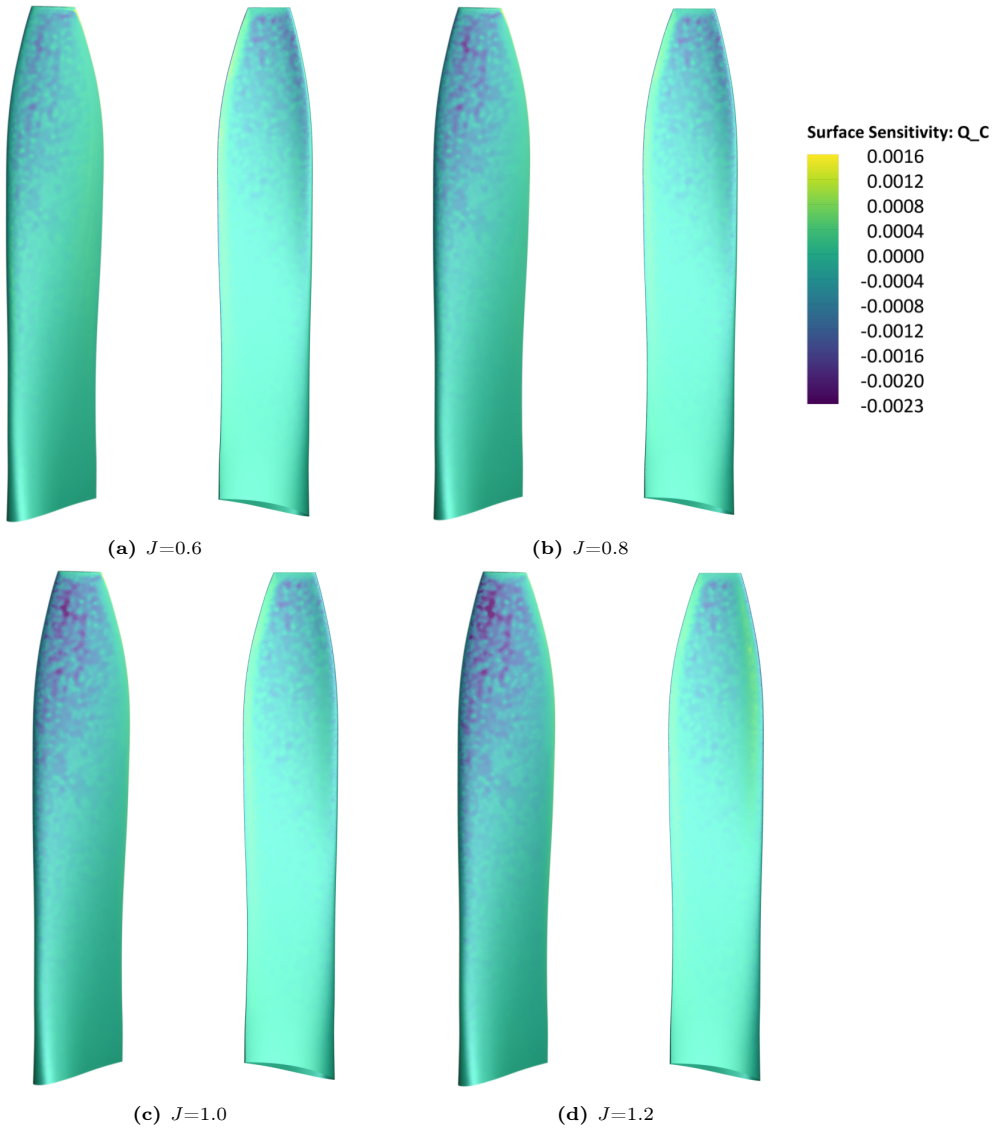

(a) J=0.6 **(b)** J=0.8

(c) J=1.0 **(d)** J=1.2

Figure 6.11: Surface sensitivity contours of XPROP with Torque (Q_C) as objective function at various advance ratios.

On the blade's suction side at any given advance ratio, the region of high sensitivity (dark blue) increases from hub to tip. It can be seen that the highest concentration of this sensitive region is found close to the blade tip. This can be attributed to the increase in torque loading from hub to tip. The spread of the high sensitivity region on the outboard suction side increases and spreads aft with increasing advance ratio. This indicates that the blade's torque coefficient becomes highly sensitive to the deformation in this region as the advance ratio increases.

Towards the trailing edge of the suction side a region of high sensitivity depicted as yellow is present. A similar trend was seen in the case of thrust gradient's surface sensitivity. This could be a sensitive region, but as aforementioned, sharp edges along the trailing edges can introduce gradients that are an order of magnitude higher than the rest of the region [38].

While on the pressure side, a similar increase in the sensitive region from root to tip is visible at any given advance ratio. However contrary to the suction side, this region of high sensitivity reduces on increasing the advance ratio from J= 0.6 to J=1.2, as can be inferred from Figure 6.11.

Gradients

Chordwise gradients of Q_C at different radial span positions along XPROP's blade are shown in Figure 6.12. Similar to the foregoing section, design variables 1 to 9 are the FFD control points along the blade's chord from leading edge to trailing edge.

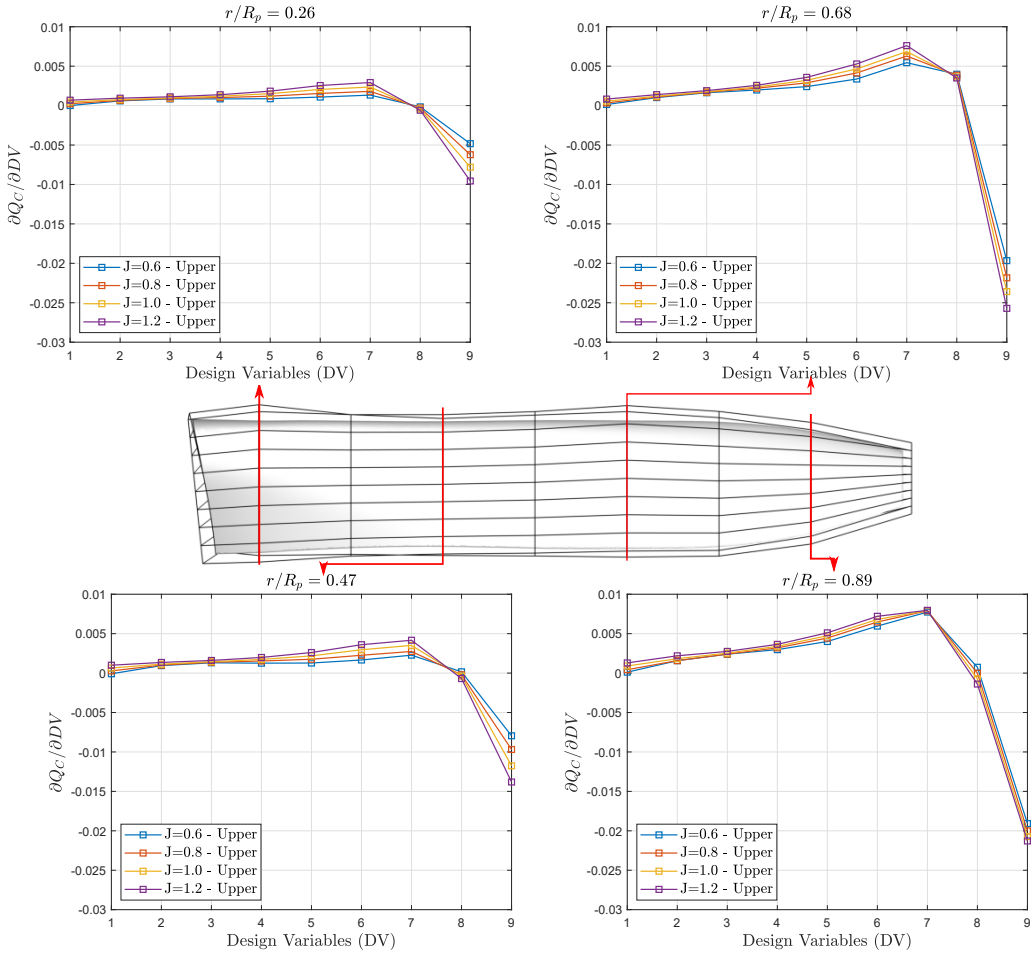

Figure 6.12: Adjoint gradient for torque coefficient (Q_C) as objective function along the chord at different span positions of XPROP blade.

The torque gradient at a given chordwise position increases from root to tip, similar to the inference made from the surface sensitivity contours. On observing the variation of torque gradient at different chord positions along the section, it can be inferred that the higher improvement in torque is attained on going downstream from the leading edge towards trailing edge for the surface normal deformation until design variable 7. Beyond DV = 7, the direction of the gradient tends to change towards the opposite direction. The highest modulus of torque gradient is attained at the trailing edge. This observation is similar to the trend seen in the case of thrust gradient. This trend is expected, as the normal displacement of the FFD control point in the +Z direction would increase the blade section lift due to an increase in camber. The increased lift results in an increase in thrust as well as torque. As the contribution from lift dominates towards the thrust and torque for the advance ratio except for the conditions close to zero thrust.

Similarly, the modulus of increment in torque gradient increases with increasing advance ratio which can be explained based on the increasing displacement thickness and shape factor at lower advance ratios, making it highly susceptible to separation. Thus, lowering the margin to improve the objective function. While interpreting the results, one must bear in mind that the term 'improvement' refers to the increment of the objective function. In practice, the propellers are designed to minimize the torque, in order to maximize the propeller's aerodynamic efficiency at a given thrust requirement. Thus, one would want to use the predicted gradient information to reduce the torque.

After observing the trends of the chordwise torque gradients, it is worth mentioning that the direction of the regions of the high sensitivity of Q_C (Figure 6.11) are opposite to that indicated by the chordwise gradients on the suction side. Such a trend is surprising.

The torque gradients from discrete adjoint solver are validated against the FD method. Figure 6.13 shows the comparison between Q_C gradients of XPROP's blade for J=1.0 at 57% and 89% radial positions. The comparison is drawn between the design variables located on the upper surface of the FFD box.

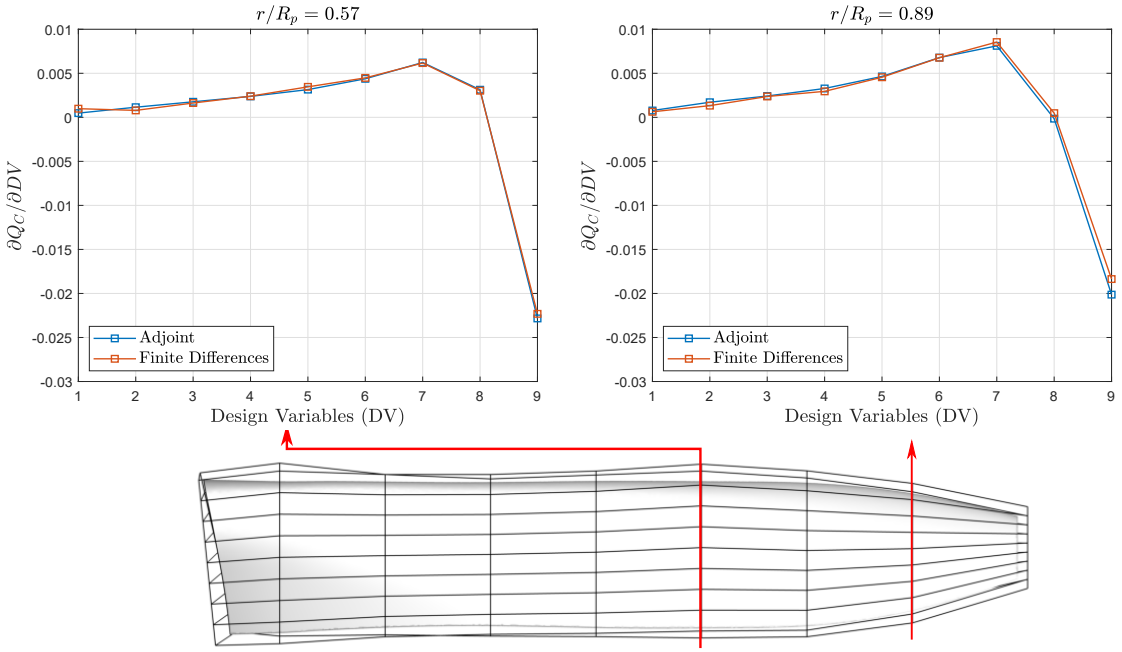

Figure 6.13: Gradient comparison of XPROP's torque coefficient Q_C at J=1.0.

The agreement between the Q_C gradients from discrete adjoint and FD method is good, as they exhibit gradients with same sign for all the design variables. Although, the adjoint method predicts a larger gradient for the design variable at the trailing edge of the blade sections at 57% and 89% radius. As seen in the case of T_C, the better agreement is seen of the design variables along 57% radius than the one along 89% radius.

Adjoint Flowfield

Figure 6.14 displays the contours for adjoint momentum (X-direction) at 70% blade radius of XPROP for different advance ratios with respect to the torque coefficient.

From the plots, it can be observed that any change in the region within the vicinity of the boundary layer along the blade's suction side would have a dominant effect on the variation of the Q_C as compared to other regions in the flowfield. While the change along the trailing edge portion of the blade section's suction side would have the highest effect. Similar trends were observed for the chordwise gradient at a span location close to 70% blade radius.

As the advance ratio is increased, the adjoint momentum close to the trailing edge increases. This suggests that there is a potential to obtain a larger increment in the Q_C by inducing delta change in the momentum (as a result of geometry variation or operating condition) at higher advance ratios. From the perspective of the propeller's aerodynamic performance, a lower torque is desired. In other words, the trailing edge must be designed with care as it has a dominant effect on the performance of the propeller.

Based on the adjoint flowfield for T_C and Q_C for XPROP, it can be concluded that the change induced in momentum along the suction side's trailing edge by altering the geometry, would have a dominant effect on the propeller's performance.

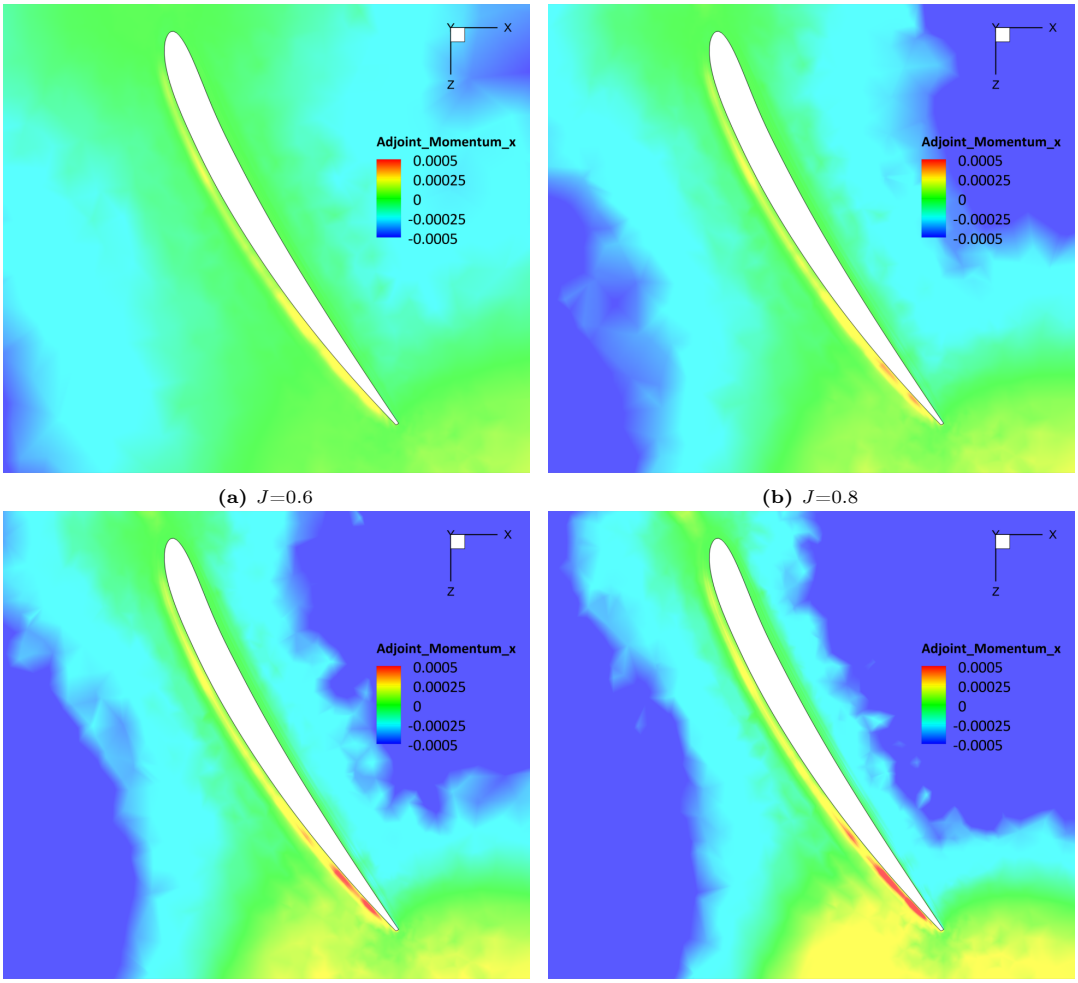

(a) J=0.6 **(b)** J=0.8

(c) J=1.0 **(d)** J=1.2

Figure 6.14: Adjoint solution for Momentum (X-direction) at 70% R_p of XPROP with torque coefficient (Q_C) as objective function at various advance ratios

6.3. Sensitivity Analysis of Optimized XPROP

This section presents the results and discussion from the sensitivity analysis of the Optimized XPROP's aerodynamic performance using discrete adjoint method.

6.3.1. Convergence Analysis

The convergence history of the flow solver and adjoint solvers for thrust coefficient and torque coefficient are shown in Figure 6.15, 6.16 and 6.17, respectively with Optimized XPROP at J=1.0. Similar to the case setup of XPROP, the continuity equation was assigned as the monitor variable for the convergence of the flow solver on meeting the threshold value. The residuals of continuity equation drop by 3 orders of magnitude within 22000 iterations. Similar order of drop is seen for the residuals of the momentum equations.

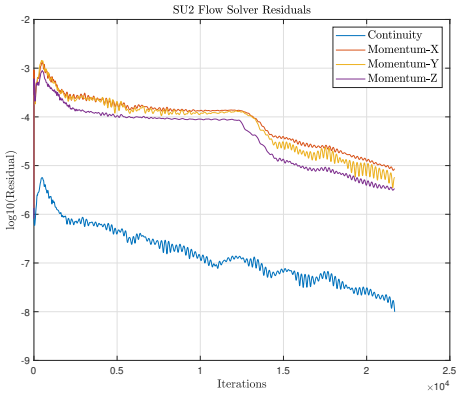

Figure 6.15: Flow Solver's convergence history for XPROP at J=1.0.

The residuals of the adjoint continuity equation for the thrust coefficient and torque coefficient stagnates after 1.5 orders of magnitude and does not change after 15000 iteration. This convergence behaviour is similar to the one observed in the case of XPROP. As aforementioned, one of the potential reasons could be the (relatively) poor convergence of flow solver. Based on validation of the gradients and deformation studies, a comment on the convergence of adjoint solver is made in Section 6.6.

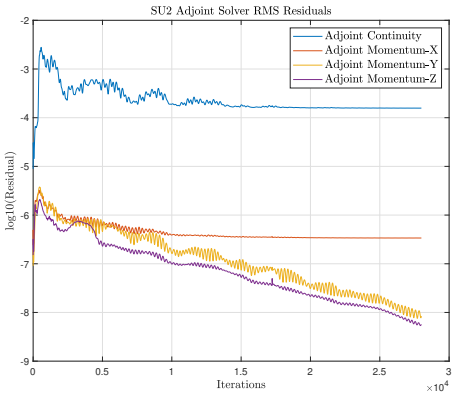

Figure 6.16: Adjoint Solver's convergence history for Optimized XPROP at J=1.0, with thrust coefficient as objective function.

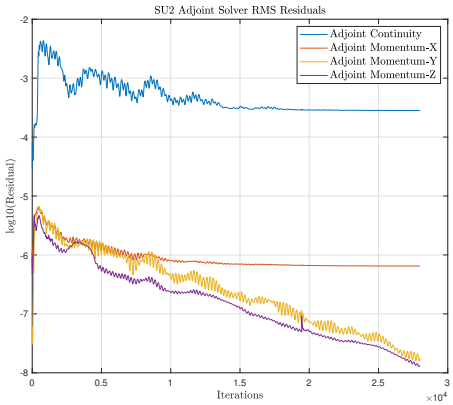

Figure 6.17: Adjoint Solver's convergence history for Optimized XPROP at J=1.0, with torque coefficient as objective function.

6.3.2. Objective function: Thrust Coefficient

Surface Sensitivities

Figure 6.18 shows the surface sensitivity contours of XPROP's suction and pressure side for a thrust objective function at different advance ratios.

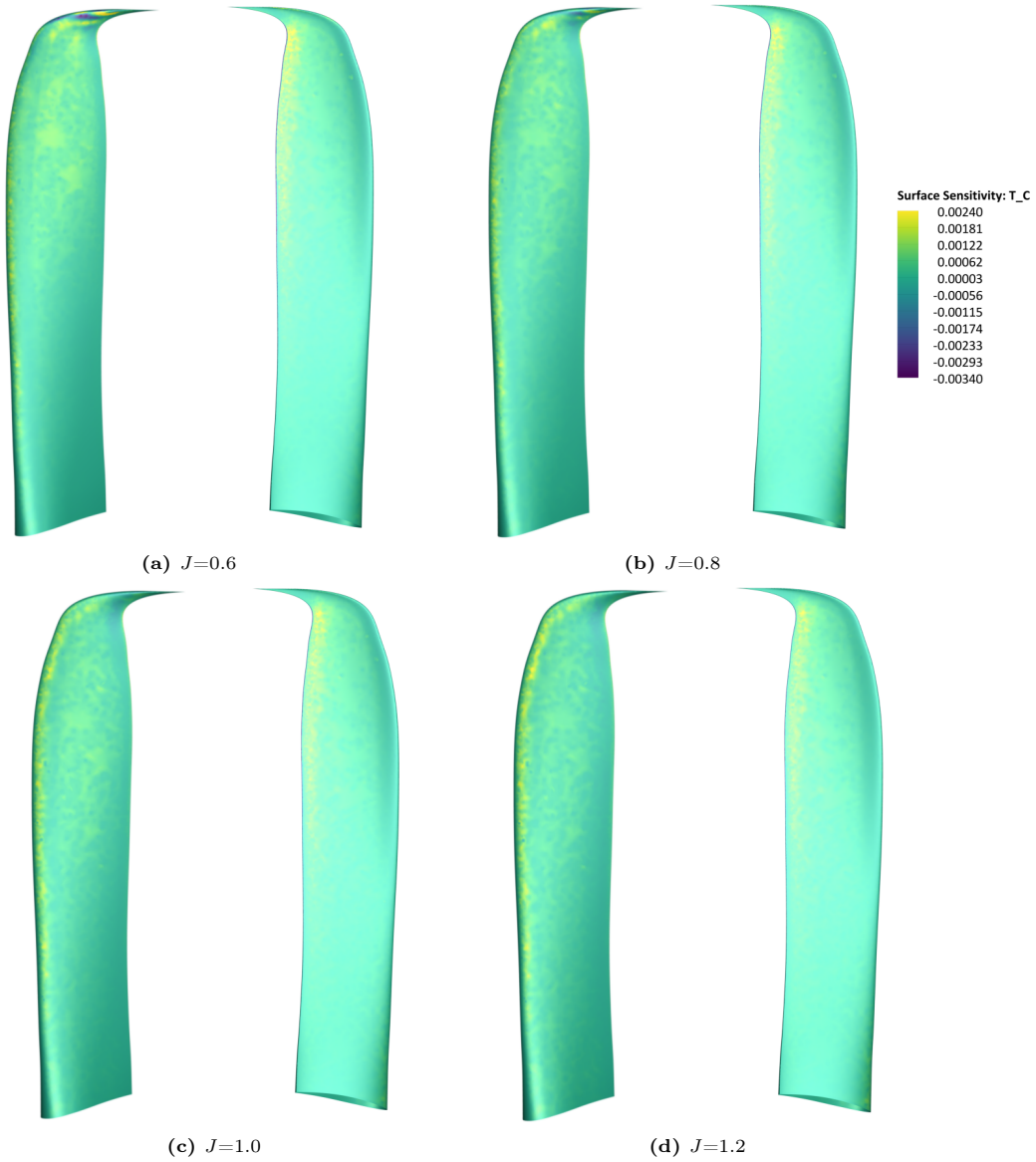

(a) J=0.6 **(b)** J=0.8

(c) J=1.0 **(d)** J=1.2

Figure 6.18: Surface sensitivity contours of Optimized XPROP with Thrust (T_C) as objective function at various advance ratios.

The regions of high sensitivity (yellow region) on the suction side become apparent on the outboard part of the Optimized XPROP at any given advance ratio. Similar to the case of XPROP, a region of high sensitivity (yellow region) is apparent along the leading edge of the blade that tends to increase along the leading edge, extending from mid-span upto the tip with increasing advance ratio.

While focusing on the effect of tip sweep on thrust in Figure 6.18a, a region of high sensitivity is attained at the contour of the tip. It tends to reduce with increasing advance ratio, as can be inferred from Figure 6.18b, 6.18c, and6.18d. This region of high sensitivity can be attributed to the presence of leading edge vortex at the blade's tip, as a result of high incidence angle at low advance ratios. Similar to XPROP, a region of high sensitivity (yellow region) is located along the trailing edge of the blade near the tip on the pressure side. This region tends to decrease with increasing advance ratio.

Gradients

Figure 6.19 displays the chordwise gradients of the thrust coefficient T_C for Optimized XPROP at various radial positions for different advance ratios.

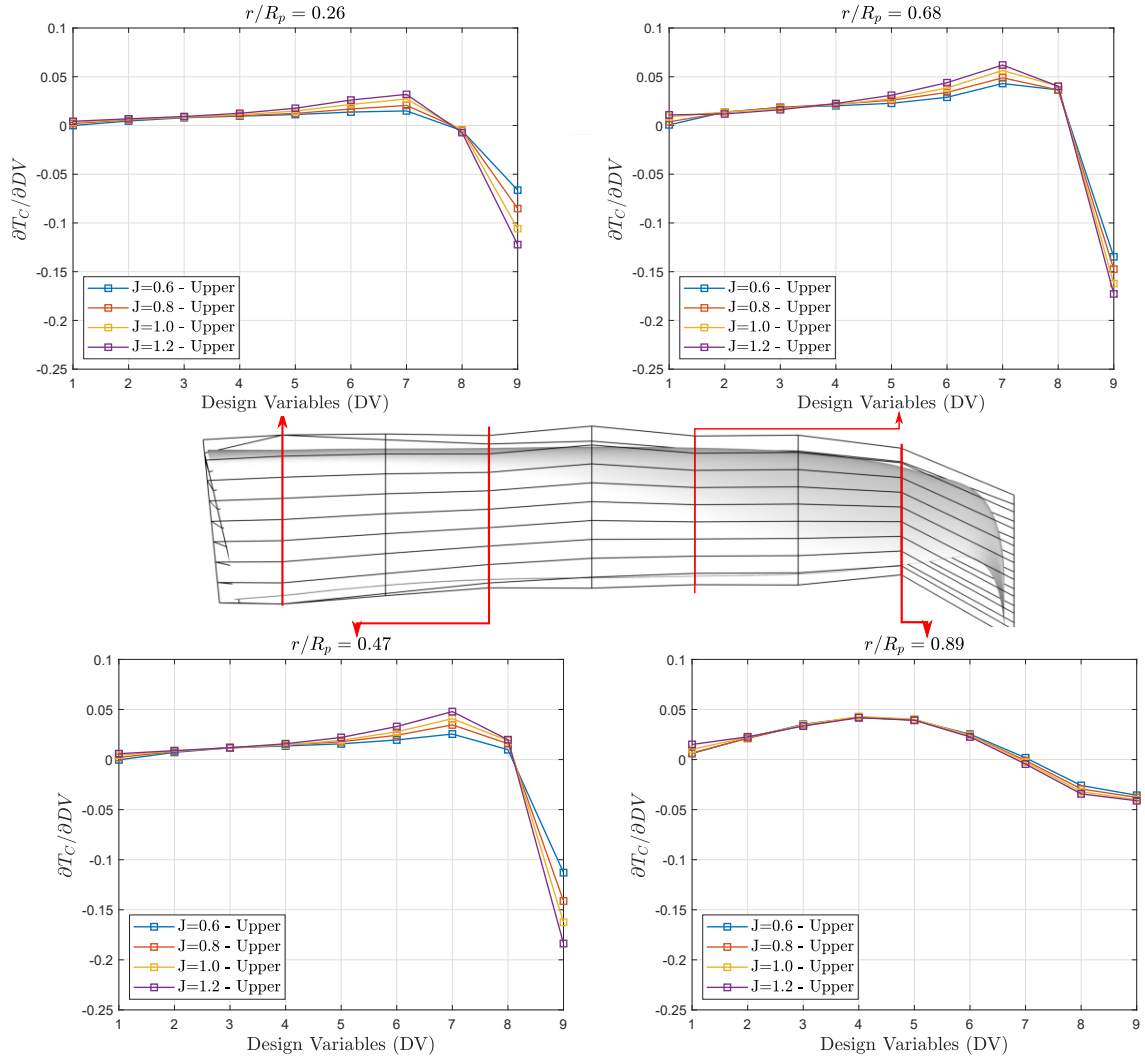

Figure 6.19: Chordwise adjoint gradient with thrust coefficient (T_C) as objective function at different radial positions along Optimized XPROP blade's suction side.

The thrust gradient at a given chord position increases from the root towards the tip as was seen in the case of XPROP. This means that the movement of the FFD control point located close to the root of the blade (and thus deforming region close to that) will have little effect on the thrust coefficient of the blade at any given advance ratio. While at 26%, 47%, and 68% radius, the highest modulus of thrust gradient is attained by moving the FFD control point located near the trailing edge.

The observed trends are similar to that of XPROP when it comes to the variation of the chordwise gradients with advance ratio at a radial span of 26%, 47%, and 68%. This is due to the fact that Optimized XPROP and XPROP have same airfoil chord and twist distribution, therefore reaping similar trends at a given advance ratio. Additionally, the sweep in this region of the blade is relatively less as compared to the outboard part of the blade.

Normal displacement of design variables near the blade tip at 89% radius results in a unique behaviour of chordwise gradients from leading edge to trailing edge for Optimized XPROP. This is the region where higher MCA i.e., sweep, is introduced in the blade extending up to the tip. Unlike the gradients at other radial positions, the trailing edge doesn't have a dominant effect on the objective function at this radius. Such a difference in the gradients could be explained by the differences between pressure distribution of blade sections in the tip region and the inboard sections. Based on the discussion on aerodynamic

performance of Optimized XPROP in Section 5.2, the chordwise load redistribution towards aft portion of the blade on suction side as well as leading edge vortex resulted in a C_p curve which was different from the ones at the inboard sections.

Except for 89% radius, the gradients located near the trailing edge of the blade sections are more sensitive to the variation in advance ratios. Whereas at 89% radius, these design variables are relatively less sensitive to the variation in advance ratios.

Figure 6.20 shows the comparison between discrete adjoint and FD gradients of XPROP's blade for J=1.0 at 57% and 89% radial positions with T_C as objective function. The comparison is drawn between the design variables located on the upper surface of the FFD box.

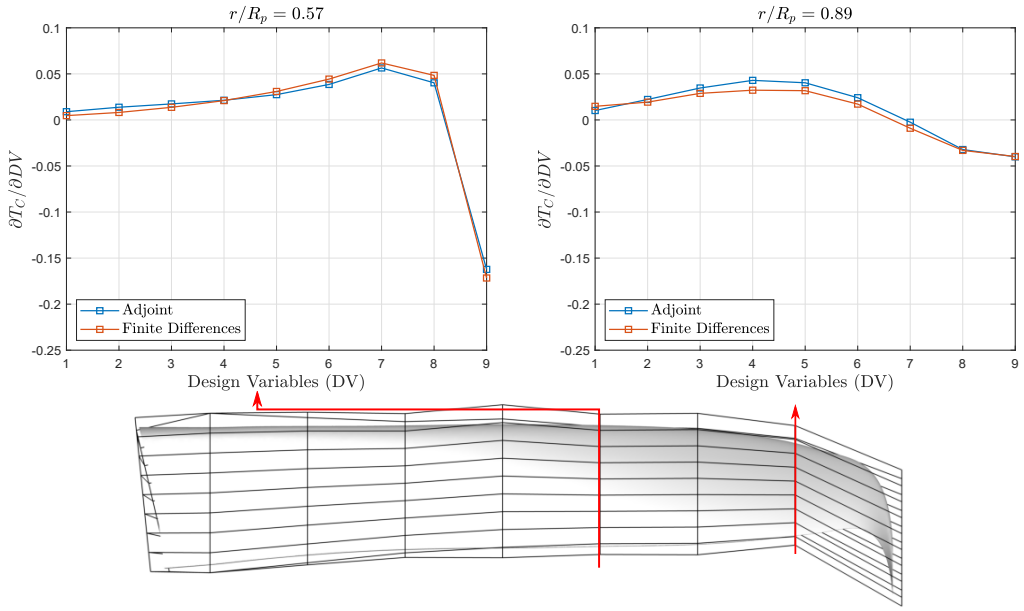

Figure 6.20: Gradient comparison of Optimized XPROP's thrust coefficient T_C at J=1.0 along the suction side.

From the gradient validation plots, it can be inferred that the direction of the gradients with FD and adjoint method are in a good agreement for the two radial positions. Although, differences in the magnitude is apparent. At 57% radius, the difference is dominant near the leading edge, where adjoint method predicts slightly higher magnitude of gradient. While, adjoint method underpredicts the magnitude of the gradients with respect to FD method for aft portion of the blade. At 89% radius, dominant differences between the gradients of two methods is seen for the design variables located along the mid chord at 89% radius, with largest for design variable DV=7. Part of the reason for such discrepancies can be attributed to the fact that FD method is prone to truncation errors. In comparison to the XPROP's gradient validation, larger differences are seen in the case of Optimized XPROP. Overall, a satisfactory agreement is seen between the gradients from two method.

Adjoint Flowfield

Figure 6.21 displays the flowfield of adjoint momentum (X-direction) at 70% blade radius of Optimized XPROP at different advance ratios, with thrust coefficient T_C as the objective function.

From the adjoint momentum (X-direction) plots, it can be inferred that inducing change in the region along the blade section's suction side has a higher potential for the increase in the T_C as compared to other regions. The observations of this adjoint solution is similar to that of XPROP with T_C, as any variation in the region close to suction side's trailing edge has a dominant effect on the thrust and this region is in the vicinity of the boundary layer. Similarly, the effect of variation of the advance ratio is same as that observed for XPROP.

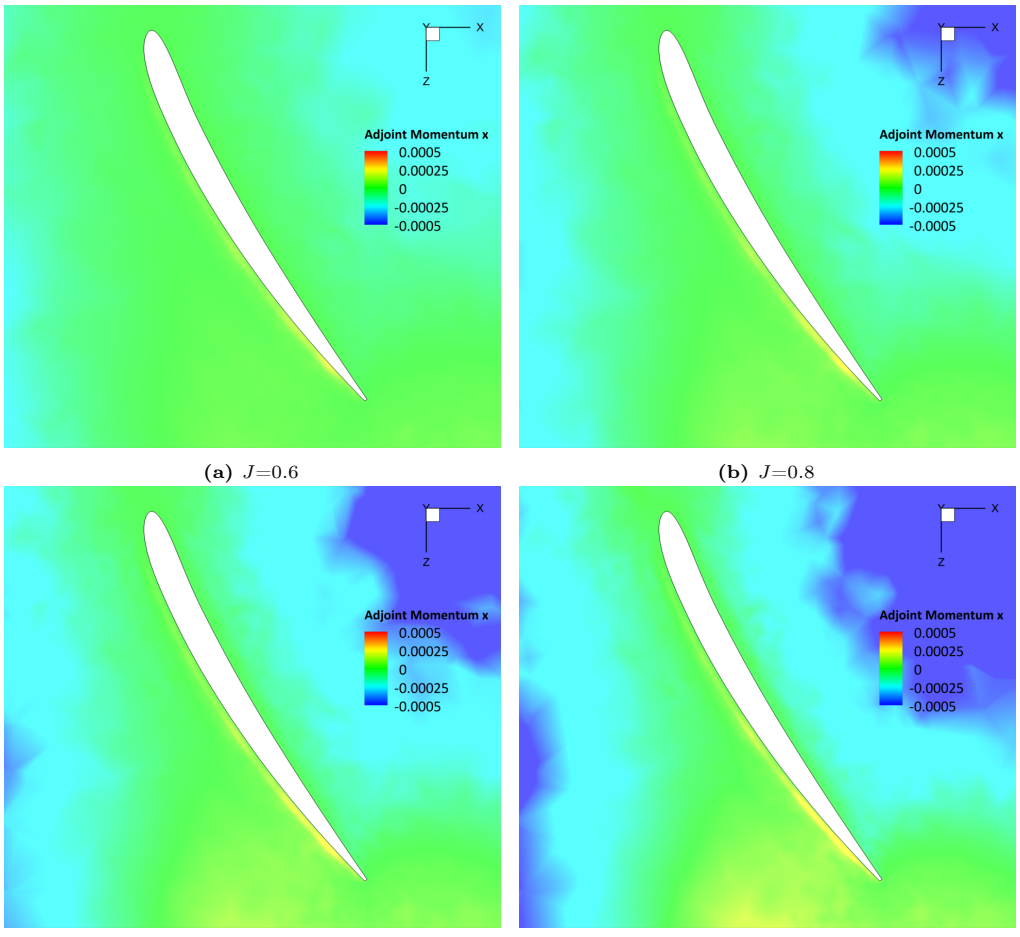

(a) J=0.6 **(b)** J=0.8

(c) J=1.0 **(d)** J=1.2

Figure 6.21: Adjoint solution for Momentum (X-direction) at 70% R_p of Optimized XPROP with thrust coefficient (T_C) as objective function at various advance ratios

6.3.3. Objective function: Torque Coefficient

Surface Sensitivities

Surface sensitivities contours of Optimized XPROP blade with torque coefficient as the objective function at various advance ratios is displayed in Figure 6.22.

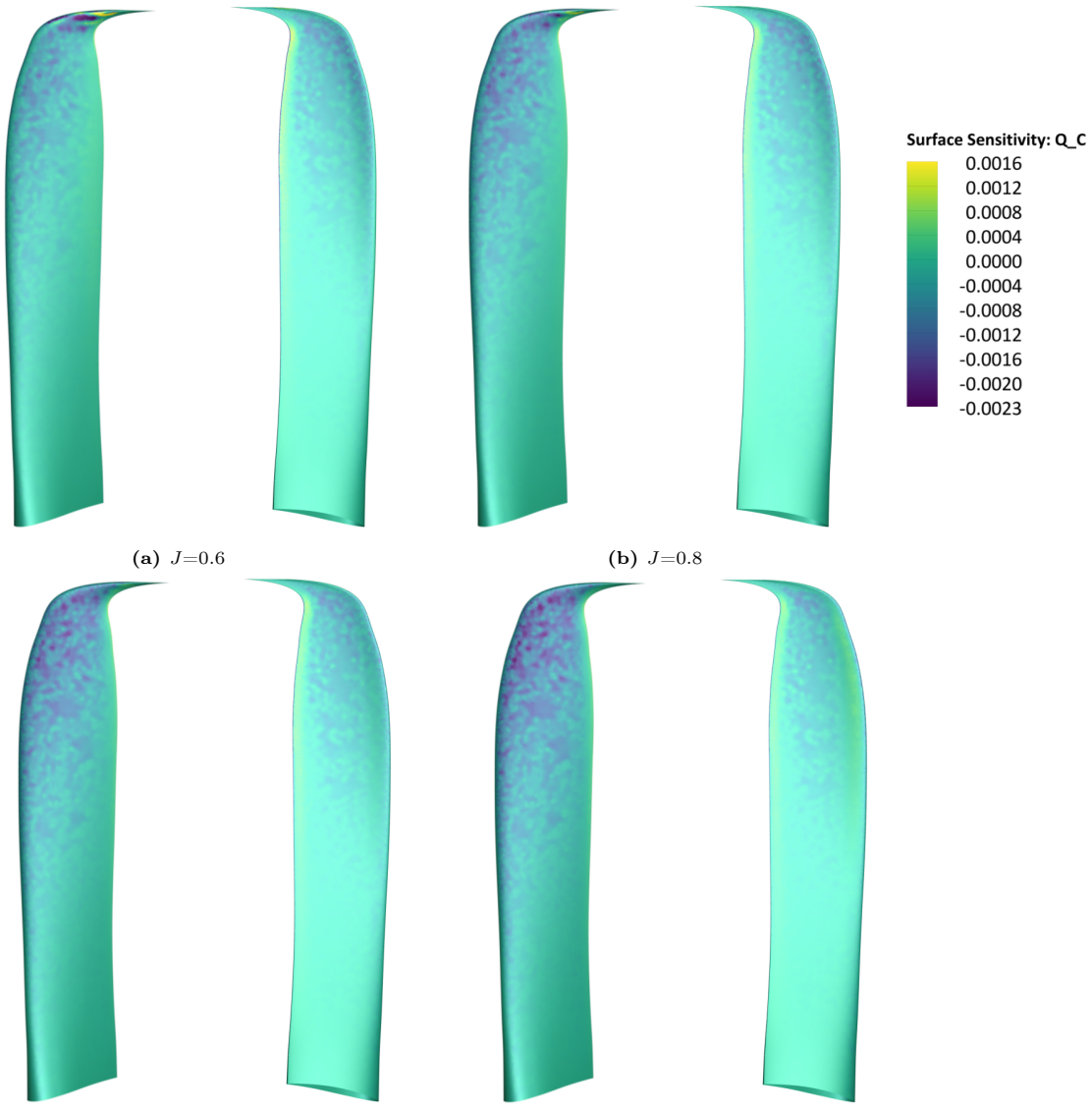

(a) J=0.6 **(b)** J=0.8

(c) J=1.0 **(d)** J=1.2

Figure 6.22: Surface sensitivity contours of Optimized XPROP with Torque (Q_C) as objective function at various advance ratios.

From the observation of the Optimized XPROP's suction side, the region of high sensitivity (dark blue) increases along the span of the blade at any given advance ratio. This is attributed to the increased torque loading with the radial position. Whereas, the concentration of this high sensitivity region tends to increase and spread towards the aft of the blade with the increasing advance ratios. This could be explained by the decreasing local angle of attack at the blade section with increasing advance ratios.

Similar to the thrust gradient, a region of high sensitivity (dark blue and yellow region) is visible at the contour of the swept tip Figure 6.22a. This region tends to disappear/reduce in concentration with increasing advance ratio. This could suggest the presence of vortex formation along the leading edge of the swept tip, which tends to reduce at higher advance ratios (low loading).

Whereas on the pressure side, a region of high sensitivity (dark blue) increases from hub to tip. On increasing the advance ratio, this region tends to reduce. Additionally, region of high sensitivity (yellow)

is apparent along the trailing edge of the blade's pressure side.

Gradients

Figure 6.23 displays the chordwise gradients of the torque coefficient Q_C for Optimized XPROP at various radial positions for different advance ratios.

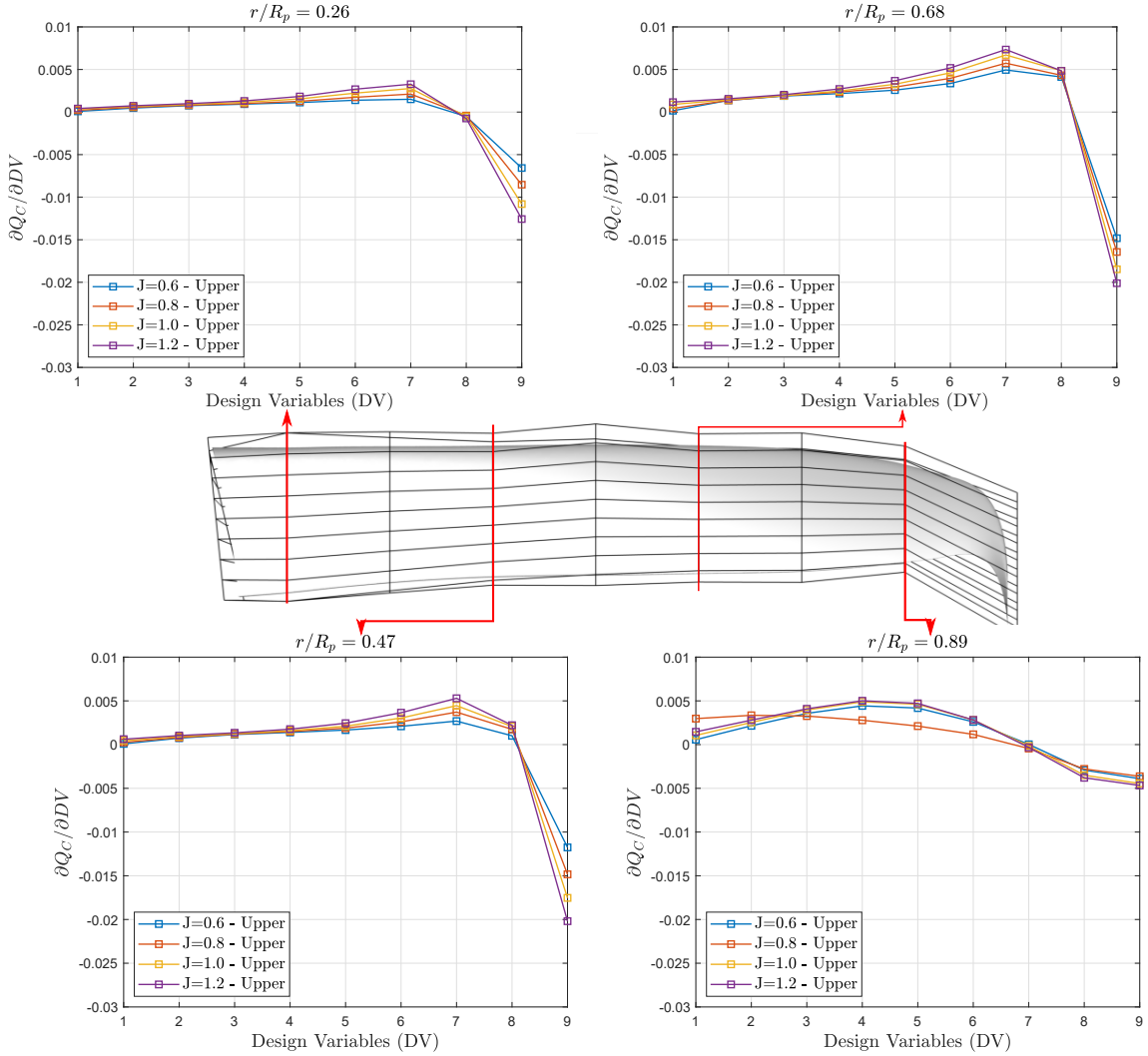

Figure 6.23: Adjoint gradient for torque coefficient (Q_C) as objective function along the chord at different span positions of Optimized XPROP blade.

On analyzing the chordwise torque gradients at 26%, 47%, and 68% radius, it can be inferred that magnitude of gradient increases from the root towards the tip as was seen in the case of XPROP. This means that the movement of the design variables located close to the root of the blade (and thus deforming region close to that) will have little effect on the torque coefficient of the blade at any given advance ratios. At these radial positions, highest modulus of thrust gradient is attained by moving the design variables located near the trailing edge. As was seen in the case of XPROP, higher torque gradient with increasing advance ratio is attained at a given radius and this effect is more apparent in the aft of the blade section. This can be attributed to the stronger adverse gradients experienced at lower advance ratios, making it reap less advantage of the geometric deformation.

Whereas, at 89% radius, the chordwise trends are unlike the ones observed at the inboard portion. As aforementioned introduction of sweep in the outboard portion of the blade redistributes the chordwise pressure distribution and could explain such a deviation from the trend of chordwise gradients seen at the inboard section. The Q_C gradients at 89% radius show a trend similar to the ones observed in case

of T_C, as the design variable that has a dominant effect on the objective function is now located along the mid-chord of the section, except for the case of J=0.8.

As was seen in the case XPROP, the gradients of Q_C suggest a trend opposite to that of the surface sensitivity contours. That is, the surface sensitivity contours depict the reduction in Optimized XPROP's Q_C, on the normal displacement of the design variables in +Z-direction. Whereas the gradients shown in Figure 6.23, suggest that Q_C would increases on moving the design variables in +Z-direction.

Figure 6.17 shows the Q_C gradient comparison between the discrete adjoint and FD gradients for Optimized XPROP at 57% and 89% radius for J=1.0.

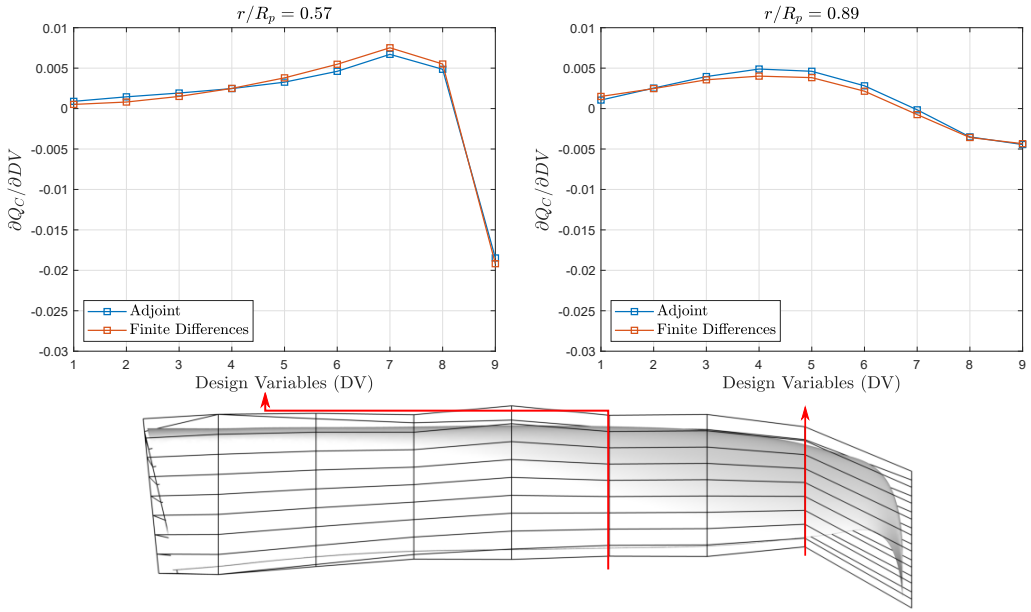

Figure 6.24: Gradient comparison of Optimized XPROP's torque coefficient Q_C at J=1.0.

The direction of the gradients from the two methods at the 57% and 89% radius are in good agreement. Although, deviation is seen at 57% radius in terms of magnitude where adjoint method underpredicts the gradients for design variables near the leading edge of the blade, while overpredicting for the ones along the aft portion of the blade. Larger discrepancy is seen in the gradients with respect to the FFD control points located along the mid chord of the section at 89% radius, as adjoint method predicts larger values. As aforementioned, this could be partly due to the truncation error in FD method. However, a satisfactory agreement is seen between the two methods.

Adjoint Flowfield

Figure 6.25 displays the contours of adjoint momentum (X-direction) at 70% blade radius of Optimized XPROP at different advance ratios, with torque coefficient Q_C as the objective function.

On observing the adjoint momentum (X-direction) flowfield, inferences similar to the XPROP's adjoint momentum flowfield for Q_C are derived. Based on the adjoint flowfield of T_C and Q_C for Optimized XPROP, it can be concluded that the change induced in momentum along the suction side's trailing edge by altering the geometry, would have a dominant effect on the propeller's performance. This holds true for all advance ratio. As the advance ratio is increased from J=0.6 to J=1.2, this region in the vicinity of boundary layer increases and extends upstream with respect to the trailing edge of the blade.

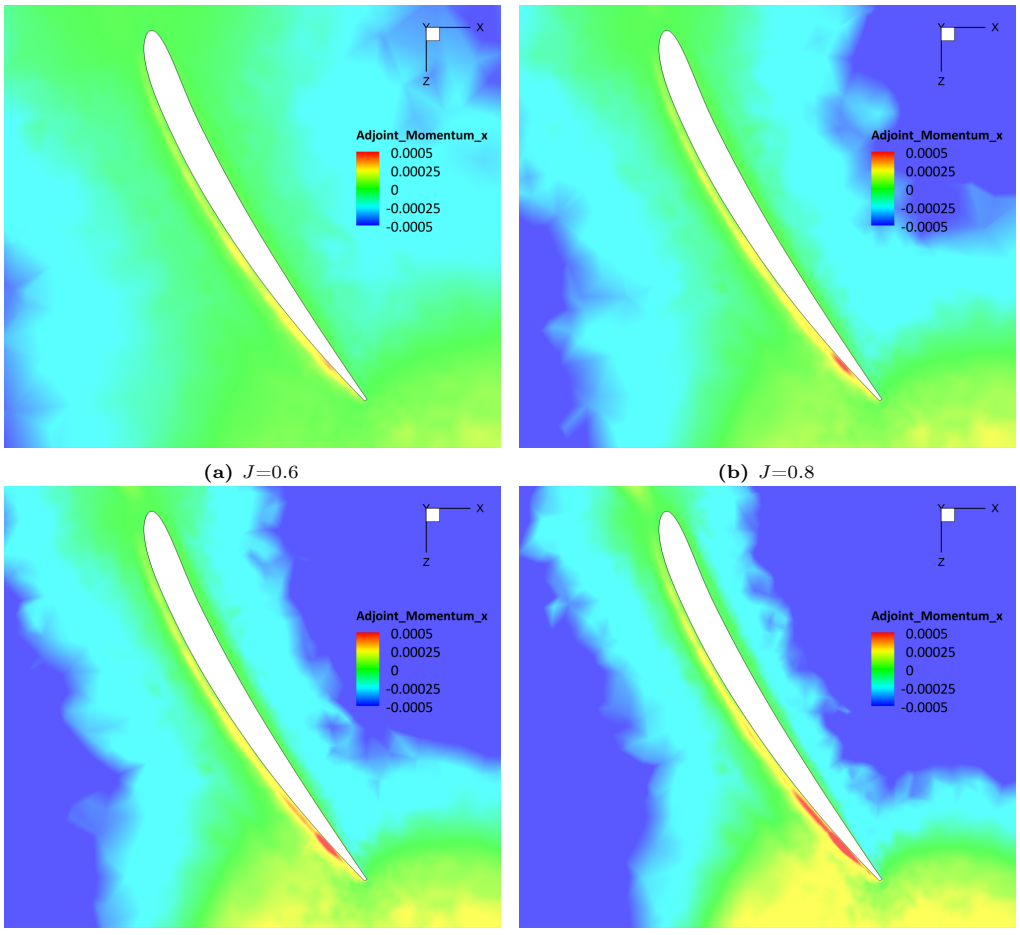

(a) J=0.6 **(b)** J=0.8

(c) J=1.0 **(d)** J=1.2

Figure 6.25: Adjoint solution for Momentum (X-direction) at 70% R_p of Optimized XPROP with torque coefficient (Q_C) as objective function at various advance ratios

6.4. Comparison of XPROP and Optimized XPROP

To analyse the effect of sweep on the adjoint gradients and sensitivities under same operating conditions, a comparative study has been performed by analysing the foregoing results of XPROP and Optimized XPROP for thrust coefficient T_C and torque coefficient Q_C.

6.4.1. Objective function: Thrust Coefficient

Surface Sensitivities

The surface sensitivity contours of XPROP and Optimized XPROP for thrust coefficient T_C at advance ratio of J=1.0 are shown in Figure 6.26. On comparing the suction side of the blade, nearly identical regions of high sensitivity are apparent along the leading edge of the blade. Although, Optimized XPROP tends to have higher concentration of high sensitivity region along the tip of the blade. This is especially visible along tip's leading edge where sweep of the blade is added. While, both the blades exhibit region of high sensitivity along the trailing edge of the blade on the pressure side. Based on the surface sensitivities, both blades have nearly similar sensitivity map at the given condition.

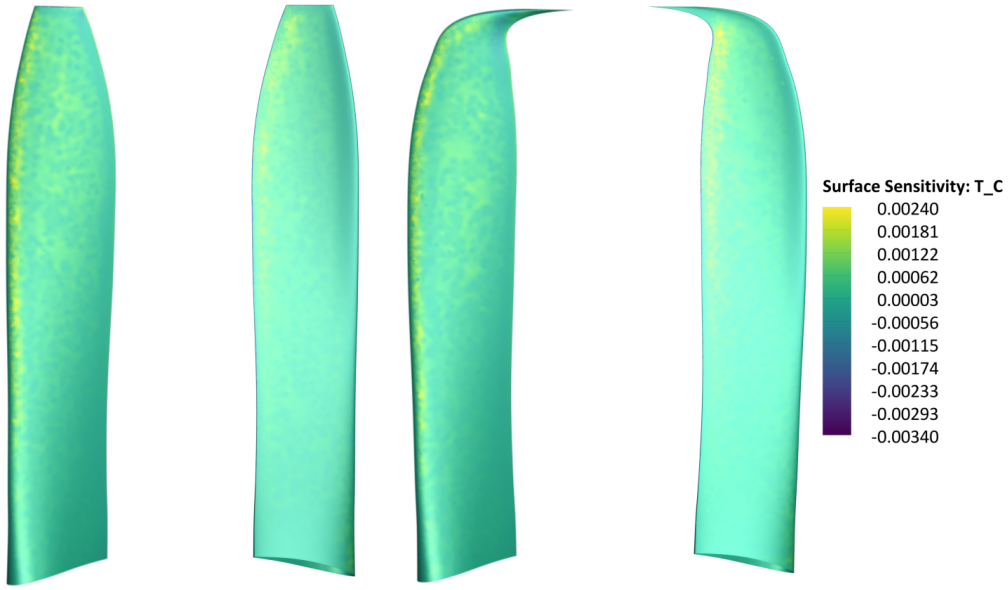

(a) XPROP **(b)** Optimized XPROP

Figure 6.26: Comparison of Surface sensitivity contours of XPROP and Optimized XPROP with Thrust (T_C) as objective function at J=1.0.

Gradients

After comparing the surface sensitivity contours of the blades, the chordwise gradients of T_C at different radial positions have been compared here. Figure 6.27 shows the chordwise gradients with respect to the FFD control points at 26%, 68%, 89%, and 101% propeller radius. It must be noted that since the orientation of the FFD boxes are defined to conform to the twist and sweep distribution of the respective blades, the displacement of a particular FFD control point would induce a change in geometry which will be different for the two blades. However, the results are presented to study how the gradients for the two blades differ especially for the region close to blade's tip.

Both the propeller blades display identical gradient behaviour for displayed radial spans except at the tip. Starting at the root, no apparent difference is seen in the gradients at 26% radius in terms of magnitude and direction. This is attributed to the fact that the blade section is the same for the two propellers at this span as well as due to the low loading in this region. At the 68% radius, it can be inferred that the difference in the gradient for the forward portion of the blade section is negligible and it is only after the design variable DV=7 that a deviation is seen where a displacement of design variable DV=9 affects the magnitude of the thrust differently for the two blades.

Optimized XPROP's gradients attained at design variables at 89% and 101% radius, show a chordwise trend different from that of XPROP's. This is the region where higher sweep (higher MCA) is introduced

in the Optimized XPROP's blade. It can be inferred that the normal displacement of the design variables located near the forward portion of the blade section would result in higher increment in thrust for Optimized XPROP in comparison to the XPROP. The increment in thrust is a result of the camber addition by normal displacement of the design variable. Whereas, same displacement of the design variables near the aft portion of the blade sections would result in higher gains in thrust for XPROP. It is interesting to notice the lower magnitude of gradients attained for the design variables located at the trailing edge for Optimized XPROP. Such variatiom in the chordwise gradients at 89% and 101% radius for the two blades can explained by the differences in the C_p curves of the two blades discussed in Section 5.2. Variation in load distribution along the chord (as a result of geometry) and local angle of attack could explain such differences in the gradients around this region.

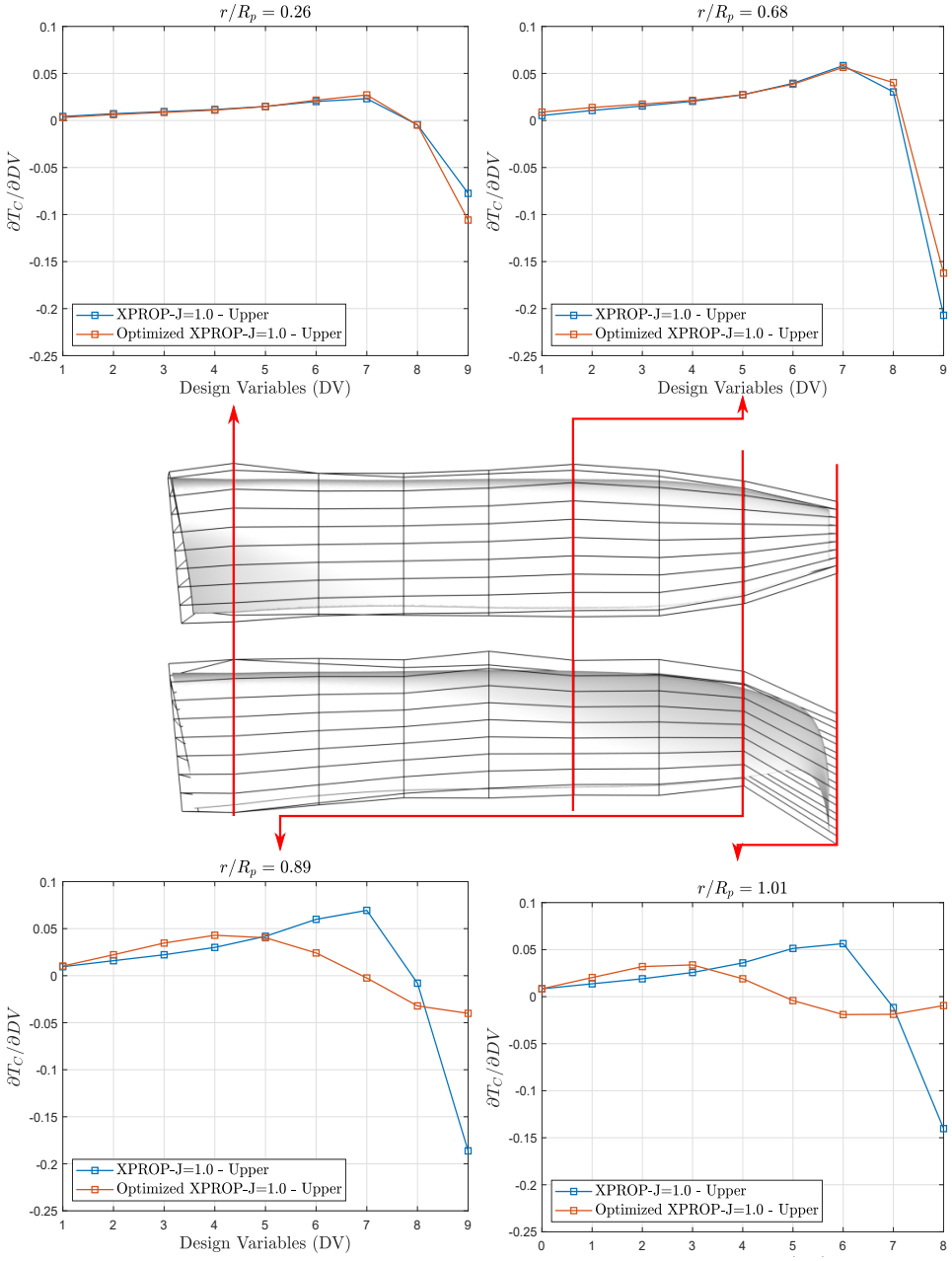

Figure 6.27: Comparison of Adjoint gradient for thrust coefficient (T_C) as objective function along the chord at different span positions of Optimized XPROP blade.

6.4.2. Objective function: Torque Coefficient

Surface Sensitivities

Figure 6.28a displays the surface sensitivity contours of XPROP and Optimized XPROP at J=1.0. On comparing the suction side of the two blades, it can be inferred that Optimized XPROP's blade has larger concentration of high sensitive region (dark blue) along the outboard of the blade as compared to XPROP. This region of high sensitivity is dominated towards the leading edge of the blade tip. Whereas, region of high sensitivity on the pressure side of the two blades are visibly same and largely spread across the outboard part of the blade. Along the trailing edge of the pressure side, a light yellow region is indicative of the region of high sensitivity too. This is apparent in the case of both the blades.

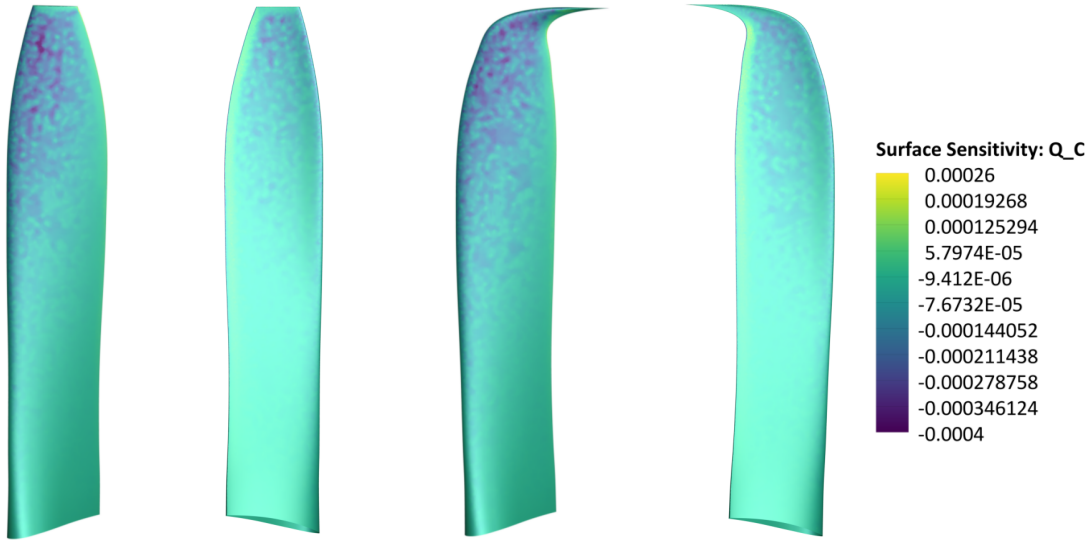

(a) XPROP **(b)** Optimized XPROP

Figure 6.28: Comparison of surface sensitivity contours of XPROP and Optimized XPROP with Torque (Q_C) as objective function at J=1.0.

Gradients

Chordwise gradients of torque coefficient Q_C of XPROP and Optimized XPROP are compared at different radial positions for J=1.0 as shown in Figure 6.29.

The trends observed here are similar to the thrust gradients observed for both the blades. This is as expected, since increment in the thrust due to additional camber by displacement of the design variable results in an increase in torque and vice versa. The addition of camber to the blade section by displacing the design variables along 26% radius have little effect on the torque for both blades. And the effect of displacing the design variable in normal direction reaps larger effect in terms of gain in torque for both the blades at 68% span as well. At these two radial positions, differences are seen for the gradients with respect to the displacement of the design variable located next to the trailing edge i.e., DV=9.

As the higher sweep is encountered at 89% and 101% radius of Optimized XPROP's blade, the trend of chordwise gradient of Q_C tends to vary as compared to XPROP. Similar to the observations made in previous subsection, normal displacement of the design variables in the forward portion of the blade section would have larger effect on torque for Optimized XPROP as a result of increased camber. Whereas, increasing the camber by displacing the design variables located in the aft of the blade section would have a larger effect on the XPROP's torque. As aforementioned, such a difference in the trend of chordwise gradients could be explained by the variation in the C_p curves for a blade section in this region.

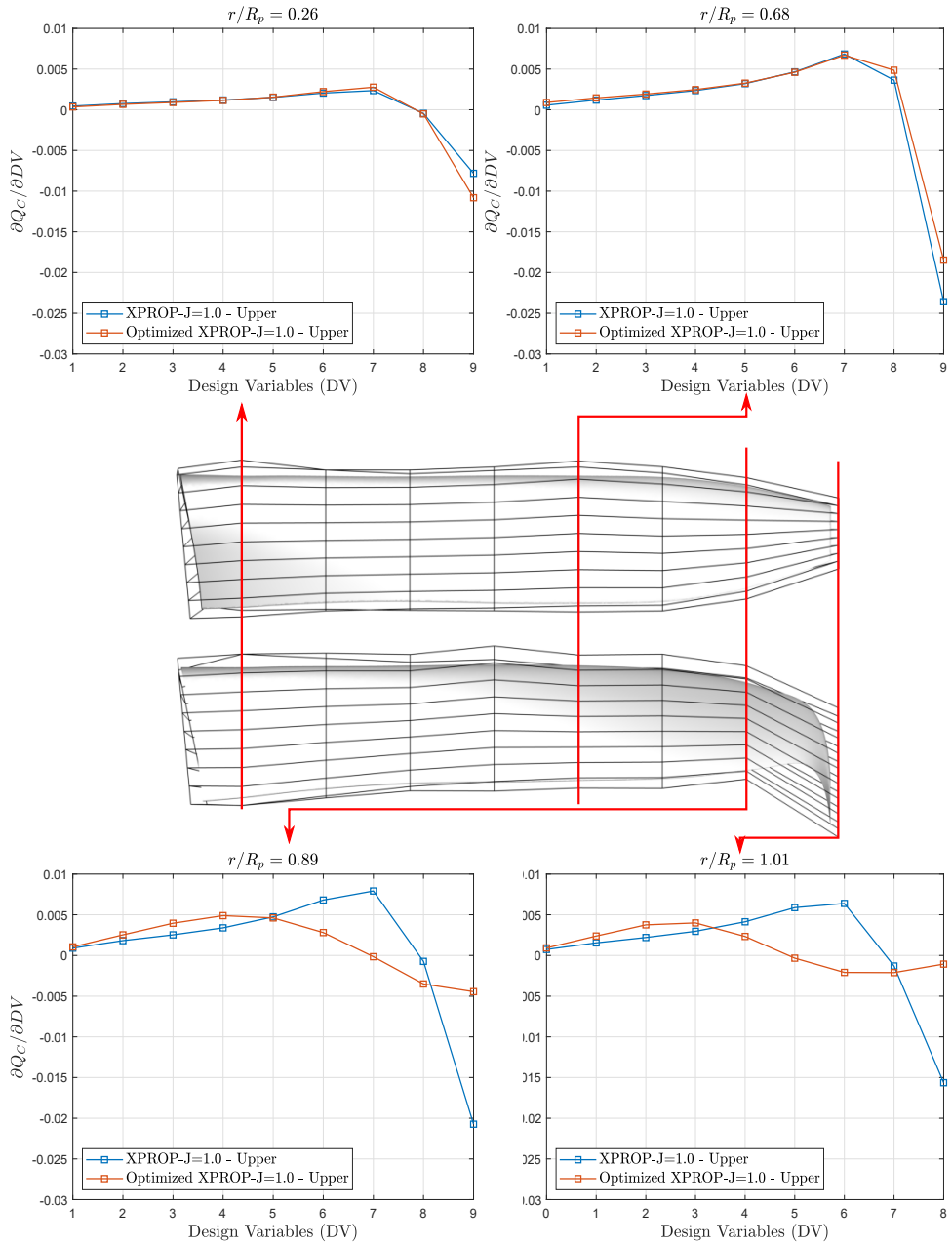

Figure 6.29: Comparison of adjoint gradient for torque coefficient (Q_C) as objective function along the chord at different span positions of Optimized XPROP blade.

6.5. Deforming the Surface using Adjoint data

Similar to the design information gained using adjoint based sensitivity analysis in the foregoing sections, designer is provided with key insights into the design of the aerodynamic body which can be used to improve the design objective function by translating this information into deformation of the body. The sensitivity maps, gradients, and adjoint flowfield of the performance parameters of both the blades have provided some interesting insights. In this section, this information is used to deform the surface of the propeller blade by displacing specific FFD control points and quantify the effect in terms of change in the performance parameters of the blade. In the case of an optimization study, this is considered first design iteration to attaining an optimal shape design.

6.5.1. Case-1-Deformation along the leading edge

As could be inferred from the surface sensitivity maps, gradients, and adjoint flowfield for the XPROP blade, displacement of the design variable normal to the surface in +Z-direction on the outboard part of the blade results in an increment in thrust coefficient T_C and torque coefficient Q_C. Using this information, the design variables of the FFD boxes located on the outboard part' leading edge of the blade are displaced to morph the blade surface as shown in Figure 6.30.

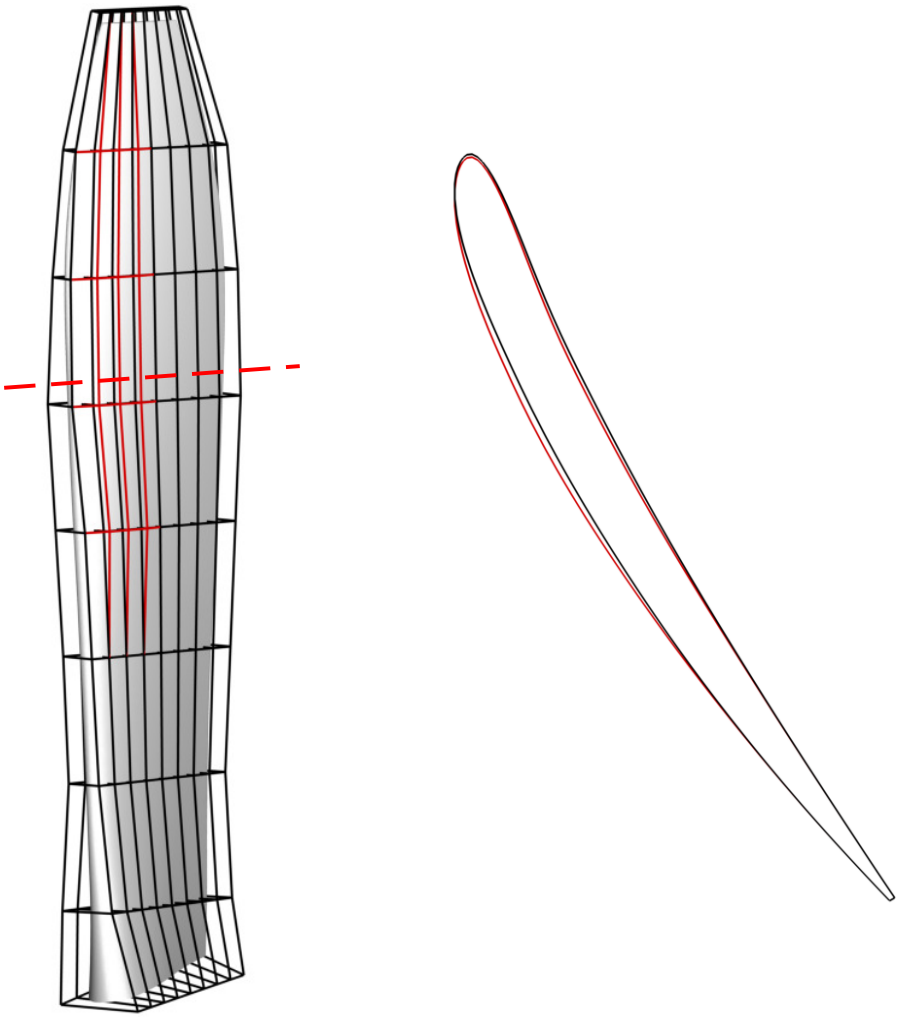

Figure 6.30: Deforming XPROP's leading edge by displacing the FFD control points and slice of the blade section at 70% radius. In the figure- Black: Baseline FFD Box and blade section; Red: Deformed FFD Box and blade section.

Table 6.2: Performance parameters of baseline XPROP and deformed XPROP for Case-1

Parameter	Baseline	Deformed
Thrust coefficient T_C	0.363	0.368
Torque coefficient Q_C	0.038	0.039

Flow over deformed blade was simulated for advance ratio J=1.0 and the resulting performance parameters are shown in Table 6.2. It can be inferred from the table that, deformed blade attains higher thrust coefficient T_C and torque coefficient Q_C as compared to the baseline blade. The deformed blade has gains an increment of 1.28% and 1.43% in the T_C and Q_C respectively. The normal displacement of the FFD control points in the +Z direction morphs the surface of the blade by adding a marginal amount of camber along 20%-50% chord wise position of the blade section. The higher camber results in increased lift at a given blade section, therefore increasing the thrust and torque of the blade. Therefore,

the results are in line with the adjoint information.

6.5.2. Case-2-Deformation along the blade's trailing edge

From the gradient information of the propeller blades, it was inferred that displacement of the control points located along the blade's trailing edge have a dominant effect on the magnitude of the performance parameter as compared to displacement of any other control points. To validate this, the design variables located along the trailing edge of the blade's outboard part are displaced in the +Z-direction. The effect of the displacement on the FFD box and the blade section at 70% radius is shown in Figure 6.31.

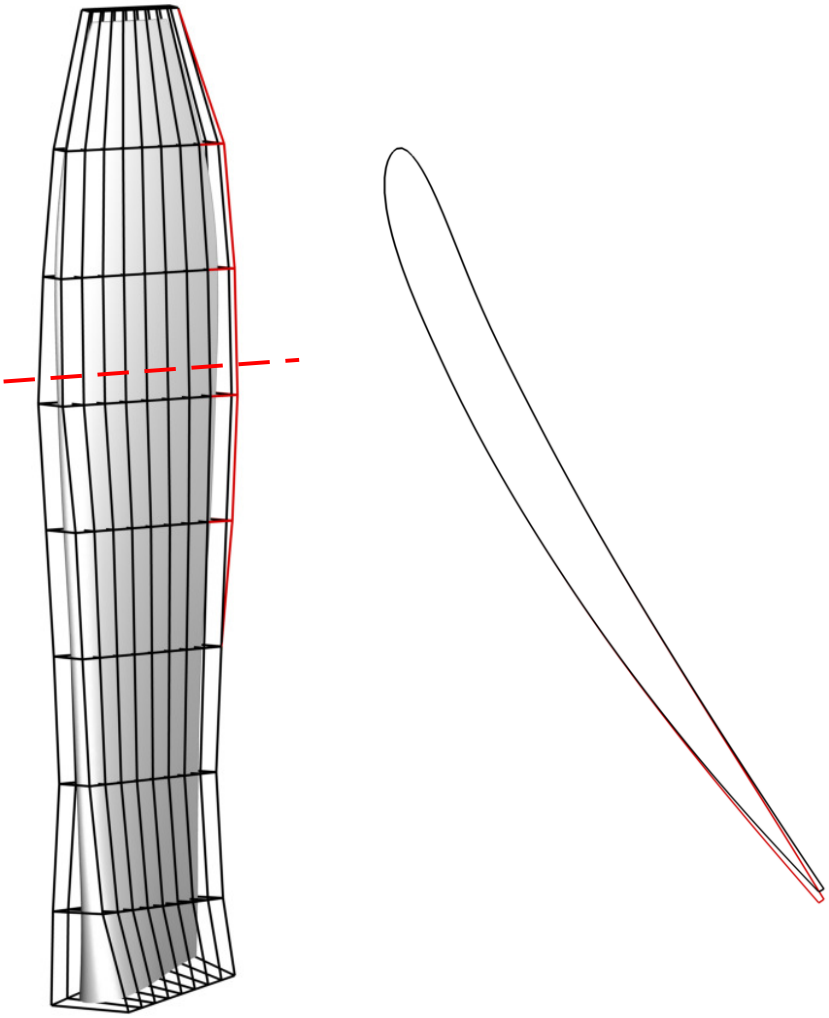

Figure 6.31: Deforming XPROP's trailing edge by displacing the FFD control points and slice of the blade section at 70% radius. In the figure- Black: Baseline FFD Box and blade section; Red: Deformed FFD Box and blade section.

Table 6.3: Performance parameters of baseline XPROP and deformed XPROP for Case-2

Parameter	Baseline	Deformed
Thrust coefficient T_C	0.363	0.329
Torque coefficient Q_C	0.038	0.034

The results of the effect of deformation along the trailing edge are shown in Table 6.3. It can be seen the deformation of the blade by displacing the FFD points along the trailing edge of the blade results in a reduction in the thrust coefficient T_C and torque coefficient Q_C as compared to the baseline blade. Decrements of 9.5% and 10.5% is attained in the T_C and Q_C respectively, on adding the camber towards the aft of the blade section. On comparing the magnitude of effect on the performance parameters of

the current case with that of the previous case of leading edge deformation, it can be confirmed that FFD control points along the trailing edge tend to have dominant effect on the performance of the blade. In other words, performance of the blade is highly sensitive to the deformation along the trailing edge. The decrease in the T_C and Q_C as a result of deformation of the blade in this case, is consistent with the gradient information as the adjoint solver predicts negative gradient on displacing the FFD control points located along the trailing edge.

6.6. Discussion on Adjoint Solver's Convergence

The key step in RANS-based design study employing an adjoint solver is accurate and efficient computation of the adjoint counterpart of RANS equations. According to Xu and Timme [58], as the stiffness and linear stability of the nonlinear flow equations is derived by the adjoint equations, it is challenging to solve the stiff adjoint equations.

Based on the observations of the convergence history of the adjoint solvers in Section 6.2 and 6.3, it was inferred that convergence of adjoint continuity equation was difficult to converge as the residuals drop by 1.5 orders of magnitude. Beyond 15000 iterations, the residuals of the adjoint continuity equation stagnate for both the propeller blades. The convergence of the residual of equations is essential for the accuracy of the solution. The stagnation of the adjoint equations after a certain number of iterations, made the author question whether the resulting gradients and sensitivities are trustworthy. Xu and Timme [58], list some known reasons that could stall the convergence of adjoint equations - simulating the complex configuration in off-design conditions, numerical stiffness due to ill-conditioned coefficient matrix, destabilisation of the solver due to large separation. Based on the comparison between the residuals of flow and adjoint solver, along with the gradient validation an engineering judgement is used to conclude that resulting adjoint results are reasonable. This judgment is also based on the results obtained with deformation studies, which were in line with the predicted adjoint gradients.

7

Conclusions and Recommendations

7.1. Conclusions

The main aim of this thesis was to implement SU2's adjoint capabilities to perform the multi-point sensitivity analysis of an isolated propeller blade's aerodynamic performance parameters with respect to the deformation to its shape design. Two blades were used to proceed with the study- XPROP and Optimized XPROP. The only difference between the two propellers was that the latter blade has an additional sweep distribution from hub to tip.

Due to the coupling between the adjoint and flow solver, the SU2's flow solver was verified and validated against the calculations from commercial CFD software ANSYS Fluent. The comparison is drawn by comparing the grid convergence, discretization error, performance parameters, and spanwise pressure distribution. The solutions with SU2 were more sensitive to the mesh refinement as compared to ANSYS Fluent's, as a higher relative difference in solution was attained for SU2. The least-squares method of GCI was implemented to determine the numerical discretization error. For the RANS-based simulation on the same computational meshes of two blades, SU2 had a higher discretization error as compared to ANSYS Fluent. In the case of XPROP's C_T behaviour, discretization error of 0.31 % and 6.85% was found with ANSYS Fluent and SU2, respectively. While, solution of XPROP's C_P with ANSYS Fluent and SU2 result in the discretization error of 0.38% and 5.58%, respectively. Similar trends are seen in the case of Optimized XPROP, as the discrteization error with ANSYS Fluent and SU2 for C_T's convergence are estimated to be 0.4% and 3.9%, respectively. For Optimized XPROP's C_P solutions on the same computational mesh result in discrteization errors of 0.42% and 11.78% with ANSYS Fluent and SU2, respectively.

Based on the comparison of the performance parameters, both solvers exhibited similar trends of curves for all advance ratios. However, offset between the curves of performance parameters with two solvers is attained. This could be attributed to the difference in the type of solvers and numerical schemes used discretization of the governing equations. However, on further inspection of the pressure distributuion curves with SU2 and ANSYS Fluent at J =1.0, discrepancies were seen at the trailing edge of all blade section, as well as the mismatch between the value of C_p at the stagnation point for outboard sections. As such discrepancies could potentially result in the values different from that of ANSYS Fluent, this observation can be potentially used to explain the offset seen in the performance curves.

Results obtained from SU2's flow solver were further used to perform a comparative study between the aerodynamic performance of the XPROP and Optimized XPROP. This was done in order to study the effect of adding a sweep to the blade on the propeller's aerodynamic performance for a range of advance ratios. Based on the study, it was found that introduction of sweep results in higher thrust and power at any given advance ratio on being compared to the baseline XPROP blade. For identical flow conditions, the sweep alters blade's thrust and torque loading. On inspecting the radial blade loading distributions, it was observed that larger deficit is attained between the power distribution of the Optimized XPROP and XPROP as compared to the differences in the thrust loading. As a result of which both the differences in the efficiencies of the two propellers exists. This trend makes Optimized XPROP operate at a higher efficiency as compared to the baseline XPROP at advance ratios J>0.9 as

the differences in thrust and torque are cancelled. The largest gain of +0.47% in aerodynamic efficiency is reaped at J=1.2 with respect to the baseline blade. Whereas, the introduction of sweep causes a decrement in the efficiency at low advance ratios, with the largest drop -0.37% taking place at J=0.6.

The adjoint solver implementation with FFD parameterization provided insights into identifying the regions of the blade that have a dominant effect on the aerodynamic performance of the propeller on geometric deformation. The discrete adjoint solver was implemented to perform a multi-point sensitivity analysis of the XPROP and Optimized XPROP blades. For baseline XPROP blade, the regions of high sensitivity on the suction side increases from hub to tip for both T_C and Q_C. The spread of this region tends to extend to a larger portion of the blade with the increasing advance ratio. Likewise, the sensitive region across the blade's leading edge on the suction side increases with advance ratio, spanning from midspan to the tip. Additionally, a region of high sensitivity was observed at blade's tip for low advance ratio (J =0.6). This sensitive region could suggest the presence of leading edge vortex, as the this region tends to reduce with increasing advance ratios. For the case of Optimized XPROP, similar observations were made for the surface sensitivity contours.

Based on the information from the thrust and torque gradients, at a given radius, the increment in the design objective increases for the normal displacement of the design variables, spanning up to 60%-70% of the section chord for XPROP. Beyond this point, the direction of gradient changes and highest gradients are attained on the deformation of the design variables close to the trailing edge. The increment in the design objective tends to vary with the advance ratios, as higher increments in the design objective are attained at the higher advance ratios. Similar trends were observed for the case of the Optimized XPROP, except in the regions close to the tip where the sweep is large. The addition of sweep at the tip has an effect on the thrust and torque gradients as the sensitivity of the gradients to advance ratio reduces. Moreover, the design variable with a dominant effect on the objective function is now located at the mid-chord region instead of the trailing edge. Therefore, the addition of sweep at the tip modifies the thrust and torque gradients.

The adjoint flowfield for both the blades with thrust and torque coefficient as the objective functions, suggested that these performance parameters are sensitive to change induced in the momentum (X-direction) in the region close to the blade section's suction side. While, inducing such a change along suction side's trailing edge would have a dominant effect on the performance parameters, at any given advance ratio. Since, changing the momentum in this region would have a same effect on the thrust and torque due to the same direction of adjoint variable, care must be taken while interpreting this information when designing an aerodynamically efficient propeller blade.

In addition to validation of the gradients with FD method, a validation study of the gradients was performed by manually displacing the design variables and deforming the blade surface. The results of the deformation study were in line with information obtained from adjoint-based sensitivity analysis. On deforming the leading edge of the propeller blade's outboard section by adding camber results in an increase in T_C and Q_C by 1.28% and 1.43%, respectively. Whereas, deforming the blade's trailing edge by displacing the design variables in the surface normal direction results in a decrement of 9.5% and 10.5% in the T_C and Q_C, respectively. Thus, indicating that reducing the camber along the trailing edge would result in an increment of T_C and Q_C. Similarly, on comparing the magnitude of difference in the performance parameters, it can be confirmed that the trailing edge of the blade along the outboard part is the most sensitive region at any given advance ratio.

To conclude, this study aimed at the multi-point sensitivity analysis of the propeller using the adjoint method provides insights into sensitivity information for designing aerodynamically efficient propeller blades as shown by the deformation studies.

7.2. Recommendations

The following recommendations for future studies are made -

- As SU2's adjoint solver tends to stagnate and was difficult to converge for both the propeller cases, using a structured mesh with periodic boundary conditions could be used to check whether the mesh of the geometry itself is the reason for stagnation of the adjoint solver.
- Implementation of CAD-based parameterization would allow to perform a sensitivity analysis of the propeller's performance with respect to the geometry parameters used to define the blade shape such as twist distribution, chord distribution etc. Such a study would provide the sensitivity

information with respect to propeller geometric parameters, wherein large number of design variables can be used.

- To analyze the acoustic performance of the two propellers, an aeroacoustic model can be coupled with the CFD method and analyze whether the swept blade has better aeroacoustic performance as a result of sweep for the operating conditions used in this study.
- As per the original research objective, employing an aeroacoustic model to perform the sensitivity analysis using adjoint eqautions to gain insights into designing efficient yet quieter propeller blades.
- An aerodynamic optimization of the propeller blades can be performed based on the gradient information obtained from this study, and placing the FFD boxes in the regions of high sensitivity.

A

Gradients for XPROP

In this appendix, the chordwise gradients of thrust coefficient T_C and torque coefficient Q_C are presented for XPROP's blade at various advance ratios. Figure A.1 shows the radial location over which the upper edges of the FFD boxes from root to tip. In this research, gradients have been computed using the FFD control points located at these radial locations indicated by design variables DV = 1 to 9. FFD control point located near the leading edge at a given radial position is designated as design variable DV=1, which counts upto 9 control points along the radial span to design variable DV=9 located near the trailing edge at a section.

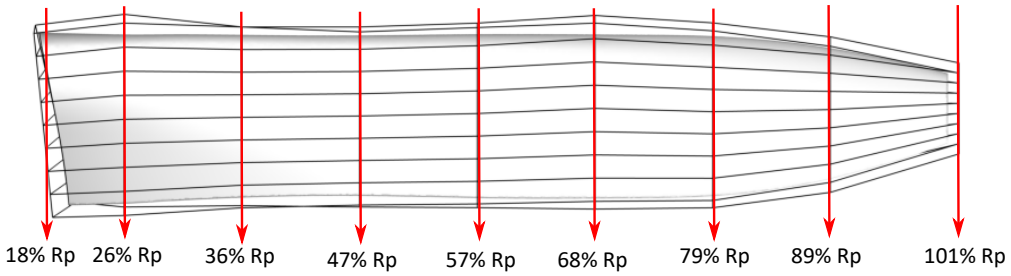

Figure A.1: Radial position of the edges of upper side FFD boxes along XPROP's blade.

Plots in Figures A.2 and A.3 represents the chordwise adjoint gradients with thrust coefficient T_C and torque coefficient Q_C as the objective function, respectively, at different radial positions of XPROP. The gradients are shown for advance ratios J=0.6, 0.8, 1.0, and 1.2.

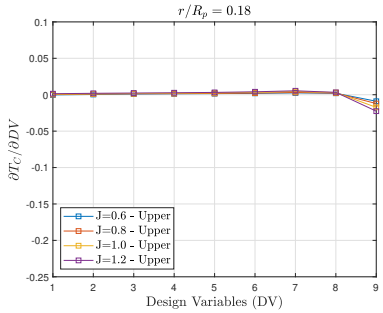

(a) $r/R_p = 18\%$

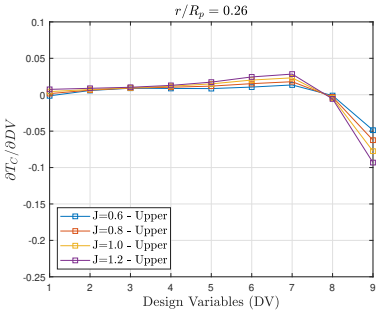

(b) $r/R_p = 26\%$

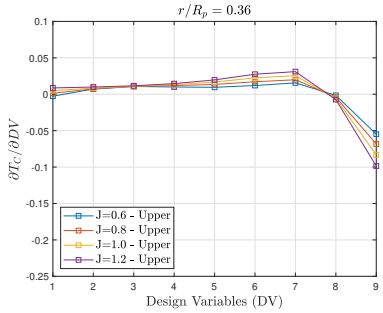

(c) $r/R_p = 36\%$

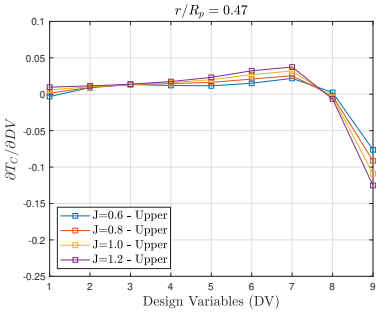

(d) $r/R_p = 47\%$

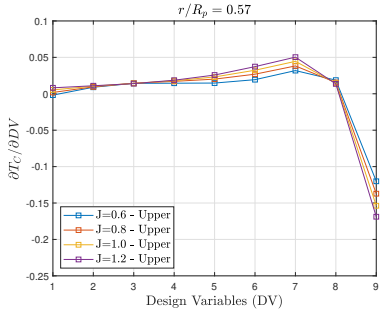

(e) $r/R_p = 57\%$

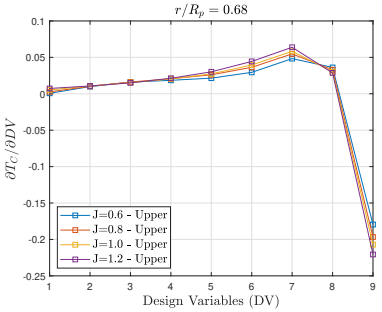

(f) $r/R_p = 68\%$

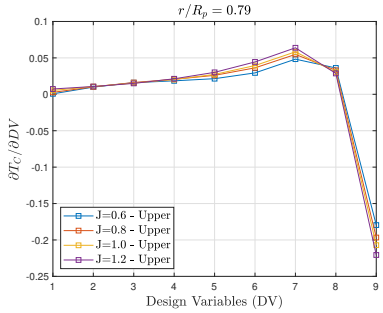

(g) $r/R_p = 79\%$

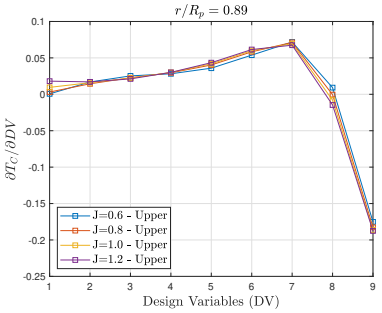

(h) $r/R_p = 89\%$

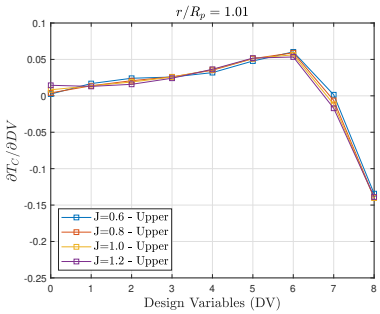

(i) $r/R_p = 101\%$

Figure A.2: Chordwise adjoint gradient with thrust coefficient (T_C) as objective function at different radial positions of XPROP's blade.

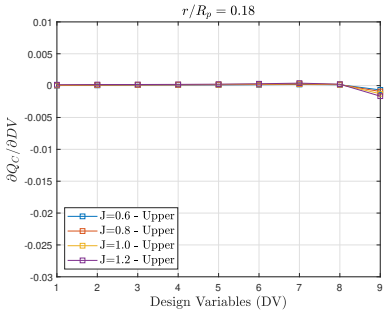

(a) $r/R_p = 18\%$

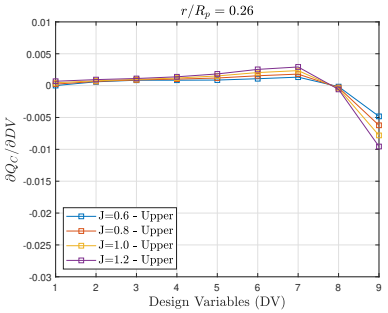

(b) $r/R_p = 26\%$

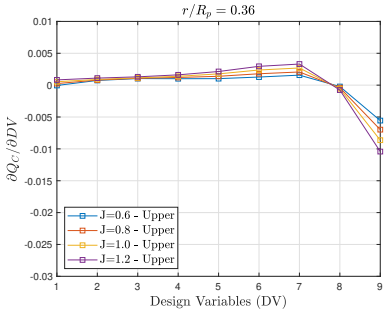

(c) $r/R_p = 36\%$

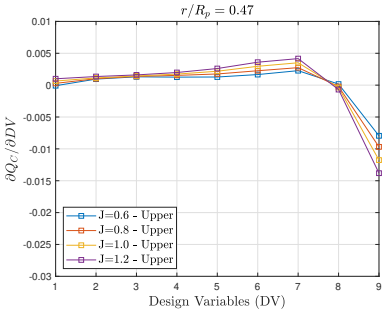

(d) $r/R_p = 47\%$

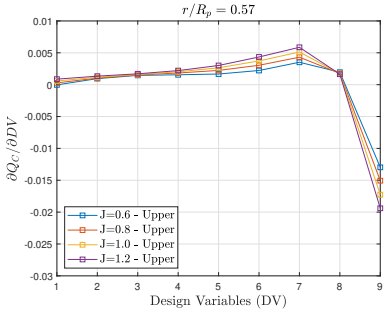

(e) $r/R_p = 57\%$

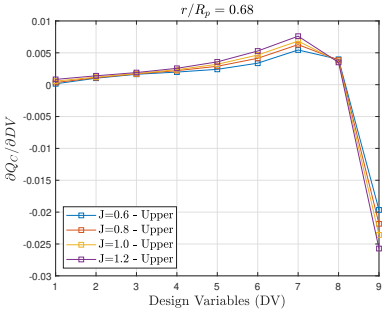

(f) $r/R_p = 68\%$

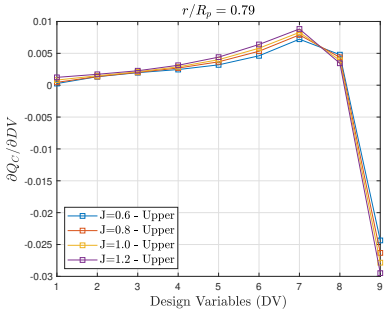

(g) $r/R_p = 79\%$

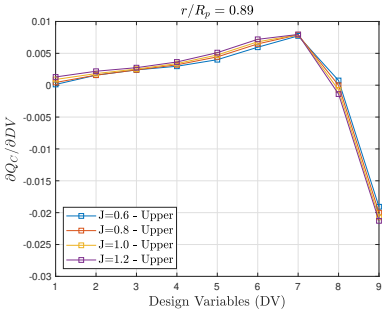

(h) $r/R_p = 89\%$

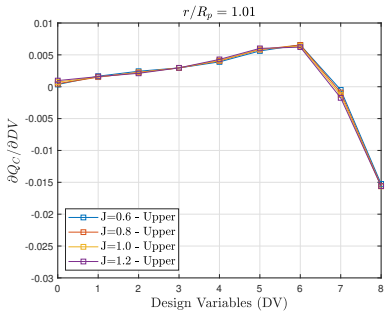

(i) $r/R_p = 101\%$

Figure A.3: Chordwise adjoint gradient with torque coefficient (Q_C) as objective function at different radial positions of XPROP's blade.

B

Gradients for Optimized XPROP

In this appendix, the chordwise gradients of thrust coefficient T_C and torque coefficient Q_C are presented for XPROP's blade at various advance ratios. Figure B.1 shows the radial location over which the upper edges of the FFD boxes from root to tip of Optimized XPROP's blade. In this research, gradients have been computed using the FFD control points located at these radial locations indicated by design variables DV = 1 to 9. FFD control point located near the leading edge at a given radial position is designated as design variable DV=1, which counts upto 9 control points along the radial span to design variable DV=9 located near the trailing edge at a section.

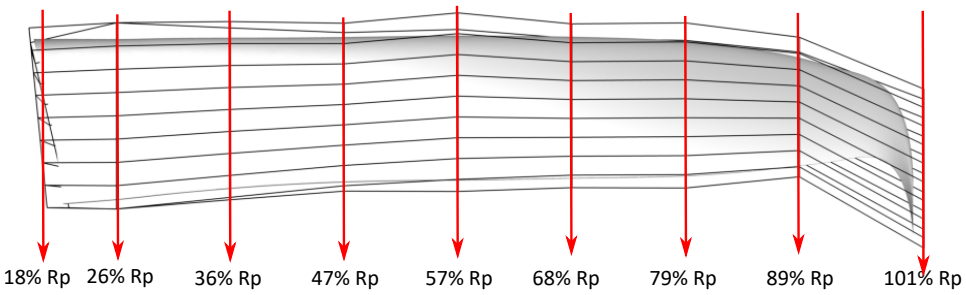

Figure B.1: Radial position of the edges of upper side FFD boxes along Optimized XPROP's blade.

Plots in Figures B.2 and B.3 represents the chordwise adjoint gradients with thrust coefficient T_C and torque coefficient Q_C as the objective function, respectively, at different radial positions of Optimized XPROP. The gradients are shown for advance ratios J=0.6, 0.8, 1.0, and 1.2.

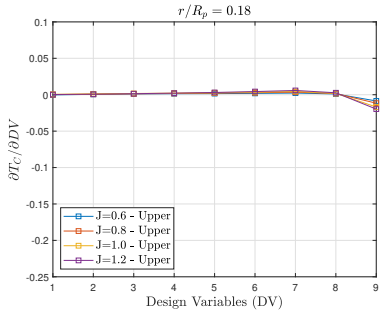

(a) $r/R_p = 18\%$

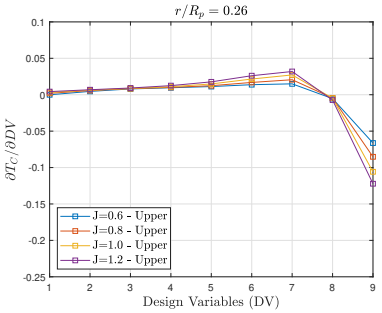

(b) $r/R_p = 26\%$

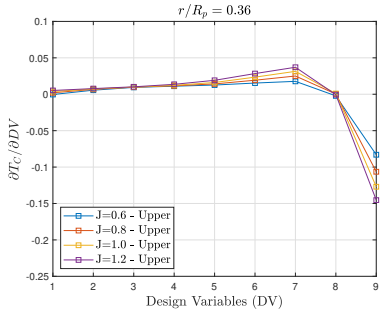

(c) $r/R_p = 36\%$

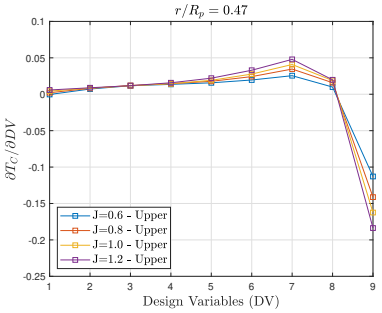

(d) $r/R_p = 47\%$

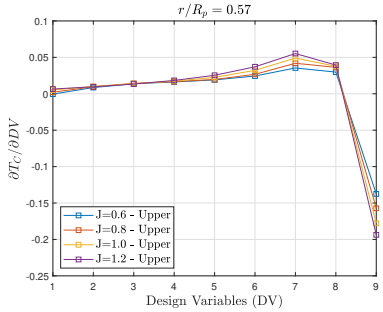

(e) $r/R_p = 57\%$

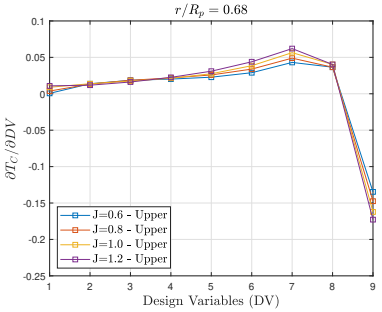

(f) $r/R_p = 68\%$

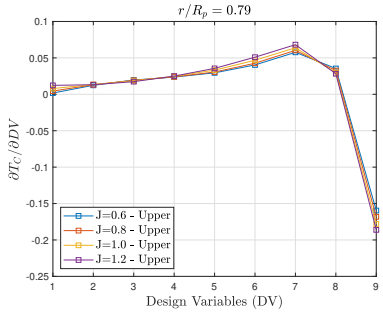

(g) $r/R_p = 79\%$

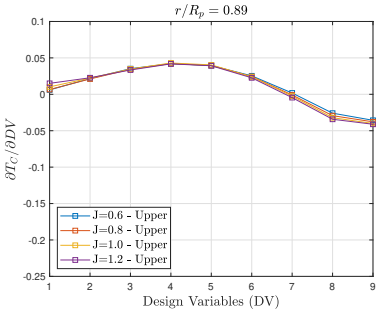

(h) $r/R_p = 89\%$

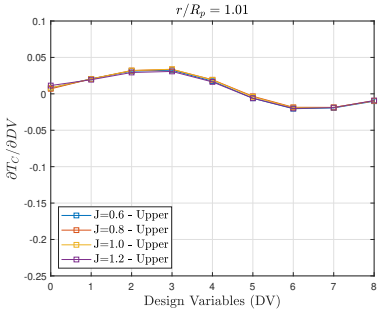

(i) $r/R_p = 101\%$

Figure B.2: Chordwise adjoint gradient with thrust coefficient (T_C) as objective function at different radial positions of Optimized XPROP's blade.

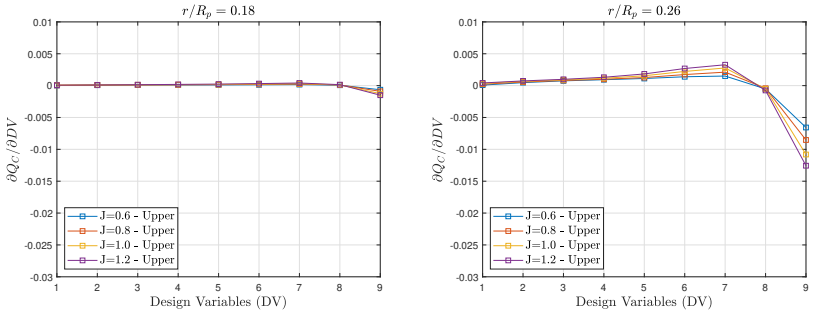

(a) $r/R_p = 18\%$

(b) $r/R_p = 26\%$

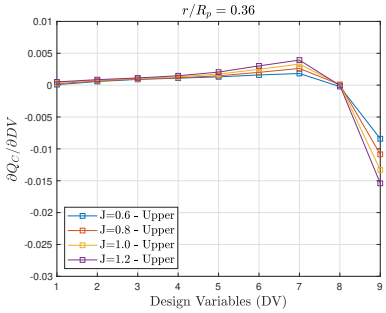

(c) $r/R_p = 36\%$

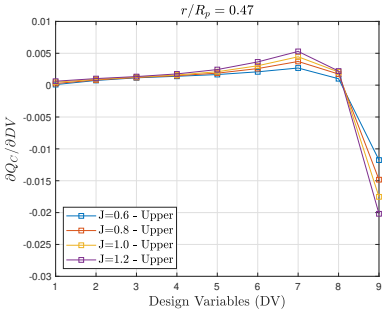

(d) $r/R_p = 47\%$

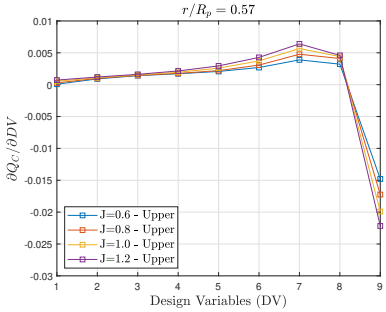

(e) $r/R_p = 57\%$

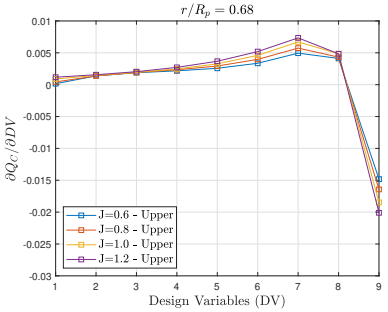

(f) $r/R_p = 68\%$

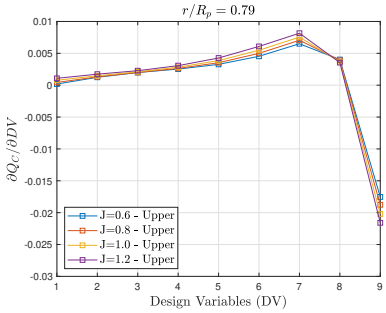

(g) $r/R_p = 79\%$

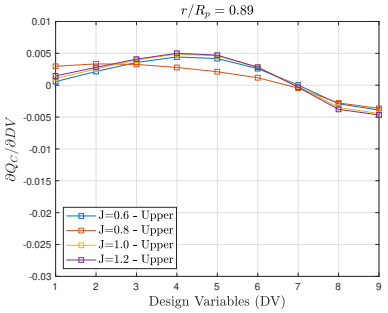

(h) $r/R_p = 89\%$

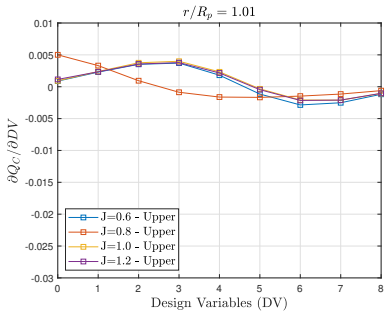

(i) $r/R_p = 101\%$

Figure B.3: Chordwise adjoint gradient with torque coefficient (Q_C) as objective function at different radial positions of Optimized XPROP's blade.

References

[1] Flightpath ACARE. "2050". *European Commission* (2011).

[2] Dheeraj Agarwal et al. "Parametric design velocity computation for CAD-based design optimization using adjoint methods". *Engineering with Computers* 34.2 (2018), pp. 225–239.

[3] Nitish Anand et al. "Assessment of FFD and CAD-based Shape Parametrization Methods for Adjoint-based Turbomachinery Shape Optimization". *Proceedings of Montreal* 7 (2018), 9th.

[4] Samuel Bernstein. *Feasibility Study Of Propeller Design For General Aviation By Numerical Optimization*. Tech. rep. SAE Technical Paper, 1976.

[5] David Biermann and Edwin P Hartman. "The Aerodynamic Characteristics of Six Full-scale Propellers Having Different Airfoil Sections" (1939).

[6] Jiri Blazek. *Computational Fluid Dynamics: Principles and Applications*. Butterworth-Heinemann, 2015.

[7] Richard Lawson Campbell. *An Approach to Constrained Aerodynamic Design with Application to Airfoils*. Vol. 3260. National Aeronautics and Space Administration, Office of Management, 1992.

[8] Jinsoo Cho and Seung-Chul Lee. "Propeller Blade Shape Optimization For Efficiency Improvement". *Computers & fluids* 27.3 (1998), pp. 407–419.

[9] Tristan Dhert, Turaj Ashuri, and Joaquim RRA Martins. "Aerodynamic Shape Optimization of Wind Turbine Blades using a Reynolds-averaged Navier–Stokes Model and an Adjoint method". *Wind Energy* 20.5 (2017), pp. 909–926.

[10] James F Dugan et al. "The NASA High-Speed Turboprop Program". *SAE Transactions* (1980), pp. 3397–3415.

[11] Luis Eça and Martin Hoekstra. "A Procedure for the Estimation of the Numerical Uncertainty of CFD Calculations Based on Grid Refinement Studies". *Journal of Computational Physics* 262 (2014), pp. 104–130.

[12] Thomas Economon, Francisco Palacios, and Juan Alonso. "Optimal shape design for open rotor blades". *30th AIAA Applied Aerodynamics Conference*. 2012, p. 3018.

[13] Thomas D Economon, Francisco Palacios, and Juan J Alonso. "A Viscous Continuous Adjoint Approach for the Design of Rotating Engineering Applications". *21st AIAA computational fluid dynamics conference*. 2013, p. 2580.

[14] Thomas D Economon et al. "SU2: An Open-Source Suite for Multiphysics Simulation and Design". *Aiaa Journal* 54.3 (2016), pp. 828–846.

[15] E Ferrer and X Munduate. "Wind Turbine Blade Tip Comparison using CFD". *Journal of Physics: Conference Series*. Vol. 75. 1. IOP Publishing. 2007, p. 012005.

[16] Joel H Ferziger, Milovan Perić, and Robert L Street. *Computational Methods for Fluid Dynamics*. Vol. 3. Springer, 2002.

[17] ANSYS Fluent. "12.0 Theory Guide". *ANSYS Inc* 5.5 (2009), p. 15.

[18] Wouter de Haan. "Impact of Blade Sweep on Aerodynamic and Aeroacoustic Performance Optimization of Isolated Propellers" (2021).

[19] Donald B Hanson. "Influence of propeller design parameters on far-field harmonic noise in forward flight". *AIAA Journal* 18.11 (1980), pp. 1313–1319.

[20] Ping He et al. "Aerothermal Optimization Of Internal Cooling Passages Using A Discrete Adjoint Method". *2018 Joint Thermophysics and Heat Transfer Conference*. 2018, p. 4080.

[21] Philip Hewitt and Simao Marques. "Aerofoil optimisation using CST parameterisation in SU2". *Royal Aeronautical Society Biennial Applied Aerodynamics Research Conference*. Vol. 2014. 2014.

[22] Raymond M Hicks and Preston A Henne. "Wing Design by Numerical Optimization". *Journal of Aircraft* 15.7 (1978), pp. 407–412.

[23] H Himmelskamp. *Profile investigations on a rotating airscrew*. Ministry of Aircraft Production, 1947.

[24] Antony Jameson. "Aerodynamic Design via Control Theory". *Journal of Scientific Computing* 3.3 (1988), pp. 233–260.

[25] Antony Jameson, Luigi Martinelli, and Niles A Pierce. "Optimum Aerodynamic Design Using the Navier–Stokes Equations". *Theoretical and computational fluid dynamics* 10.1 (1998), pp. 213–237.

[26] Antony Jameson and Kui Ou. "Optimization Methods in Computational Fluid Dynamics". *Encyclopedia of Aerospace Engineering* (2010).

[27] Gaetan KW Kenway et al. "Effective Adjoint Approaches for Computational Fluid Dynamics". *Progress in Aerospace Sciences* 110 (2019), p. 100542.

[28] KD Korkan and Gerald M Gregorek. "Propeller Aeroacoustic Methodologies". *NASA Conference Publication*. Vol. 2126. National Aeronautics and Space Administration, Scientific and Technical Information Office. 1980.

[29] Chung K Law. *Combustion Physics*. Cambridge University Press, 2010.

[30] Benoıt Marinus. "Multidisciplinary Optimization of Aircraft Propeller Blades". PhD thesis. Ecully, Ecole centrale de Lyon, 2011.

[31] Andre C Marta et al. "Interpretation Of Adjoint Solutions For Turbomachinery Flows". *AIAA journal* 51.7 (2013), pp. 1733–1744.

[32] Barnes W McCormick. *Aerodynamics, Aeronautics and Flight Mechanics*. 1995.

[33] Joel P Mendoza. "Propeller Design By Numerical Optimization" (1977).

[34] Florianr Menter. "Zonal two equation kw turbulence models for aerodynamic flows". *23rd fluid dynamics, plasmadynamics, and lasers conference*. 1993, p. 2906.

[35] Daniel C Mikkelson, Glenn A Mitchell, and Lawrence J Bober. "Summary of Recent NASA Propeller Research". *AGARD Fluid Dyn. Panel Meeting on Aerodyn. and Acoustics of Propellers*. E-2216. 1984.

[36] Eric J Nielsen and W Kyle Anderson. "Aerodynamic design optimization on unstructured meshes using the Navier-Stokes equations". *AIAA journal* 37.11 (1999), pp. 1411–1419.

[37] Antonio Pagano et al. "Tonal and Broadband Noise Calculations for Aeroacoustic Optimization of a Pusher Propeller". *Journal of Aircraft* 47.3 (2010), pp. 835–848.

[38] Francisco Palacios, Thomas D Economon, and Juan J Alonso. "Large-scale aircraft design using SU2". *53rd AIAA Aerospace Sciences Meeting*. 2015, p. 1946.

[39] Francisco Palacios et al. "Stanford University Unstructured (SU2): Analysis and Design Technology for Turbulent Flows". *52nd Aerospace Sciences Meeting*. 2014, p. 0243.

[40] Yu Peixun et al. "Aeroacoustic and Aerodynamic Optimization of Propeller Blades". *Chinese Journal of Aeronautics* (2019).

[41] Tyrone S Phillips and Christopher J Roy. "Richardson Extrapolation-based Discretization Uncertainty Estimation For Computational Fluid Dynamics". *Journal of Fluids Engineering* 136.12 (2014).

[42] Olivier Pironneau. "On Optimum Design in Fluid Mechanics". *Journal of Fluid Mechanics* 64.1 (1974), pp. 97–110.

[43] Robert J Platt Jr. "Static Tests of Four Two-blade NACA Propellers Differing in Camber and Solidity" (1948).

[44] Bill Read. *Turboprop revival?* Feb. 2019. URL: `https://www.aerosociety.com/news/turboprop-revival/`.

[45] James Reuther et al. "Aerodynamic Shape Optimization of Complex Aircraft Configurations via an Adjoint Formulation". *34th Aerospace Sciences Meeting and Exhibit*. 1996, p. 94.

[46] Ger Ruijgrok. *Elements of Airplane Performance*. VSSD, 2009.

[47] Jamshid A Samareh. "A Survey of Shape Parameterization Techniques". *NASA Conference Publication*. Citeseer. 1999, pp. 333–344.

[48] Herrmann Schlichting and Klaus Gersten. *Boundary-layer Theory*. Springer Science & Business Media, 2003.

[49] Tomas Sinnige. "Aerodynamic and Aeroacoustic Interaction Effects for Tip-Mounted Propellers: An Experimental Study". PhD thesis. Delft University of Technology, 2018.

[50] Jaroslaw Sobieszczanski-Sobieski. "The Case for Aerodynamic Sensitivity Analysis". *Sensitivity Analysis in Engineering* (1987).

[51] Philippe Spalart and Steven Allmaras. "A One-Equation Turbulence Model for Aerodynamic Flows". *30th Aerospace Sciences Meeting and Exhibit*. 1992, p. 439.

[52] Philippe R Spalart and Christopher L Rumsey. "Effective Inflow Conditions for Turbulence Models in Aerodynamic Calculations". *AIAA journal* 45.10 (2007), pp. 2544–2553.

[53] Tom CA Stokkermans et al. "Validation and Comparison of RANS Propeller Modeling Methods for Tip-Mounted Applications". *AIAA Journal* 57.2 (2019), pp. 566–580.

[54] Tom Caton Arnaud Stokkermans. "Design and Analysis of Swirl Recovery Vanes for an Isolated and a Wing Mounted Tractor Propeller" (2015).

[55] Michiel Hannes Straathof. "Shape Parameterization in Aircraft Design: A Novel Method, based on B-Splines". PhD dissertation. TU Delft, 2012.

[56] James Courtland Townsend et al. *Integration of a CAD System into an MDO Framework*. Citeseer, 1998.

[57] L.L.M. Veldhuis. "Propeller wing aerodynamic interference". PhD thesis. Delft University of Technology, 2005.

[58] Shenren Xu and Sebastian Timme. "Robust and Efficient Adjoint Solver for Complex Flow Conditions". *Computers & Fluids* 148 (2017), pp. 26–38.

[59] Xue-ke Zheng et al. "The Efficiency Analysis Of High-altitude Propeller Based On Vortex Lattice Lifting Line Theory". *The Aeronautical Journal* 121.1236 (2017), pp. 141–162.

[60] GJD Zondervan. "A Review Of Propeller Modelling Techniques Based On Euler Methods". *Series 01: Aerodynamics 05* (1998).